



MINISTÉRIO DA CIÊNCIA, TECNOLOGIA, INOVAÇÕES E COMUNICAÇÕES
INSTITUTO NACIONAL DE PESQUISAS ESPACIAIS

sid.inpe.br/mtc-m21b/2017/05.05.02.33-TDI

3D MODEL MAGNETO-ACOUSTIC WAVES IN CORONAL LOOPS OBSERVED DURING TRANSIENT EVENTS

Sandra Milena Conde Cuellar

Doctorate Thesis of the Graduate
Course in Astrophysics, guided
by Dr. Joaquim Eduardo Rezende
Costa, approved in May 25, 2017.

URL of the original document:

<<http://urlib.net/8JMKD3MGP3W34P/3NR6PP2>>

INPE
São José dos Campos
2017

PUBLISHED BY:

Instituto Nacional de Pesquisas Espaciais - INPE

Gabinete do Diretor (GB)

Serviço de Informação e Documentação (SID)

Caixa Postal 515 - CEP 12.245-970

São José dos Campos - SP - Brasil

Tel.:(012) 3208-6923/6921

E-mail: pubtc@inpe.br

**COMMISSION OF BOARD OF PUBLISHING AND PRESERVATION
OF INPE INTELLECTUAL PRODUCTION (DE/DIR-544):**

Chairperson:

Maria do Carmo de Andrade Nono - Conselho de Pós-Graduação (CPG)

Members:

Dr. Plínio Carlos Alvalá - Centro de Ciência do Sistema Terrestre (CST)

Dr. André de Castro Milone - Coordenação de Ciências Espaciais e Atmosféricas (CEA)

Dra. Carina de Barros Melo - Coordenação de Laboratórios Associados (CTE)

Dr. Evandro Marconi Rocco - Coordenação de Engenharia e Tecnologia Espacial (ETE)

Dr. Hermann Johann Heinrich Kux - Coordenação de Observação da Terra (OBT)

Dr. Marley Cavalcante de Lima Moscati - Centro de Previsão de Tempo e Estudos Climáticos (CPT)

Silvia Castro Marcelino - Serviço de Informação e Documentação (SID) **DIGITAL LIBRARY:**

Dr. Gerald Jean Francis Banon

Clayton Martins Pereira - Serviço de Informação e Documentação (SID)

DOCUMENT REVIEW:

Simone Angélica Del Ducca Barbedo - Serviço de Informação e Documentação (SID)

Yolanda Ribeiro da Silva Souza - Serviço de Informação e Documentação (SID)

ELECTRONIC EDITING:

Marcelo de Castro Pazos - Serviço de Informação e Documentação (SID)

André Luis Dias Fernandes - Serviço de Informação e Documentação (SID)



MINISTÉRIO DA CIÊNCIA, TECNOLOGIA, INOVAÇÕES E COMUNICAÇÕES
INSTITUTO NACIONAL DE PESQUISAS ESPACIAIS

sid.inpe.br/mtc-m21b/2017/05.05.02.33-TDI

3D MODEL MAGNETO-ACOUSTIC WAVES IN CORONAL LOOPS OBSERVED DURING TRANSIENT EVENTS

Sandra Milena Conde Cuellar

Doctorate Thesis of the Graduate
Course in Astrophysics, guided
by Dr. Joaquim Eduardo Rezende
Costa, approved in May 25, 2017.

URL of the original document:

<http://urlib.net/8JMKD3MGP3W34P/3NR6PP2>

INPE
São José dos Campos
2017

Cataloging in Publication Data

Conde Cuellar, Sandra Milena.

C751t 3D model magneto-acoustic waves in coronal loops observed during transient events / Sandra Milena Conde Cuellar. – São José dos Campos : INPE, 2017.

xxiv + 125 p. ; (sid.inpe.br/mtc-m21b/2017/05.05.02.33-TDI)

Thesis (Doctorate in Astrophysics) – Instituto Nacional de Pesquisas Espaciais, São José dos Campos, 2017.

Guiding : Dr. Joaquim Eduardo Rezende Costa.

1. Flares. 2. Waves. 3. Magnetohydrodynamic. 4. Relation to magnetic field. 5. Structures. I.Title.

CDU 520.62:537.84



Esta obra foi licenciada sob uma Licença [Creative Commons Atribuição-NãoComercial 3.0 Não Adaptada](https://creativecommons.org/licenses/by-nc/3.0/).

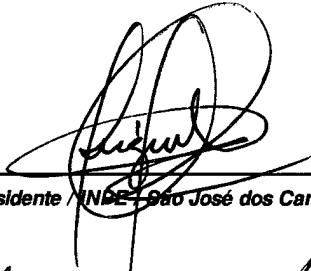
This work is licensed under a [Creative Commons Attribution-NonCommercial 3.0 Unported License](https://creativecommons.org/licenses/by-nc/3.0/).

Aluno (a): **Sandra Milena Conde Cuellar**

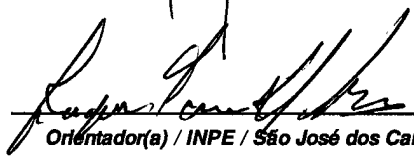
Título: "3D MODEL MAGNETO-ACOUSTIC WAVES IN CORONAL LOOPS OBSERVED DURING TRANSIENT EVENTS"

Aprovado (a) pela Banca Examinadora em cumprimento ao requisito exigido para obtenção do Título de **Doutor(a)** em **Astrofísica**

Dr. César Augusto Costa


Presidente / INPE / São José dos Campos - SP

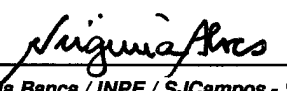
Dr. Joaquim Eduardo Rezende Costa


Orientador(a) / INPE / São José dos Campos - SP

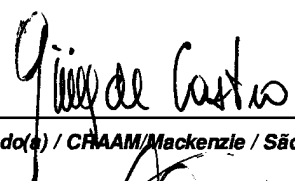
Dr. Luis Eduardo Antunes Vieira


Membro da Banca / INPE / São José dos Campos - SP

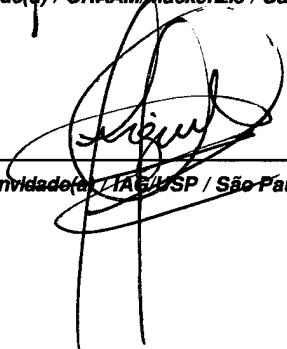
Dra. Maria Virginia Alves


Membro da Banca / INPE / SJCampos - SP

Dr. Carlos Guillermo Giménez de Castro


Convidado(a) / CRAAM/Mackenzie / São Paulo - SP

Dra. Vera Jatenco Silva Pereira


Convidado(a) / IAE/USP / São Paulo - SP

Este trabalho foi aprovado por:

maioria simples

unanimidade

São José dos Campos, 25 de maio de 2017

To my family with love

ACKNOWLEDGEMENTS

I would like to express my sincere gratitude to one and all, who directly or indirectly, have made possible the realization of this work.

Firstly, I would like to thank my advisor Dr Joaquim Eduardo Rezende Costa for the continuous support of my Ph. D study and related research, for his patience and guidance. I am very grateful with him because the door of his office was always open to discuss topics related with my research or thesis writing. He allowed me to develop this work respecting my ideas and independence, but steered me in the right direction whenever he thought I needed it.

Besides my advisor, I am thankful to my husband, Dr Carlos Eduardo Cedeño Montaña, for encourage me to perform this long task and help me in all its steps, for his fruitful and stimulating discussions, which help me to see my research from different view points.

I am grateful to Dr Miguel Ibañez for the initial discussion to beginning this research, to Dr José Carlos Neves de Araújo for his helpful and friendly hand in the difficult situations during the course of this Ph.D and my family for supporting me spiritually throughout all these years.

I want to thanks to Astrophysical Division (DAS) for providing me with all the necessary facilities to develop my research. To *Programa de Apoio à Pós-Graduação* (PROAP) for the financial support to attend the different schools and to receive the necessary training to perform this work.

I would like to thank the financial support of the Coordination for the Improvement of Higher Education Personnel (CAPES).

I would like to thank to Solar Dynamics Observatory (SDO) and a mission for the NASA's Living With a Star (LWS) program for available data using in this research. Finally, I would like to thanks to Dr Christopher Torrence and Dr Gilbert P. Compo for the wavelet software, which is available at <http://paos.colorado.edu/research/wavelets/>. Also, I thank to Dr Marcus Aschwanden and his team for the automated detection of temperatures routines available at <http://www.lmsal.com/~aschwand/software>.

ABSTRACT

We present a three-dimensional analysis of magneto-acoustic waves, along the seven coronal loops, observed on the active region NOAA 11272 during the class B and C flares. We found 19-, 9-, 5-, 2-, 1-, and 0.6-minute waves using the pixelised wavelet filtering method over images obtained from the *Atmospheric Imaging Assembly* instrument. We modelled the velocity of these waves along the extrapolated magnetic field lines that reproduce the observed loops in extreme ultraviolet. The extrapolation was made over magnetograms, got from the *Helioseismic and Magnetic Imager* instrument, using the linear force-free approximation. From our model, we found temperatures $10^3 \lesssim T \lesssim 1.8 \times 10^7$ K and densities $10^7 \lesssim n \lesssim 10^{17}$ cm⁻³, covering from photosphere to corona, as expected in the solar atmosphere. Hence, we obtained acoustic $c_s \approx 10^2$ km s⁻¹ and Alfvénic $v_A \approx 10^4$ km s⁻¹ velocities values which are in agreement with the literature. In addition, the brightness asymmetry observed along the coronal loops is explained by the magnetic field and Alfvén velocity distributions along the extrapolated field lines. We found fast magneto-acoustic waves at the beginning of B3.8 and C1.9 flares and slow modes along the loops during all flares. Our 3D model represents an unprecedented method to study waves in coronal loops. All results are coherent with expected values in the solar atmosphere conditions.

Keywords: Flares, Waves. Corona, Structures. Flares, Relation to Magnetic Field. Waves, Magnetohydrodynamic. Waves, Alfvén.

MODELO TRIDIMENSIONAL DE ONDAS MAGNETOACÚSTICAS EM *LOOPS* CORONAIS OBSERVADOS DURANTE EVENTOS TRANSIENTES

RESUMO

Apresentamos uma análise tridimensional de ondas magnetoacústicas ao longo de sete *loops* coronais, observados na região ativa NOAA 11272 durante os flares de classe B e C. Encontramos ondas de 19, 9, 5, 2, 1 e 0.6 minutos usando o método *Pixelised Wavelet Filtering* sobre imagens obtidas com o instrumento *Atmospheric Imaging Assembly*. Modelamos as velocidades dessas ondas ao longo das linhas de campo magnético extrapoladas que reproduzem os *loops* observados em ultravioleta extremo. A extrapolação foi feita sobre os magnetogramas obtidos com o instrumento *Helioseismic and Magnetic Imager*, usando a aproximação *Linear Force-Free*. A partir do nosso modelo, encontramos temperaturas de $10^3 \lesssim T \lesssim 1.8 \times 10^7$ K e densidades de $10^7 \lesssim n \lesssim 10^{17}$ cm⁻³, cobrindo desde a fotosfera até a coroa, como esperado na atmosfera solar. Desta forma, obtivemos valores para as velocidades acústica e Alfvénica de $c_s \approx 10^2$ km s⁻¹ e $v_A \approx 10^4$ km s⁻¹ respectivamente, as quais estão acorde com a literatura. Adicionalmente, a assimetria no brilho observada ao longo dos *loops* coronais é explicada pelas distribuições do campo magnético e da velocidade Alfvén ao longo das linhas extrapoladas. Nós encontramos ondas magnetoacústicas rápidas no início dos flares B3.8 e C1.9 e modos lentos ao longo dos *loops* durante todos os flares. O nosso modelo representa um método inédito para estudar ondas em *loops* coronais. Todos os resultados são coerentes com os valores esperados nas condições da atmosfera solar.

Keywords: Flares, Ondas. Corona, Estruturas. Flares, Relação com o Campo Magnético. Ondas, Magnetohidrodinâmicas. Ondas, Alfvén.

LIST OF FIGURES

	<u>Page</u>
2.1 Doppler shift in the Fe XIX line observed with SOHO/SUMER on 9 March 2001.	4
2.2 Radiative loss functions for chromospheric and coronal plasma.	12
2.3 Model for the solar corona based on energy balance.	13
2.4 QPP Spectra of X1.6 class flare	15
3.1 Design of Solar Dynamics Observatory.	17
3.2 Sun's image in the band passes of AIA.	18
3.3 Temperature response functions for six EUV channels.	20
3.4 LOS magnetogram and EUV image of NOAA 11272.	21
3.5 Tracking of NOAA 11272 observed by AIA in 1700 Å.	23
4.1 Morlet mother function.	27
4.2 Paul mother function.	27
4.3 Derivative of Gaussian (DOG) mother function.	28
4.4 Synthetic data cube	30
4.5 Test signal and Variance map	30
4.6 Temporal signal and wavelet spectra for synthetic data cube.	31
4.7 Global Synthetic Integrated Wavelet Power Spectrum	32
4.8 Temporal signal filtered.	33
4.9 Dynamical Maps.	34
5.1 Plasma β parameter in the solar atmosphere.	37
5.2 Twist for force-free magnetic field	39
5.3 Extrapolation of magnetic field in the solar limb	41
5.4 Loops reproduced using SDO and STEREO images	43
6.1 Active Region NOAA 11272 seen in nine SDO/AIA wavelengths	45
6.2 Time profile of signal for NOAAs 11271 and 11272 in 131 Å.	46
6.3 Time profile of intensity for NOAA 11272.	47
6.4 Loops perturbed during the period of flares occurred in NOAA 11272.	48
6.5 Variance map for loops perturbed during the flares occurred in NOAA 11272	49
6.6 Wavelet spectra over temporal signal of 1700 Å	50
6.7 Global spatially integrated wavelet power spectrum for 1600 Å.	51
6.8 narrowband map for 1600 Å	52
6.9 Amplitude narrowband maps for waves of 19 minutes along the loop A	53

6.10	Amplitude narrowband maps for waves of 19 minutes in loops B and C .	54
6.11	Amplitude and phase narrowband maps for waves of 19 minutes.	55
6.12	Amplitude narrowband map for waves of 19 minutes in loops D and G . .	56
6.13	Amplitude narrowband maps for waves of 19 minutes in loops E and F . .	57
6.14	Amplitude and phase narrowband maps for waves of 19 minutes from the loops D to G	58
6.15	Amplitude narrowband maps for waves of 9 minutes in loop A and foot- point of loop C	59
6.16	Amplitude narrowband maps for waves of 9 minutes in loops B and C . .	60
6.17	Amplitude and phase maps for waves of 9 minutes in loops A , B , and C .	61
6.18	Amplitude narrowband maps for waves of 9 minutes in loop D	62
6.19	Amplitude narrowband maps for waves of 9 minutes in loops E and F . .	63
6.20	Amplitude and phase for waves of 9 minutes in loops D , E , and F	64
6.21	Amplitude narrowband maps for waves of 9 minutes in loop G	65
6.22	Amplitude and phase narrowband maps for waves of 9 minutes in loop G .	65
6.23	Amplitude narrowband maps for waves of 5 minutes in loop A and foot- point 1 of loop C	66
6.24	Amplitude and phase for waves of 5 minutes in loops A and C	67
6.25	Amplitude narrowband maps for waves of 5 minutes in loops B and C . .	68
6.26	Amplitude narrowband maps for 5-minutes waves in footpoint 1 of loop C	69
6.27	Amplitude and phase for 5-minutes waves in loop B and footpoint 1 of C .	70
6.28	Amplitude narrowband maps for waves of 5 minutes in loop D	71
6.29	Amplitude narrowband maps for waves of 5 minutes in loop G	71
6.30	Amplitude and phase for waves of 5 minutes in loops D and G	72
6.31	Amplitude of 2-min travelling waves in loops A and B	73
6.32	Amplitude and phase maps for waves of 2 minutes in loops A and B . . .	74
6.33	Amplitude narrowband maps for waves of 2 minutes in loops A and C . .	75
6.34	Amplitude and phase maps for waves of 2 minutes in loops A to C	76
6.35	Amplitude narrowband maps for travelling waves of 1 minute in the footpoints of the loops A and C	77
6.36	Amplitude and phase maps for waves of 1 minute between the loops A to C footpoints.	77
6.37	Amplitude narrowband maps for waves of 36 seconds in the footpoint of loops A and C	78
6.38	Amplitude and phase narrowband maps for travelling waves of 36 seconds in the footpoints of loops A and C	79
6.39	Best fitted decaying curve	81
6.40	Magnetic field lines plotted over AIA images.	82

6.41	Image of loop A obtained by SDO/AIA in nine wavelengths.	83
6.42	Magnetic field lines for $\alpha_A=-1.5\times 10^{-2}$ Mm $^{-1}$ over images of SDO/AIA. .	84
6.43	Magnetic field lines for $\alpha_A=-1.5\times 10^{-2}$ Mm $^{-1}$ over an image of SDO/HMI.	85
6.44	Image of loop B obtained by SDO/AIA in nine wavelengths.	86
6.45	Magnetic field lines for $\alpha_B=-6.8\times 10^{-3}$ Mm $^{-1}$ over images of SDO/AIA. .	87
6.46	Magnetic field lines for $\alpha_B=-6.8\times 10^{-3}$ Mm $^{-1}$ over an image of SDO/HMI.	88
6.47	Image of loop C obtained by SDO/AIA in nine wavelengths.	89
6.48	Magnetic field lines for $\alpha_C=1.1\times 10^{-2}$ Mm $^{-1}$ over images of SDO/AIA. .	90
6.49	Magnetic field lines for $\alpha_C=1.1\times 10^{-2}$ Mm $^{-1}$ over an image of SDO/HMI.	91
6.50	Image of loop D obtained by SDO/AIA in nine wavelengths.	92
6.51	Magnetic field lines for $\alpha_{D_1}=1.5\times 10^{-2}$ Mm $^{-1}$ and $\alpha_{D_2}=2.2\times 10^{-2}$ Mm $^{-1}$ over images of SDO/AIA.	93
6.52	Magnetic field lines for $\alpha_{D_1}=1.5\times 10^{-2}$ Mm $^{-1}$ and $\alpha_{D_2}=2.2\times 10^{-2}$ Mm $^{-1}$ over an image of SDO/HMI.	94
6.53	Image of loops E and F obtained by SDO/AIA in nine wavelengths.	95
6.54	Magnetic field lines for $\alpha_E=1.3\times 10^{-2}$ Mm $^{-1}$ and $\alpha_F=2.2\times 10^{-2}$ Mm $^{-1}$ over images of SDO/AIA.	96
6.55	Magnetic field lines for $\alpha_E=1.3\times 10^{-2}$ Mm $^{-1}$ and $\alpha_F=2.2\times 10^{-2}$ Mm $^{-1}$ over an image of SDO/HMI.	97
6.56	Image of loop G obtained by SDO/AIA in nine wavelengths.	98
6.57	Magnetic field lines for $\alpha_G=-2.2\times 10^{-2}$ Mm $^{-1}$ over images of SDO/AIA. .	99
6.58	Magnetic field lines for $\alpha_G=-2.2\times 10^{-2}$ Mm $^{-1}$ over an image of SDO/HMI.	100
6.59	Logarithm of the number density along the loops A–C	101
6.60	Temperature distribution along the loops D–G	102
6.61	Sound velocity c_s along the loops A–C	103
6.62	Sound velocity c_s along the loops D–G	103
6.63	Alfvén velocity v_a along the loops A–C	104
6.64	Alfvén velocity v_a along the loops D–G	105

LIST OF TABLES

	<u>Page</u>
3.1 Distribution of wavelengths, lines, regions, and temperatures observed by AIA.	19
3.2 Information about AIA data adquisition at websites.	22
5.1 Sound velocities expected for SDO/AIA EUV lines, according to O’Dwyer et al. (2010) model.	44
6.1 Flares occurred in NOAA 11272 on 17 August 2011.	46
6.2 Description of perturbed loops during the period of flares.	48
6.3 Fitting parameters for waves found in NOAA 11272.	80
6.4 Lenght L (Mm), height h (km) and magnetic field B (G) of extrapolated field lines.	100
6.5 Phase velocity v_{ph} for 0.6-, 1- and 2-minute waves.	105
6.6 Phase velocity v_{ph} for 5-, 9- and 19-minute waves.	106

LIST OF ABBREVIATIONS

AIA	– Atmospheric Imaging Assembly
CCD	– Charge Coupled Device
CDS	– Coronal Diagnostic Spectrometer
COI	– Cone Of Influence
DOG	– Derivative Of Gaussian
EIT	– Extreme ultraviolet Imaging Telescope
EUV	– Extreme Ultraviolet
EVE	– Extreme ultraviolet Variability Experiment
FITS	– Flexible Image Transport System
FOV	– Field Of View
GBM	– Gamma-ray Burst Monitor
GOES	– Geostationary Operational Environmental Satellite
GSIWPS	– Global Spatially Integrated Wavelet Power Spectrum
GWS	– Global Wavelet Spectrum
HMI	– Helioseismic and Magnetic Imager
HXR	– Hard X-Ray
IDL	– Interactive Data Language
IRIS	– Interface Region Imaging Spectrograph
JSOC–SDP	– Joint SDO Operations Center–Science-Data Processing
LFFF	– Linear Force-Free Field
LMSAL	– Lockheed Martin Solar and Astrophysics Laboratory
LOS	– Line Of Sight
LWS	– Living With a Star
MHD	– Magnetohydrodynamics
NASA	– National Aeronautics and Space Administration
NIS	– Normal Incidence Spectrometer
NLFFF	– Non-Linear Force-Free Field
NOAA	– National Oceanic and Atmospheric Administration
NoRH	– Nobeyama Radioheliograph
PFSS	– Potential Field Source Surface
PWF	– Pixelised Wavelet Filtering
QPP	– Quasi Periodic Pulsations
RAM	– Random Access Memory
ROI	– Region Of Interest
SDO	– Solar Dynamics Observatory
SECCHI	– Sun Earth Connection Coronal and Heliospheric Investigation
SoHO	– Solar and Heliospheric Observatory
SSW	– Solar Software
STEREO	– Solar Terrestrial Relation Observatory
SUMER	– Solar Ultraviolet Measurements of Emitted Radiation

SWAVES – STEREO/WAVES
SXR – Soft X-Ray
TRACE – Transition Region and Coronal Explorer
UT – Universal Time
UV – Ultraviolet
VCA – Vertical Current Approximation
VSO – Virtual Solar Observatory

LIST OF SYMBOLS

k_B	–	Boltzman constant
m	–	Mean particle mass
m_e	–	Electron mass
m_p	–	Proton mass
n	–	Total number of particles per unit value
n_e	–	Electron number density
n_i	–	Ion number density
n_p	–	Proton number density
α	–	Force-free function
β	–	Plasma β parameter
γ	–	Ratio of specific heats
η	–	Magnetic diffusivity
μ	–	Mean atomic weight
ρ	–	Mass density of fluid

CONTENTS

	<u>Page</u>
1 INTRODUCTION	1
2 MAGNETOACOUSTIC WAVES	3
2.1 Magnetohydrodynamics Equations	4
2.2 Wave Equation	7
2.3 Dispersion Relation	9
2.4 Waves and Thermal Equilibrium in the Solar Atmosphere	11
2.5 Waves During Transient Events	14
3 FACILITIES FOR OBTAINING AND PROCESSING SOLAR DATA	17
3.1 Solar Dynamics Observatory (SDO)	17
3.1.1 Atmospheric Imaging Assembly (AIA)	18
3.1.2 Helioseismic and Magnetic Imager (HMI)	20
3.1.3 Data Processing	21
4 DATA ANALYSIS METHOD	25
4.1 Wavelet Analysis Evolution	25
4.2 Pixelised Wavelet Filtering (PWF)	29
5 3D MODEL OF WAVES ALONG OF CORONAL LOOPS	37
5.1 Linear Force-Free Field (LFFF) Approximation	37
5.2 Three Dimensional Reconstruction of the Magnetic Field Line	40
5.3 3D Model of Velocity Waves	42
6 NOAA 11272	45
6.1 Active Region Characteristic	45
6.2 Waves Detected	49
6.3 Curve Fitting for Waves Found	79
6.4 Magnetic Field Extrapolation and Waves Velocity	81
6.4.1 Waves Velocity	101
7 CONCLUSIONS AND FINAL REMARKS	107

REFERENCES 111

1 INTRODUCTION

The study of waves in the solar atmosphere began with the attempt to explain the observed Doppler shifts and the broadening of photospheric spectral lines (STEIN; LEIBACHER, 1974). Then, it was established that the acoustic waves contribute to heating of photosphere, chromosphere and low corona (STEIN, 1968; STEIN; SCHWARTZ, 1972). Biermann (1946) and Schwarzschild (1948) suggested for the first time that the acoustic waves generated in the convective zone, provide the heat needed to balance the lost energy by radiation in the chromosphere and corona. Since then, magnetohydrodynamics (MHD) waves in the solar corona have been widely studied (LEROY; SCHWARTZ, 1982; ASCHWANDEN, 2004; MATHIOUDAKIS et al., 2012). Particularly, waves in coronal loops have been recently analysed in quiescent and transient Sun (MOORTELE, 2006; KIM et al., 2012). These waves have been classified, according to their period, phase, amplitude, etc., as kink, sausage, fast or slow magneto-acoustic among other (ROBERTS, 1981a; ROBERTS, 1981b).

In transient Sun regime it is common to see flaring events, and it is interesting to analyse waves associated with them, in some cases in a recursive mode called quasi periodic pulsations (QPP) (NAKARIAKOV; MELNIKOV, 2009). They can be observed in all stages of the flare, in different bands at the same time, and can have periods from seconds to several minutes (NAKARIAKOV et al., 2010a; KUMAR et al., 2016). Actually, the *Atmospheric Imaging Assembly* (AIA) on board the *Solar Dynamics Observatory* (SDO) allows us to observe oscillatory phenomena during transient events (NISTICÒ et al., 2013a). This instrument provides images in ultraviolet (UV) and extreme ultraviolet (EUV), with spatial resolution of 0.6 arcsec and temporal cadence of 12 seconds (LEMEN et al., 2012).

Waves-like oscillations are commonly detected by means of wavelet analysis, which determines period, power, amplitude and phase in temporal signals (MOORTELE et al., 2000a; MOORTELE et al., 2004). The pixelised wavelet filtering (PWF) method applies pixel by pixel the continuous wavelet transform with a Morlet mother function (TORRENCE; COMPO, 1998) in the temporal series of a 3D data cube. This method allows us to analyse spatially and temporally oscillations found through the narrowband dynamic maps (SYCH; NAKARIAKOV, 2008; SYCH et al., 2010).

Many numerical (MENDOZA-BRICEÑO et al., 2004; MORTON et al., 2010; ERDÉLYI; MENDOZA-BRICEÑO, 2004) and observational (WANG et al., 2003a; MOORTELE, 2009) analysis have been carried out, in an attempt to represent the behaviour of waves along the coronal loops. Most of them in 2D.

With the help of *Sun Earth Connection Coronal and Heliospheric Investigation* (SECCHI) on board of *Solar Terrestrial Relation Observatory* (STEREO) mission (HOWARD et al., 2008) it is possible to do a three-dimensional analysis of coronal loops. Some works show results about the waves studied along the loops in 3D, joining SECCHI and AIA images (WHITE; VERWICHTE, 2012; ANFINOGENTOV et al., 2013; VERWICHTE et al., 2013). The magnetic field on these observed lines can be computed using the potential field source surface (PFSS) extrapolation tool (SCHRIJVER, 2001; SCHRIJVER; DE-ROSA, 2003). However, this method can be used only in limited cases because, it is not possible to obtain SECCHI images all time, and the reconstructed loops should be on the solar limb.

In this work, we present a new method for analysing waves along the coronal loops involved in transient events. We chose the active region NOAA 11272 on 17 August 2011, where occurred B and C class flares, and made a three-dimensional model for describing the waves' behaviour along the loops. In order to do this, we detected these waves in images obtained with SDO/AIA, using the PWF method. We extrapolated the magnetic field lines using the Linear Force-Free Field (LFFF) approximation (NAKAGAWA; RAADU, 1972; SELHORST et al., 2008), from the line-of-sight (LOS) magnetograms obtained with the *Helioseismic and Magnetic Imager* (HMI) instrument (SCHERRER et al., 2011) on board of SDO. Thus, we reproduced the field lines that best match with the coronal loops observed in EUV, to study variations of physical parameters along them. Then, we determine temperature, density, acoustic and Alfvén velocities for each height of the line using models for flares (MACHADO et al., 1980), quiet sun (AVRETT; LOESER, 2008) and Solar Software (SSW) routines for automated detection of temperature (ASCHWANDEN et al., 2013).

In order to present the development of our study, we distributed this work as follows: In Chapter 2 we present a theoretical description of MHD waves and their role in the heating of the solar atmosphere. In Chapter 3 we explain the process for obtaining and processing data. Methods used for analysing oscillatory data as PWF and for extrapolating magnetic field lines are described in Chapters 4 and 5, respectively. Description of our results in concerning to active region NOAA 11272 as well as the waves that we found, extrapolated field lines and 3D models for physical parameters of coronal loops are presented in Chapter 6. In the last Chapter, we discuss our results and present the final remarks and perspectives.

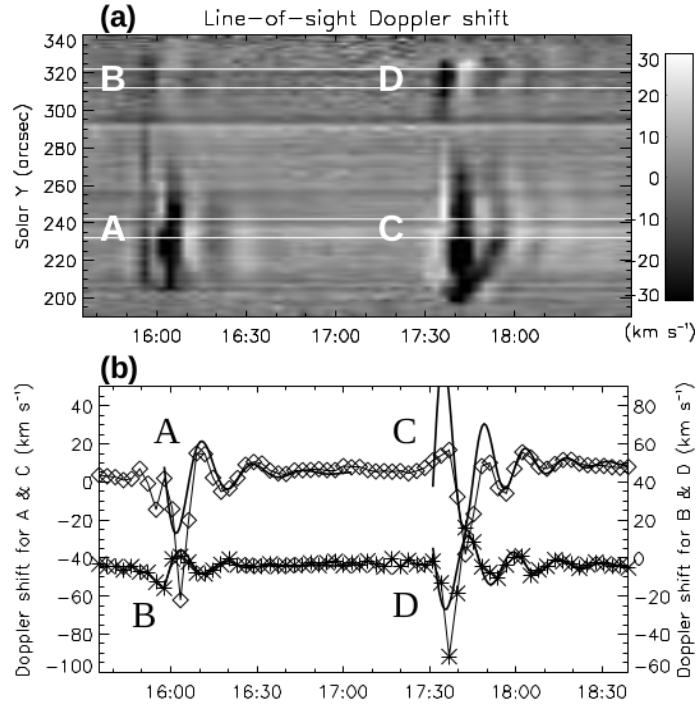
2 MAGNETOACOUSTIC WAVES

The Sun is a dynamic star, so it is natural to find waves as response to many physical processes. The presence of waves in the solar atmosphere is product of restoring forces, which act in opposition to the plasma motion and try to restore the fluid to its original equilibrium. For a fluid in presence of magnetic field, the magnetic tension drives Alfvén waves. Magnetic and plasma pressure acting together generate magneto-acoustic waves (PRIEST, 1982).

The energy deposited by acoustic waves may keep the thermal equilibrium between photosphere and low corona (ULMSCHNEIDER, 1970; STEIN; LEIBACHER, 1974; MCWHIRTER et al., 1975; NARAIN; ULMSCHNEIDER, 1996; WALSH; IRELAND, 2003), but in some parts of chromosphere and to inner of corona, where the plasma is magnetically dominated, the MHD waves play a very important role to balance the lost of energy by radiation (KHODACHENKO et al., 2004; NAKARIAKOV; VERWICHTE, 2005).

Many ground-based observatories such as *Nobeyama Radioheliograph* (NoRH) and space-borne (e.g., SDO) have been used for detecting oscillatory phenomena. For example, Walsh and Ireland (2003) studied magneto-acoustic waves using data from the *Extreme Ultraviolet Imaging Telescope* (EIT) on board of *Solar and Heliospheric Observatory* (SoHO), in the Fe XII line at 195 Å. Waves of 5 minutes were detected with the *Transition Region and Coronal Explorer* (TRACE) in 171 Å and with the *Coronal Diagnostic Spectrometer* (CDS) in the He I, O V and Mg IX lines (MOORTELE et al., 2000b; ROBBRECHT et al., 2001; MARSH et al., 2003). Fast and slow waves propagating simultaneously along the same path were observed in images of SDO/AIA (ZHANG et al., 2015). Kliem et al. (2002) and Wang et al. (2003a) detected quasi periodic oscillations through a Doppler shift in the Fe XIX and Fe XXI emission lines, observed by the spectral instrument *Solar Ultraviolet Measurements of Emitted Radiation* (SUMER), see Figure 2.1(a). These oscillations have $c_s = 370 \text{ km s}^{-1}$, periods in the range 7–31 minutes and decay times of 5.7–36.8 minutes. Observations of Doppler shift in UV emission lines showed that the solar corona can be heated by waves generated under it (ATHAY; WHITE, 1978; BRUNER JR., 1978).

Figure 2.1 - Doppler shift in the Fe XIX line observed with SOHO/SUMER on 9 March 2001.



(a) Waves observed through the LOS Doppler shift. (b) Time series for Doppler shift in the oscillatory event for points AC and BD of panel (a).

SOURCE: Wang et al. (2003a)

2.1 Magnetohydrodynamics Equations

We present a standard mathematical discussion about magneto-acoustic waves, e.g., see Ferraro and Plumpton (1966), Priest (1982), Mihalas and Mihalas (1984), Landau and Lifshitz (1987). In the most simple form, it is assumed a plasma frozen to the magnetic field lines, thermally insulated obeying the adiabatic law ($p/\rho^\gamma = \text{cte}$), the medium should be homogeneous and isotropic, and fluxes with $\mathbf{v}_0 = \mathbf{0}$ are not considered, i.e., the density and magnetic field only depend on the spatial coordinates.

At the beginning, the plasma in thermal and hydrodynamic equilibrium is slightly perturbed and then is analysed whether the resulting disturbance propagates as a wave or not. For that, the ideal MHD equations are used. In order to avoid phenomena associated with the non linearity regime, as turbulence, we restrict our presentation only to the linear regime and the perturbation of thermodynamics quantities

$(\rho, T \text{ e } p)$ is assumed to vary like $\sim \exp[i(kx - \omega t)]$. Then, the wave equation and dispersion relation are found.

As follow, the ideal MHD equations for an homogeneous, isotropic, adiabatic, of infinite extent medium and without external forces acting over it are presented. In these equations a volume element V_0 whose boundary surface lies entirely within the fluid is considered.

The *Equation of Continuity* express the conservation of matter, i.e., the mass contained within the volume V_0 always should be the same

$$\frac{\partial \rho}{\partial t} + \frac{\partial(\rho v_i)}{\partial x_i} = 0, \quad (2.1)$$

where ρ is the mass density and v_i is the i^{th} component for velocity with $i = 1, 2, 3$. We are using the *Einstein summation notation* for the indices.

The *Momentum Equation* describes the principle of conservation of linear momentum, which says that the rate of change of the momentum associated with the volume element is equal to the forces acting on it, e.g., in our case, the pressure and the magnetic force

$$\rho \left(\frac{\partial v_i}{\partial t} + v_j \frac{\partial v_i}{\partial x_j} \right) = -\frac{\partial p}{\partial x_i} + \frac{1}{4\pi} \left[B_k \frac{\partial B_i}{\partial x_k} - \frac{1}{2} \frac{\partial(|B|^2)}{\partial x_i} \right], \quad (2.2)$$

where p is the gas pressure and B_i is the i^{th} component of magnetic field.

On the other hand, the *Energy Equation* describes the law of conservation of energy. The rate of change of heat received by the volume element should be equal to the heat dissipated by it. Because in the ideal form, the fluid is adiabatic, then dissipative processes are not considered

$$\frac{\partial p}{\partial t} + v_j \frac{\partial p}{\partial x_j} - c_s^2 \left(\frac{\partial \rho}{\partial t} + v_j \frac{\partial \rho}{\partial x_j} \right) = 0, \quad (2.3)$$

where c_s is the velocity of sound to constant entropy s , i.e.,

$$c_s^2 = \left(\frac{\partial p}{\partial \rho} \right)_s. \quad (2.4)$$

The *Equation of State* relates the pressure, temperature and density of a fluid. A particular case of this equation is called *perfect gas law*

$$p = \frac{k_B}{m} \rho T, \quad (2.5)$$

where k_B is the Boltzmann constant, $m = \mu m_p$ is the mean particle mass, μ is the mean atomic weight, m_p is the proton mass, and T is the temperature. In this work we conveniently express the density as $\rho = mn$, where $n = n_{ion} + n_e$ is the total number of particles per unit volume, n_{ion} and n_e are the ion and electron number densities respectively. Thus, the Equation (2.5) may be expressed as

$$p = \frac{\gamma k_B}{\mu m_p} T, \quad (2.6)$$

where γ is the ratio of specific heats for a given adiabatic equation of state. For fully-ionized gases $\gamma = 5/3$. In the solar atmosphere $\mu \approx 0.6$ and $n \approx 1.9n_e$, except near to the photosphere (PRIEST, 1982). In the solar corona $\mu \approx 1.27$, $n \equiv n_p + n_e = 2n_e$, and $\rho \equiv n_p m_p + n_e m_e \approx n_e m_p$, where n_p and m_e are the proton number density and the electron mass respectively (ASCHWANDEN, 2004).

The magnetic field behaviour is governed by the *Induction Equation* (Equation 2.7). This depends on the magnetic Reynolds number $R_m = l_0 v_0 / \eta$, with l_0 the length-scale, v_0 the plasma speed and η the magnetic diffusivity. In this case $R_m \gg 1$, i.e., the plasma satisfies the frozen-flux theorem (the magnetic field lines move with the plasma perfectly conducting) (PRIEST, 1982)

$$\frac{\partial B_i}{\partial t} = B_j \frac{\partial v_i}{\partial x_j} - \frac{\partial v_j}{\partial x_j} B_i - v_j \frac{\partial B_i}{\partial x_j}. \quad (2.7)$$

Finally, it is considered the *Gauss' Law* for magnetism, which determines that magnetic monopoles do not exist

$$\frac{\partial B_i}{\partial x_i} = 0. \quad (2.8)$$

Because the perturbation is adiabatic, variations in the material properties may be related through the density, temperature and pressure taking the entropy constant (MIHALAS; MIHALAS, 1984), i.e.,

$$\delta\rho = \frac{\delta p}{c_s^2}. \quad (2.9)$$

For an ideal gas, the pressure adiabatic behaviour is described by

$$p = p_0 \left(\frac{\rho}{\rho_0} \right)^\gamma. \quad (2.10)$$

Then, (2.4) becomes

$$c_s^2 = \frac{p_0}{\rho_0} \gamma \left(\frac{\rho}{\rho_0} \right)^{\gamma-1}. \quad (2.11)$$

Because the temperature in this conditions is

$$\frac{T}{T_0} = \left(\frac{\rho}{\rho_0} \right)^{\gamma-1} \quad (2.12)$$

and using the Equation (2.6) we can see that the sound velocity c_s depends only on the temperature

$$c_s^2 = \frac{p_0}{\rho_0 T_0} \gamma T = \frac{k_B}{\mu m_p} \gamma T. \quad (2.13)$$

2.2 Wave Equation

At the beginning, the fluid is at rest ($\mathbf{v}_0 = \mathbf{0}$) and in equilibrium. Thus, we can consider the physical quantities ρ_0 , p_0 , \mathbf{B}_0 , and T_0 as constant.

In order to study the wave motion, we linearised the magnetohydrodynamic Equations (2.1)–(2.8). For that, we considered small perturbations departing from the equilibrium $\rho = \rho_0 + \delta\rho$, $p = p_0 + \delta p$, $T = T_0 + \delta T$, $B = B_0 + \delta B$, and $\delta\mathbf{v}$, where $|\delta\rho/\rho_0| \ll 1$, $|\delta p/p_0| \ll 1$, $|\delta T/T_0| \ll 1$, $|\delta B/B_0| \ll 1$, and $|\delta\mathbf{v}|/c_s \ll 1$ (MIHALAS; MIHALAS, 1984; LANDAU; LIFSHITZ, 1987). Hence, without considering second and

higher order terms, the equations of continuity, momentum, energy, state, induction, and Gauss' law become respectively

$$\frac{\partial \delta \rho}{\partial t} + \rho_0 \frac{\partial \delta v_i}{\partial x_i} = 0, \quad (2.14)$$

$$\rho_0 \frac{\partial \delta v_i}{\partial t} = -\frac{\partial \delta p}{\partial x_i} + \frac{1}{4\pi} \left[B_{0k} \frac{\partial \delta B_i}{\partial x_k} - \frac{\partial}{\partial x_i} (B_{0j} \delta B_j) \right], \quad (2.15)$$

$$\frac{\partial \delta p}{\partial t} - c_s^2 \frac{\partial \delta \rho}{\partial t} = 0, \quad (2.16)$$

$$\frac{\delta p}{p_0} = \frac{\delta \rho}{\rho_0} + \frac{\delta T}{T_0}, \quad (2.17)$$

$$\frac{\partial \delta B_i}{\partial t} = \left(B_{0k} \frac{\partial}{\partial x_k} \right) \delta v_i - B_{0i} \frac{\partial \delta v_k}{\partial x_k}, \quad (2.18)$$

$$\frac{\partial \delta B_i}{\partial x_i} = 0. \quad (2.19)$$

The wave equation for density, pressure and velocity come to be

$$\frac{\partial^2 \delta \rho}{\partial t^2} = c_s^2 \frac{\partial^2 \delta \rho}{\partial x_i^2} - \frac{1}{4\pi} \left[B_{0k} \frac{\partial}{\partial x_k} \frac{\partial \delta B_i}{\partial x_i} - B_{0k} \frac{\partial^2 \delta B_k}{\partial x_i^2} \right], \quad (2.20)$$

$$\frac{\partial^2 \delta p}{\partial t^2} = c_s^2 \frac{\partial^2 \delta p}{\partial x_i^2} - \frac{1}{4\pi} \left[B_{0k} \frac{\partial}{\partial x_k} \frac{\partial \delta B_i}{\partial x_i} - B_{0k} \frac{\partial^2 \delta B_k}{\partial x_i^2} \right], \quad (2.21)$$

$$\frac{\partial^2 \delta v_i}{\partial t^2} = -c_s^2 \frac{\partial}{\partial x_i} \frac{\partial \delta v_j}{\partial x_j} + \frac{1}{4\pi \rho_0} \{ [\nabla \times [\nabla \times (\delta \mathbf{v} \times \mathbf{B}_0)] \times \mathbf{B}_0 \}_i, \quad (2.22)$$

where the second term on the right-hand side of Equation (2.22) may be expressed in component as

$$\begin{aligned}
& \frac{1}{4\pi\rho_0} \left[B_{0j} \left(B_{0k} \frac{\partial}{\partial x_k} \right) \frac{\partial \delta v_i}{\partial x_j} + \left(B_{0k} \frac{\partial}{\partial x_k} \right)^2 \delta v_i - B_{0i} \left(B_{0k} \frac{\partial}{\partial x_k} \right) \frac{\partial \delta v_j}{\partial x_j} \right. \\
& - \frac{\partial \delta v_j}{\partial x_j} B_{0k} \frac{\partial B_{0i}}{\partial x_k} - B_{0k} \left(\delta v_j \frac{\partial}{\partial x_j} \right) \frac{\partial \delta v_i}{\partial x_i} - B_{0l} \left(\frac{\partial \delta v_l}{\partial x_j} \right) \frac{\partial B_{0j}}{\partial x_i} \\
& + B_{0l}^2 \frac{\partial}{\partial x_i} \frac{\partial \delta v_j}{\partial x_j} + \frac{1}{2} \frac{\partial (B_{0l}^2)}{\partial x_i} \frac{\partial \delta v_j}{\partial x_j} \\
& \left. + B_{0l} \left(\delta v_j \frac{\partial}{\partial x_j} \right) \frac{\partial B_{0j}}{\partial x_i} + B_{0l} \frac{\partial}{\partial x_i} \left(\delta v_j \frac{\partial}{\partial x_j} \right) B_{0l} \right].
\end{aligned}$$

The Equations (2.20)-(2.22) permit plane-wave solutions of the form $\sim \exp[i(k_j x_j - \omega t)]$. Hence, the solutions for density, pressure, velocity, and magnetic field perturbed are described as

$$\begin{aligned}
\delta \rho &= \tilde{\rho} \exp[i(k_j x_j - \omega t)], \\
\delta p &= \tilde{p} \exp[i(k_j x_j - \omega t)], \\
\delta v_m &= \tilde{v}_m \exp[i(k_j x_j - \omega t)], \\
\delta B_m &= \tilde{B}_m \exp[i(k_j x_j - \omega t)],
\end{aligned} \tag{2.23}$$

where, $\tilde{\rho}$, \tilde{p} , \tilde{v}_m , and \tilde{B}_m are constants. The wave number k is the magnitude of wave vector \mathbf{k} , and ω represents the angular frequency. For these waves $P = 2\pi/\omega$, $\lambda = 2\pi/k$ and $\hat{\mathbf{k}} \equiv \mathbf{k}/k$ represent the period, wavelength, and direction of the wave propagation respectively.

2.3 Dispersion Relation

Dispersion relation defines the frequency as a function of the wave number and the angle (θ_B) between the equilibrium magnetic field and the wave vector (PRIEST, 1982). For magneto-acoustic waves, we only take into account the plasma pressure and the magnetic force in the MHD equations. Considering that the perturbations in the fluid are propagating only along the x axis, the direct substitution of Equations 2.23 into the wave Equation 2.22 yields to

$$\omega^4 - \omega^2 k^2 (c_s^2 + v_A^2) + c_s^2 v_A^2 k^4 \cos^2 \theta_B = 0, \tag{2.24}$$

where v_A is the Alfvén velocity (FERRARO; PLUMPTON, 1966; ASCHWANDEN, 2004)

$$v_A = \frac{B}{\sqrt{4\pi\mu m_p n}}. \quad (2.25)$$

For outward-propagating waves ($\omega/k > 0$) exist two different solutions of Equation (2.24)

$$v_{ph\pm} = \left(\frac{\omega}{k}\right)_{\pm} = \left[\frac{1}{2}(c_s^2 + v_A^2) \pm \frac{1}{2}\sqrt{c_s^4 + v_A^4 - 2c_s^2v_A^2 \cos 2\theta_B}\right]^{1/2}. \quad (2.26)$$

These solutions define the phase velocity ($v_{ph\pm}$) and from there the group velocity (v_g), i.e.,

$$v_{ph\pm} = \left(\frac{\omega}{|\mathbf{k}|}\right)_{\pm}, \quad v_g = \nabla_{\mathbf{k}}\omega. \quad (2.27)$$

Thus, one solution to the Equation (2.24) corresponds to the high frequencies mode, called *fast magneto-acoustic waves* and the other one to *slow magneto-acoustic waves*, which refers to the low frequencies mode. The Alfvén velocity is between the fast and slow modes, then sometimes is called *intermediate mode* (PRIEST, 1982).

For coronal loops, the phase velocity in the fundamental mode (WANG, 2006) is defined as:

$$v_{ph} = \frac{2L}{P}, \quad (2.28)$$

where L represents the loop length.

The magneto-acoustic waves may be considered as sound waves modified by the magnetic field and as compressional Alfvén waves modified by the plasma pressure. These modifications depend of angle θ_B . Other important considerations are:

- perturbations along the magnetic field, $\theta_B = 0$

$$\begin{aligned}v_{ph+} &= c_s \\v_{ph-} &= v_A\end{aligned}$$

- perturbation across the magnetic field, $\theta_B = \pi/2$

$$\begin{aligned}v_{ph+} &= (c_s^2 + v_A^2)^{1/2} \\v_{ph-} &= 0\end{aligned}$$

- slow magneto-acoustic waves, as $\theta_B \rightarrow \pi/2$, $v_{ph} \rightarrow 0$, but

$$\frac{\omega}{k_B} \equiv \frac{\omega}{k \cos \theta_B} \rightarrow c_T \equiv \frac{v_A c_s}{(v_A^2 + c_s^2)^{1/2}},$$

where c_T is the cusp velocity for v_g , which represents the component of v_{ph} along \mathbf{B} for perturbations almost perpendicular to the magnetic field (PRIEST, 1982).

- If the magnetic field vanishes, $v_A = 0$, the slow wave disappears and the fast wave becomes a sound wave. On the other hand, if the pressure vanishes, $c_s = 0$, the slow wave disappears and the fast wave becomes a compressional Alfvén wave (ROBERTS, 1981b).

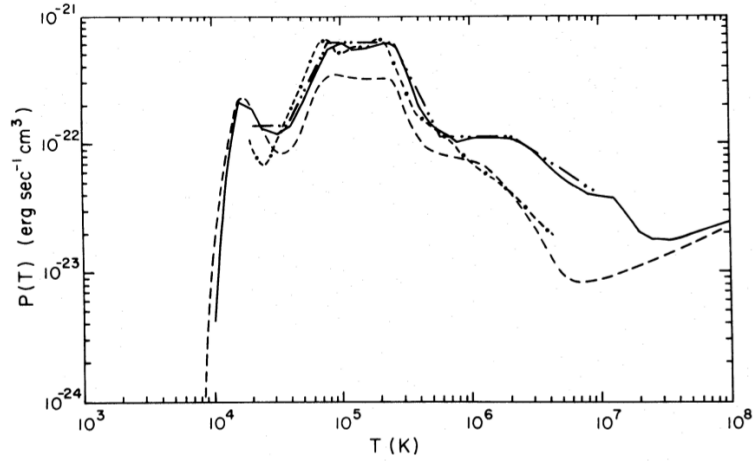
When $v_A \ll c_s$, the group velocities become $v_A \hat{\mathbf{B}}_0$ and $c_s \hat{\mathbf{k}}$ for slow and fast waves respectively. On the other hand, the $v_A > c_s$ case have been observed for coronal conditions, with $v_A \approx 1000 \text{ km s}^{-1}$ and $c_s \approx 200 \text{ km s}^{-1}$ for $T = 1.5 \text{ MK}$ plasma (ASCHWANDEN, 2004).

2.4 Waves and Thermal Equilibrium in the Solar Atmosphere

The thermal equilibrium in the solar atmosphere is determined by the energy transfer processes (KOOP, 1968). The energy can be transported through the different atmosphere layers by convective F_{conv} , radiative F_{rad} or acoustic F_{ac} fluxes (KUPERUS, 1969; KUPERUS et al., 1981).

Chromosphere and corona loss energy mainly by radiation of optically thin plasma (MCWHIRTER et al., 1975; ROSNER et al., 1978). In Figure 2.2 are shown different radiative loss functions $P(T)$ in the plasma of solar atmosphere (POTTASCH, 1965; ROSNER et al., 1978).

Figure 2.2 - Radiative loss functions for chromospheric and coronal plasma.

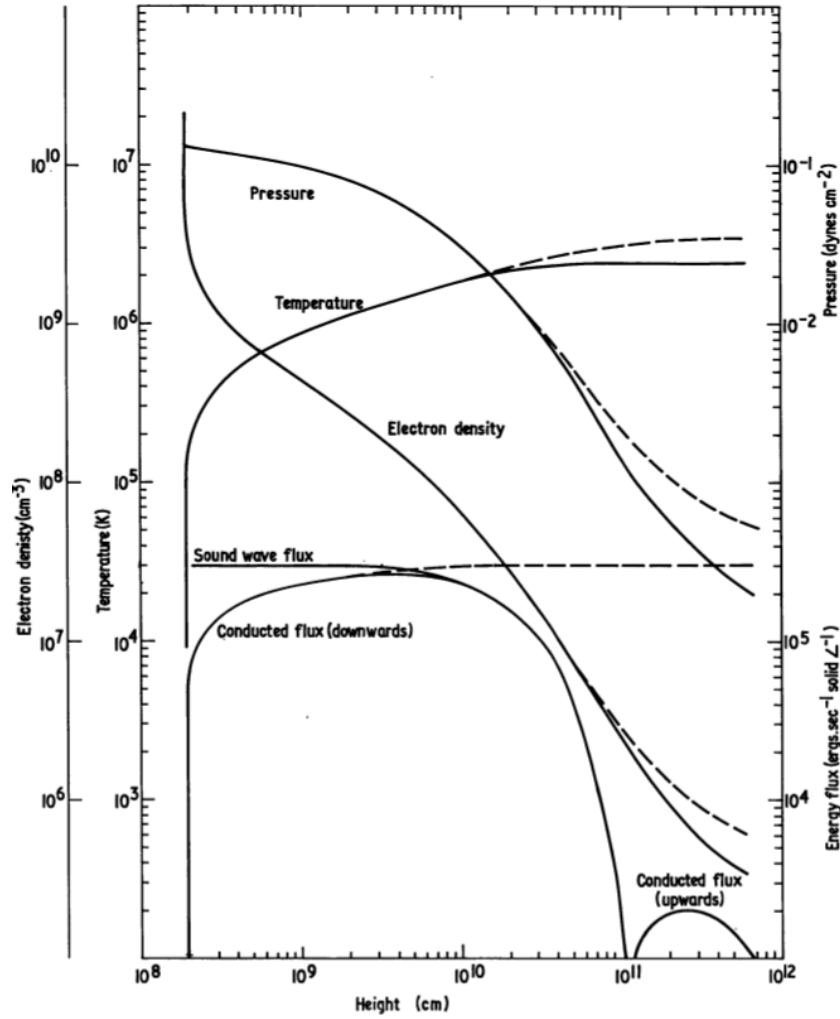


Radiative loss energy as a function of temperature (ROSNER et al., 1978) [$\cdot \cdot - \cdot \cdot$]. This function was compared with results obtained by Pottasch (1965) [$\cdot - - \cdot$] and McWhirter et al. (1975)[$- - -$].

SOURCE: Rosner et al. (1978)

On the other hand, the model made by McWhirter et al. (1975) shows the balance of energy in the solar corona. In Figure 2.3 are presented the height distribution for pressure, density, temperature and flux of energy (solid lines). The curves show that in transition region the pressure is maintained relatively constant, while the temperature and density values vary rapidly with the height. For heights greater than 10^{12} cm (dashed line), other mechanisms for coronal heating different of dissipation of acoustic waves may deposit energy in the solar atmosphere. To reach the thermal equilibrium in the solar corona it is necessary an input of mechanical energy flux of 3×10^5 ergs $\text{cm}^{-2} \text{s}^{-1}$ (MCWHIRTER et al., 1975; BOHM-VITENSE, 1987).

Figure 2.3 - Model for the solar corona based on energy balance.



Standard model for the solar corona heating (solid line). The dashed lines represent energy deposited at heights greater than 10^{12} cm.

SOURCE: McWhirter et al. (1975)

In addition, the energy dissipation of acoustic waves by viscosity, thermal conduction or shock waves are important for regions with $\beta = (8\pi p/B^2) \gtrsim 1$ (KUPERUS et al., 1981). However, for magnetized plasma $\beta \ll 1$, magneto-acoustic waves may be an important mechanism of heating (NAKARIAKOV; VERWICHTE, 2005; ERDÉLYI; BALLAI, 2007). Acoustic waves can generate sufficient energy for explaining coronal temperatures of $1.5 - 2 \times 10^6$ K, but for higher values the plasma needs an energy flux two orders of magnitude greater than the observed. This means that coronal regions not perturbed are heated by other dissipative mechanisms (JAGER; KUPERUS, 1961).

2.5 Waves During Transient Events

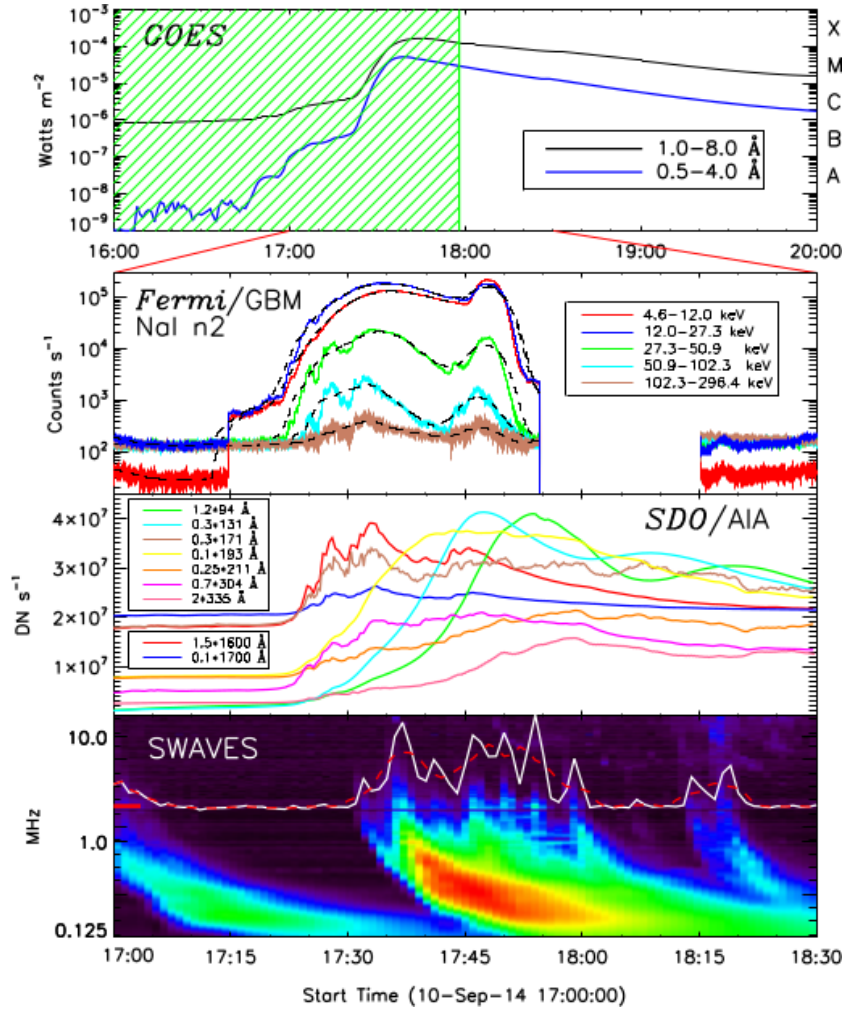
Oscillatory processes in the Sun, related with transient events, have been studied since many years ago. [Kosovichev and Zharkova \(1998\)](#) announced for first the time that flares affect the Sun's interior generating seismic waves similar to earthquakes. Since then, other studies were realized in attempt to explain how the flares generate waves in the Sun ([BEŞLIU-IONESCU et al., 2006](#); [MARTÍNEZ-OLIVEROS et al., 2008](#)).

In the solar atmosphere it is common to find flares containing QPP ([NAKARIAKOV; MELNIKOV, 2009](#)). They can be observed in all stages of the flares and in all emission bands from radio to gamma-rays ([SYCH et al., 2009](#); [SU et al., 2012](#); [SHEN; LIU, 2012](#); [NAKARIAKOV et al., 2010a](#); [KUMAR et al., 2016](#)). They can be associated with MHD auto-oscillations because their observed modulation depth, period, and anharmonicity ([NAKARIAKOV et al., 2010b](#)).

Figure 2.4 shows the QPP spectra of X1.6 flare observed in NOAA 12158 on 2014 September 10. This flare was registered by the *Geostationary Operational Environmental Satellite* (GOES) ([MACHOL, 2016](#)), and observed by the *Interface Region Imaging Spectrograph* (IRIS) ([PONTIEU et al., 2014](#)), *Fermi Gamma-ray Burst Monitor* (GBM), SDO/AIA, STEREO/WAVES (SWAVES), at soft X-ray (SXR), hard X-ray (HXR), UV, EUV, and radio wavelengths ([LI et al., 2015](#)).

The QPP excited by flares can be detected in the modulation of flare emission which can be generated by standing and travelling waves ([NAKARIAKOV; MELNIKOV, 2009](#)). Fast and slow magneto-acoustic waves represent a mechanism for periodic triggering of magnetic reconnection ([MCLAUGHLIN; HOOD, 2004](#); [CHEN; PRIEST, 2006](#)) which generate MHD turbulence and hence periodically can perturb the flare neighbouring plasma, modulating its rate, and producing QPP.

Figure 2.4 - QPP Spectra of X1.6 class flare



Flare observed from 16:00 UT to 20:00 UT on 2014 September 10. **Top:** GOES SXR flux. **Second:** X-ray light curves from Fermi/GBM at five energy channels. **Third:** AIA light curves integrated from the flare region. **Bottom:** radio dynamic spectra between 0.125 and 16.075 MHz from SWAVES.

SOURCE: Li et al. (2015)

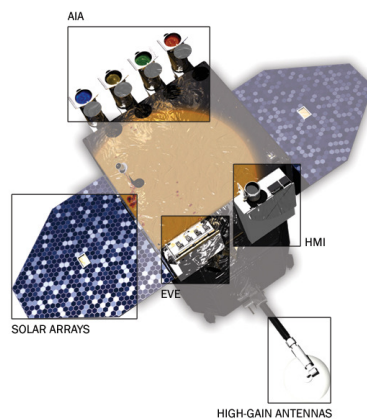
3 FACILITIES FOR OBTAINING AND PROCESSING SOLAR DATA

3.1 Solar Dynamics Observatory (SDO)

SDO is a spacecraft of the National Aeronautics and Space Administration's (NASA) Living With a Star (LWS) program. This provides data since 2010, which let us to study the solar variations and establishing their consequences on the Earth's climate and technological system (PESNELL et al., 2012). The spacecraft contain solar panels that produce 1500 W of power, high-gain antennas for transmitting the raw data to two ground stations in New Mexico, for the following instruments (see Figure 3.1) :

- AIA is an array of four telescopes that provide full-disk images of the solar corona in UV and EUV band passes every 12 seconds or less (LEMEN et al., 2012).
- *Extreme Ultraviolet Variability Experiment* (EVE) measures the EUV spectral irradiance with unprecedented spectral resolutions, temporal cadence, accuracy and precision (WOODS et al., 2012).
- HMI provides full-disk, high-cadence Doppler, intensity and magnetic images of the solar photosphere (SCHERRER et al., 2011).

Figure 3.1 - Design of Solar Dynamics Observatory.



Distribution of AIA, EVE and HMI instruments on board of SDO, high-gain antennas and solar arrays.

SOURCE: Courtesy of <http://sdo.gsfc.nasa.gov>

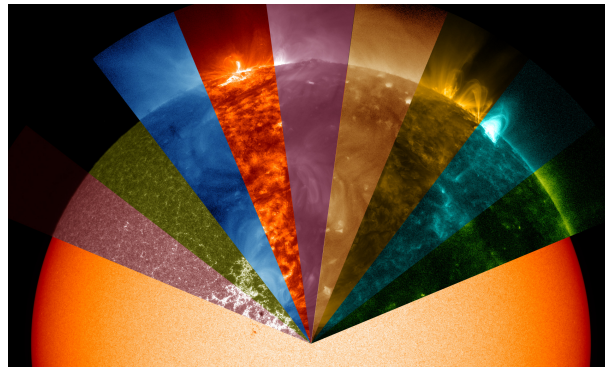
In this work we study waves on Sun’s magnetic field structures and then, we only use data from AIA and HMI instruments. They are described in more detail below.

3.1.1 Atmospheric Imaging Assembly (AIA)

Transient events as flares change rapidly the magnetic field configuration and plasma characteristic of solar corona. These processes occur on short time scales and for understanding them it is necessary to use instruments that offer data with high temporal cadence and good spatial resolution.

AIA instrument, was designed to study the dynamic of Sun’s magnetic field and the coronal response to this. AIA consists of four Cassegrain telescopes optimized to observe solar emissions from the temperature minimum region to the corona, in a range of temperatures from 6×10^4 K to 2×10^7 K (LEMEN et al., 2012). Full-disk AIA images have dimensions of 4096×4096 pixels, high spatial resolution ($0.6''$) and temporal cadence of approximately 10–12 seconds, sometimes with cadence of 8 seconds to study energetic transient phenomena.

Figure 3.2 - Sun’s image in the band passes of AIA.



The Sun observed by AIA in nine wavelengths. The mosaic shows Sun’s parts in two UV and seven EUV band passes on the background 4500 \AA continuum. These parts are distributed from left to right as 1700, 1600, 335, 304, 211, 193, 171, 131 and 94 \AA .

SOURCE: Courtesy of <http://sdo.gsfc.nasa.gov>

Figure 3.2 shows a Sun mosaic observed by SDO/AIA in different band passes. The background is 4500 \AA in the continuum, where the region observed is the photosphere. From left to right the band passes 1700 and 1600 \AA in UV, 335, 304, 211, 193, 171, 131 and 94 \AA in EUV are observed. Details of regions and characteristic

emission temperature of instrument are presented in Table 3.1.

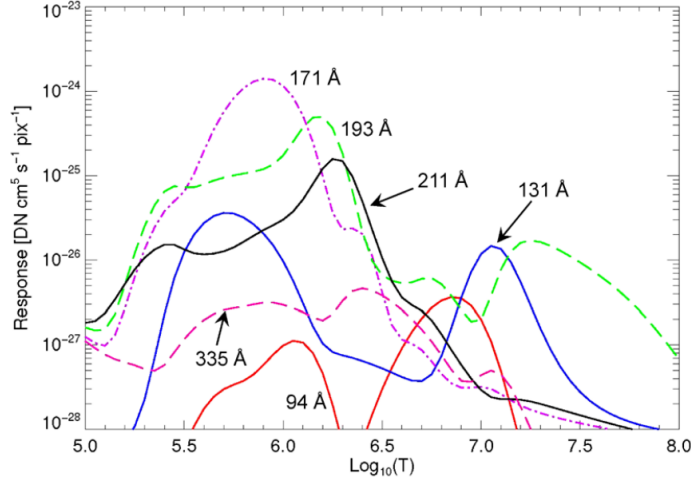
Table 3.1 - Distribution of wavelengths, lines, regions, and temperatures observed by AIA.

Channel	Primary ion(s)	Region of atmosphere	Char. log(T)
4500 Å	continuum	photosphere	3.7
1700 Å	continuum	temperature minimum, photosphere	3.7
1600 Å	C IV + continuum	transition region, upper photosphere	5.0
304 Å	He II	chromosphere, transition region	4.7
171 Å	Fe IX	quiet corona, upper transition region	5.8
193 Å	Fe XII, XXIV	corona and hot flare plasma	6.2,7.3
211 Å	Fe XIV	active-region corona	6.3
335 Å	Fe XVI	active-region corona	6.4
94 Å	Fe XVIII	flaring corona	6.8
131 Å	Fe VIII, XXI	transition region, flaring corona	5.6, 7.0

SOURCE: [Lemen et al. \(2012\)](#)

The filter response for UV and EUV channels of AIA is computed using the CHIANTI solar spectral model. This is an atomic database for emission lines made to calculate the temperature, atomic energy levels, wavelengths, radiative and electron excitation data using programs written in interactive data language (IDL) ([DERE et al., 1997](#)). In particular, the emissivity and temperature response functions are computed using CHIANTI version 7.1 and we can obtain them using the SSW routine *aia_get_response.pro*. As was showed in Table 3.1, the iron emission line dominates in six EUV band passes (171, 193, 211, 335, 94, and 131 Å). In Figure 3.3 are showed the temperature response functions for the EUV channels of AIA.

Figure 3.3 - Temperature response functions for six EUV channels.



Temperature response functions for the AIA EUV channels that are dominated by iron emission lines calculated from the effective-area functions and assuming CHIANTI model for the solar emissivity.

SOURCE: [Lemen et al. \(2012\)](#)

3.1.2 Helioseismic and Magnetic Imager (HMI)

The HMI instrument was designed to study the convection-zone dynamics, the solar dynamo, and the solar magnetic activity of the corona and heliosphere. Measurements are made in form of filtergrams in a set of polarizations and spectral-line positions at a regular cadence during the emission ([SCHERRER et al., 2011](#)). The scientific data produced can be divided into five main areas: global and local helioseismology, line-of-sight and vector magnetography, and continuum-intensity studies.

For this work we used full-disk (4096×4096 pixel) LOS magnetograms with $0.5''$ spatial resolution and temporal cadence of 45 seconds. They were obtained at level 1.5, which are made from level 1.0 filtergrams, i.e., with bad-pixel removal, flat-fielding, and quality assessment checks ([ROSA; SLATER, 2015](#)). Figure 3.4 shows the corresponding magnetogram for NOAA 11272 which was observed by AIA instrument in 171 \AA .

Figure 3.4 - LOS magnetogram and EUV image of NOAA 11272.

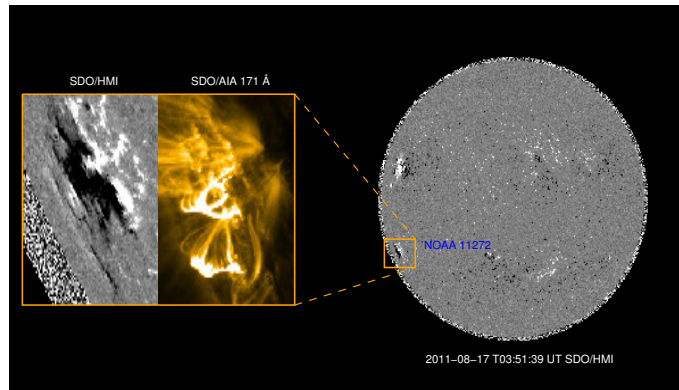


Image of active region obtained by HMI and AIA instruments. **Left:** Image of active region from HMI and AIA in 171 Å. **Right:** Full-disk magnetogram of the Sun. Orange box indicates the place of NOAA 11272.

SOURCE: Author production

3.1.3 Data Processing

The data obtained by SDO/AIA are transmitted via Ka-band telemetry to two ground stations in White Sands, New Mexico. From there, the data are transferred by broad-band circuits to the Stanford University campus where are permanently archived in the *Joint SDO Operations Center–Science-Data Processing* (JSOC-SDP) facility (BOERNER et al., 2012). Science operations for both AIA and HMI are controlled from the *Instrument Operations Center at Lockheed Martin Solar and Astrophysics Laboratory’s* (LMSAL).

Level 0 data recorded in JSOC-SDP are processed and converted to Level 1.0. This process include the follow steps (LEMEN et al., 2012):

- To remove the “over-scan” included in the readout format of files. This is using for monitoring the charge transfer efficiency in the charge coupled device (CCD) and it is only for engineering purposes.
- To remove CCD dark images, read noise and dark current.
- To apply a flat-field correction to the AIA images.
- To correct the pixels that do not respond correctly to the light (bad pixels), replacing by interpolated values from neighboring pixels.

- To remove the “spikes” that appear as result of the interaction of energetic particles with the instrument and to rise the number of high energy photons detected in the CCD.
- To flip the image so as to put solar north at the top of the array.

Level 1.0 data are freely available as flexible image transport system (FITS) files in different websites (see Table 3.2) approximately 48 hours after receipt at the JSOC. The data may be download using the SSW routines (FREELAND; BENTLEY, 2000).

Table 3.2 - Information about AIA data adquisition at websites.

Function	Name site	Site
To browse data	The Sun Now	http://sdo.gsfc.nasa.gov/data/
	Sun in Time	http://sdowww.lmsal.com/
	Solar Monitor	https://solarmonitor.org/
	Helioviewer Project	http://www.helioviewer.org/
To find data	Heliophysics Events Knowledgebase	http://www.lmsal.com/hek/
	iSolSearch	http://www.lmsal.com/isolsearch
	Joint Science Operations Center	http://jsoc.stanford.edu/ http://jsoc.stanford.edu/ajax/lookdata.html http://jsoc.stanford.edu/ajax/exportdata.html
To get data	The Cutout Service	http://www.lmsal.com/get_aia_data/
	The Virtual Solar Observatory	http://sdac.virtualsolar.org/cgi/search

SOURCE: Rosa and Slater (2015)

The images can be read with *read_sdo.pro* routine and used at level 1.0. For making videos and analysing a sequence of frames is necessary to prepare the images, i.e., convert the level 1.0 to level 1.5 with *aia_prep.pro* routine (BROWN et al., 2011; ROSA; SLATER, 2015). In addition to the calibration made in level 1.0, this process includes procedures to:

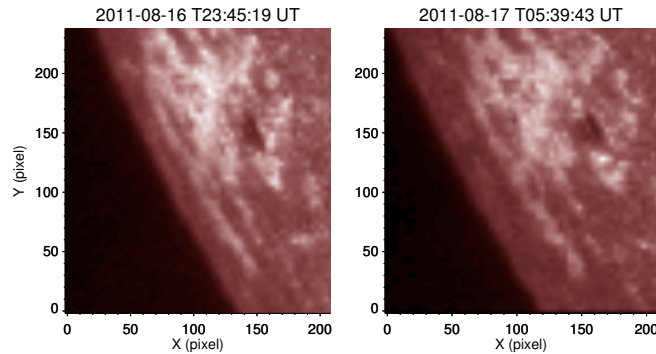
- Correct the roll angle. The images are rotated so that solar North is at 0°, i.e., at the top of the image array.
- Adjust the plate-scale to 0.6 arcsecs per pixel for all AIA’s telescopes.

- Remove the residual differences of the alignment adjust in the bore-sight pointing of each telescope.

In this work we obtained AIA and HMI data in level 1.0 and 1.5 format, respectively. For this, we used the informational resource Heliophysics Coverage Registry (the cutout service) and consequently obtained sub-fields of images in EUV and UV for NOAA 11272. For getting HMI data, we used the *Virtual Solar Observatory* (VSO) service. AIA level 1.0 data were processed using the *read_sdo.pro* and *aia_prep.pro* SSW routines. In addition, we used the *aia_prep.pro* routine to process HMI Level 1.5 data and to co-align their with AIA Level 1.5, because the plate scales between HMI and AIA images are different.

We obtained data for six hours of observation, so the region of interest may move out of the field of view as the Sun rotates. To maintain the region inside the same field of view (FOV), was necessary to calculate the region position as it rotates across the solar disk during the observation time. For that, we used the *rot_xy.pro* function (BROWN et al., 2011) and with the new position we established the coordinates for clipping the region correctly. Thus, we analysed level 1.5 data aligned and in the same FOV. In Figure 3.5 we present the first and the last image of 1700 Å data set used for our analysis. These images were aligned using *rot_xy.pro* function to keep them in the same FOV.

Figure 3.5 - Tracking of NOAA 11272 observed by AIA in 1700 Å.



Tracking of active region observed during six hours, from 2011-08-16 at 23:45 UT (**left-hand**) to 2011-08-17 at 05:49 UT (**right-hand**). The region was aligned using the function *rot_xy.pro*.

SOURCE: Author production

4 DATA ANALYSIS METHOD

It is not an easy task to detect waves in the solar atmosphere, mainly because they occur in the threshold of instrumental detectability. Hence, it is necessary to obtain data with the best spatial resolution and temporal cadence (SYCH; NAKARIAKOV, 2008). Fortunately, data obtained from SDO/AIA allow us found waves of 24 and 48 seconds in EUV and UV images respectively, with a good spatial resolution. Besides, in the low atmosphere and corona the waves are of transient nature and finite lifetime, then in the most of cases we found oscillations of few periods. These waves also have a pronounced temporal modulation in parameters as period and amplitude. Theses characteristics, turn the wavelet analysis a well suited method for analysing temporal series and to study waves in the solar atmosphere (MOORTEL et al., 2004).

In this work we used the PWF method (SYCH; NAKARIAKOV, 2008) to determine the presence of waves in a 3D data cube, making spectral static and dynamics 2D maps.

4.1 Wavelet Analysis Evolution

Before the wavelet transform becomes a popular tool for the analysis of data sets, were introduced methods as the Fourier transform and windowed Fourier transform (WENG; LAU, 1994). As follow, we will explain the principal characteristics of each one.

Fourier transform is an useful tool to obtain global information of wave-like signals. However, it does not get local information at certain instant of time. The signals are averaged over a whole domain, hence, it is not appropriated to analyse non-stationary signals that occurred only in a short period of time (WENG; LAU, 1994; MOORTEL et al., 2004). On the other hand, the windowed Fourier transform extracts local-frequency information of a signal using time-frequency window (TORRENCE; COMPO, 1998). As this is fixed width, it is not possible to detect simultaneously high and low frequencies at the same signal (WENG; LAU, 1994).

Wavelet transform is a suited tool to analyse non-stationary signal observed in short periods of time (MOORTEL et al., 2004). It is a mathematical technique, based on group theory and square integrable representations, used to unfold a signal into both space and scale (FARGE, 1992). Wavelet transform divides a data set into components with different scales, then each component is studied with a resolution

matched to its scale. In addition, wavelet transform uses a flexible time-frequency window that adjust its width automatically when fixing on high (narrow) or low (wide) frequencies oscillations (WENG; LAU, 1994; TORRENCE; COMPO, 1998).

For a time series, x_n with equal time spacing δt and $n = 0 \dots N - 1$, the wavelet function $\psi(\eta)$, with η as non-dimensional time parameter, satisfies the following conditions (FARGE, 1992; WENG; LAU, 1994):

- Admissibility condition: It is a squared integrable function with average equal to zero.
- Regularity condition: It is well localized in both time and frequency spaces.
- It has finite energy, i.e., it should be normalized.
- Cancellations condition: To study the behaviour of the Nth derivative of function, the wavelet should cancel terms up to order N, i.e., vanishing high order moments to not alter the lower-order variations.
- Invertibility condition: The function's shape should be able to recover the signal exactly from its wavelet coefficients (i.e., to be one reconstruction formula) and for allowing to calculate other quantities from them.
- Similarity condition: The scale decomposition should be obtained by the translation ($\psi(\eta) \rightarrow \psi(\eta + 1)$) and dilation ($\psi(\eta) \rightarrow \psi(2\eta)$) of only one *mother function*. Dilated and translated functions that have its origins in a mother function are called *daughter wavelets* or *wavelet*. Sometimes, the mother function is know as *analysing wavelet* or *basic wavelet*.

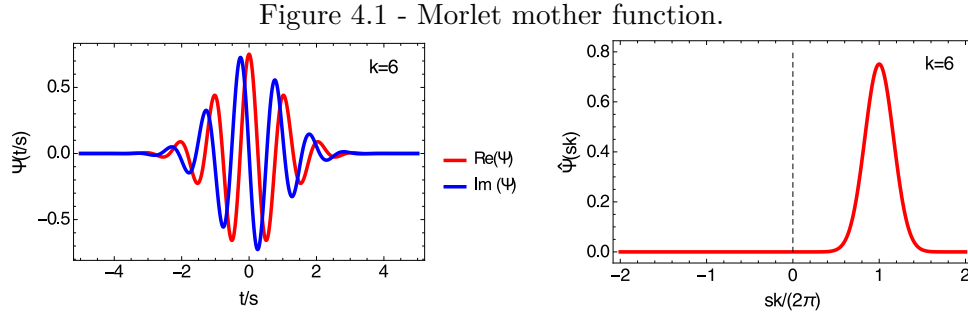
The most common mother functions are Morlet, Paul and Derivative of Gaussian (DOG) (TORRENCE; COMPO, 1998; MOORTEL et al., 2004).

The Morlet wavelet is complex-valued characterized by having large number of oscillations and hence a good frequency resolution.

$$\psi(\eta) = \pi^{-1/4} e^{ik\eta} e^{-(\eta^2/2)}, \quad (4.1)$$

where k is a non-dimensional frequency that controls the number of oscillations present in the mother wavelet, i.e., determine the frequency and time resolution of

the corresponding wavelet transform. In Figure 4.1 is presented the real and complex part of function Morlet in both time and frequency domains.

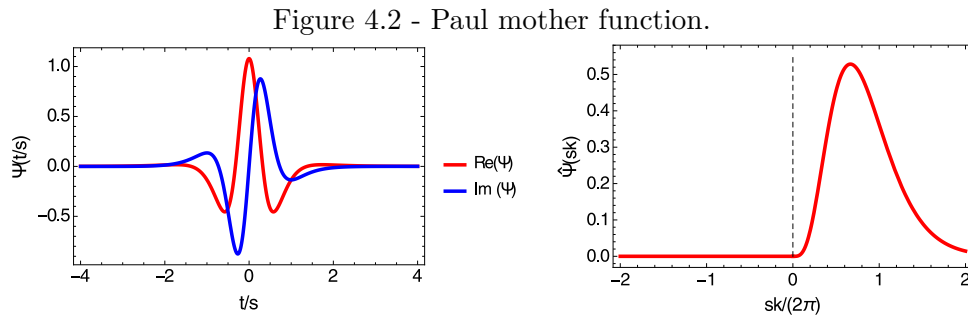


Representation of Morlet mother function (Equation (4.1)) for $k = 6$. **Left:** Real (red line) and complex (blue line) part of wavelet function in time domain. **Right:** Wavelet function in frequencies domain for $k = 6$ and $s = 1$.

SOURCE: Reproduction from Torrence and Compo (1998)

Figure 4.2 shows the Paul wavelet. This mother function is also complex-value. It has fewer oscillations, but is very localised in time, which means that the resolution in time is larger but in frequency is lower.

$$\psi(\eta) = \frac{2^m i^m m!}{\sqrt{\pi(2m)!}} (1 - i\eta)^{-(m+1)}, \quad m = \text{order} \quad (4.2)$$



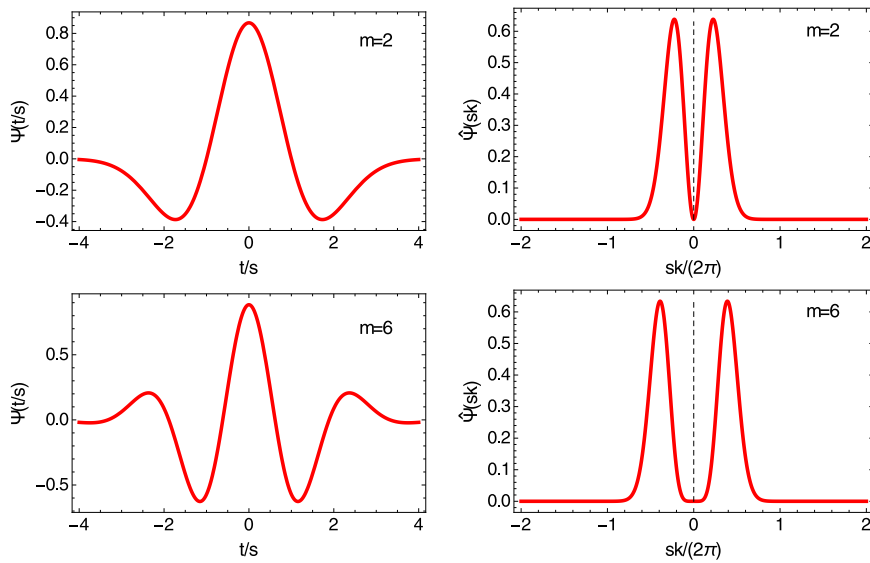
Representation of Paul mother function for $m = 4$ (Equation (4.2)). **Left:** Real (red line) and complex (blue line) part of wavelet function in time domain. **Right:** Wavelet function in frequencies domain.

SOURCE: Reproduction from Torrence and Compo (1998)

DOG function is real-valued. It has few oscillations in a much wider time domain. To $k = 2$ DOG is called Mexican hat wavelet. In Figure 4.3 we show the DOG function for $m = 2$ and $m = 6$

$$\psi(\eta) = \frac{(-1)^{m+1}}{\sqrt{\Gamma(m + \frac{1}{2})}} \frac{d^m}{d\eta^m} \left(e^{-\eta^2/2} \right), \quad m=\text{derivative} \quad (4.3)$$

Figure 4.3 - Derivative of Gaussian (DOG) mother function.



Representation of Equation (4.3) DOG mother function. **Left top:** Real part of wavelet function in time domain for Mexican hat (DOG $m = 2$). **Right top:** Wavelet function in frequencies domain for (DOG $m = 2$). **Left lower:** Real part of wavelet function in time domain for DOG $m = 6$. **Right top:** Wavelet function in frequencies domain for DOG $m = 6$

SOURCE: Reproduction from Torrence and Compo (1998)

A wavelet function may be orthogonal or non-orthogonal, but a wavelet basis refers only an orthogonal functions. This can be used with the discrete wavelet transforms, while the non-orthogonal functions may be used with the discrete or continuous wavelet transform (FARGE, 1992; TORRENCE; COMPO, 1998). We will use the continuous wavelet transform and hence we will not describe the orthogonal neither discrete wavelets.

For a discrete time series x_n the continuous wavelet transform is defined as the

convolution of x_n with a scaled and translated version of $\psi(\eta)$ i.e .

$$W_n(s) = \sum_{n'=0}^{N-1} x_{n'} \sqrt{\frac{\delta}{s}} \psi^* \left[\frac{(n' - n)\delta t}{s} \right], \quad (4.4)$$

where s is a wavelet scale, $\eta = (n' - n)/s$ is a time variation, and ψ^* is the complex conjugate of ψ (TORRENCE; COMPO, 1998; MOORTELE et al., 2004).

The wavelet transform has been widely used in solar physics to study oscillatory phenomena. For example, Moortel et al. (2000a) studied the damping of a signal using the wavelet power and applied this technique to the phase mixed Alfvén waves. Moortel et al. (2002) and Moortel et al. (2004) also used this technique to study the properties of observed wave-like oscillations and damping of waves in coronal loops. On the other hand, Moortel and McAteer (2004) developed an automatic technique for identifying periodicities in time series, through wavelet spectrum. Ireland et al. (1999) analyse active regions oscillations and detect their duration and period, through the wavelet transform over observations from SoHO and CDS–Normal Incidence Spectrometer (NIS).

4.2 Pixelised Wavelet Filtering (PWF)

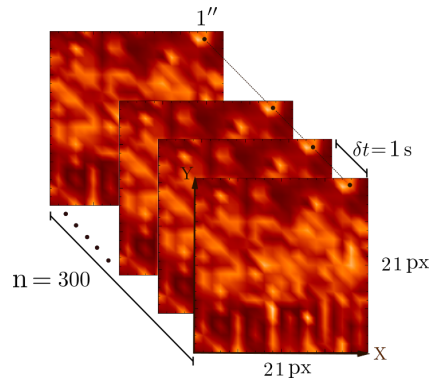
One method based in wavelet analysis is called pixelised wavelet filtering (PWF) (SYCH; NAKARIAKOV, 2008; SYCH et al., 2010), which has been applied to find waves in sunspots with data obtained from SDO (SYCH; NAKARIAKOV, 2014; YUAN et al., 2014), TRACE and NoRH (SYCH et al., 2012). This allows us to identify periodicities in 3D data cubes, showing the spatial distribution and temporal evolution of frequencies found, through of 2D narrowband maps.

The method applies the continuous wavelet transform, using the Morlet mother function over the time signal of each pixel within the region of interest (ROI) selected. The continuous wavelet transform is calculated with the code provided by Torrence and Compo (1998) ¹.

We will explain the PWF method steps using a synthetic data cube that contains standing and travelling waves of different periods, wavelengths, and amplitudes. This was reproduced from Sych and Nakariakov (2008). Figure 4.4 shows the simulated data cube of 300 frames with 21×21 pixels and temporal cadence of one second.

¹The software is available at <http://paos.colorado.edu/research/wavelets/>

Figure 4.4 - Synthetic data cube



The data cube was made with 300 frames of 21×21 pixels temporally spaced by 1 second.

SOURCE: Reproduced from Sych and Nakariakov (2008)

A 3D data cube (x, y, t) is a set of images obtained with a equal cadence δt ; x and y represents the axis of images and t the time. Therefore, each pixel is associated with a time series x_n which describes the temporal variation of its intensity.

To select the ROI it is made a variance map, calculating the variance over the time series of each pixel. Thus, the map shows the spatial distribution of the time variations including all spectral frequencies. However, we can select the ROI without the variance map. In Figure 4.5 is presented a snapshot of synthetic data cube and its variance map which includes the 20, 60, and 100 seconds periods and noise.

Figure 4.5 - Test signal and Variance map

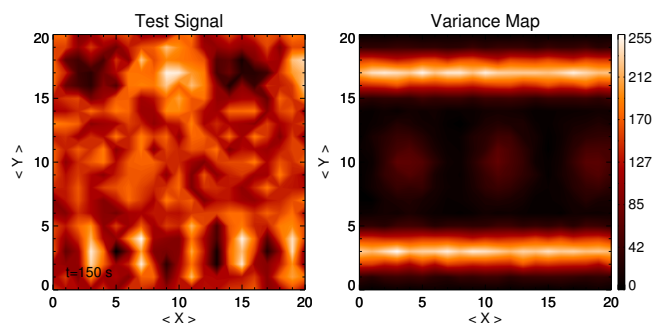
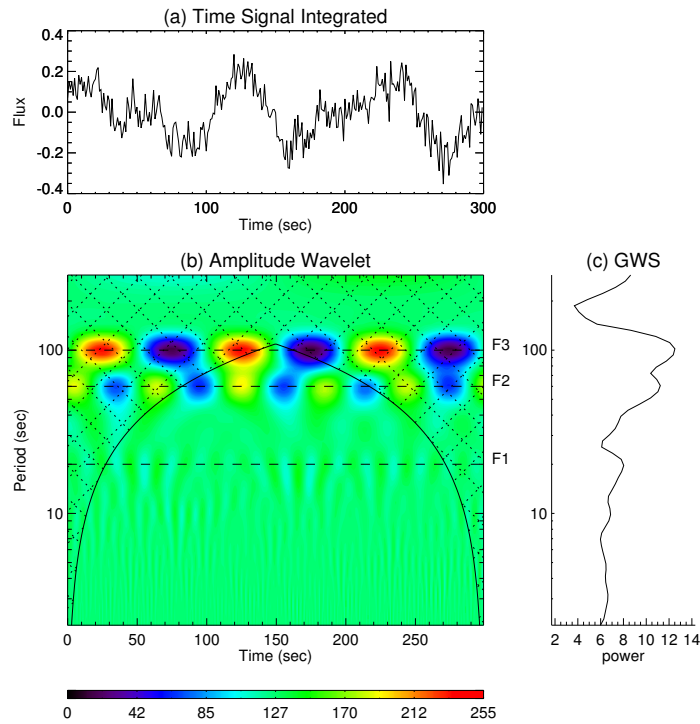


Image of test signal and variance map for synthetic data cube.

SOURCE: Reproduced from Sych and Nakariakov (2008)

In the next step we calculate the wavelet transform of the time signal integrated over the whole ROI (see Figure 4.6(a)). Through the amplitude wavelet spectrum, we identify the significant periodicities present in the signal. The cone of influence (COI) is the region where the errors at the edges of the wavelet transform may be important and values inside this area should be treated with caution (MOORTELE; MCATEER, 2004). In Figure 4.6(b) the COI is represented by the hatched area. Period F3 is inside of this area, but we considered it in the significant periodicities group. In Figure 4.6(b) and (c) are presented the significant periods F1, F2, and F3 indicating 20, 60 and 100 seconds, respectively. The dashed lines indicate the periods found and the peaks present in the global wavelet spectrum (GWS) indicate the presence of these oscillations.

Figure 4.6 - Temporal signal and wavelet spectra for synthetic data cube.



(a) Temporal signal integrated over ROI. (b) Amplitude wavelet spectrum. (c) Global wavelet spectrum.

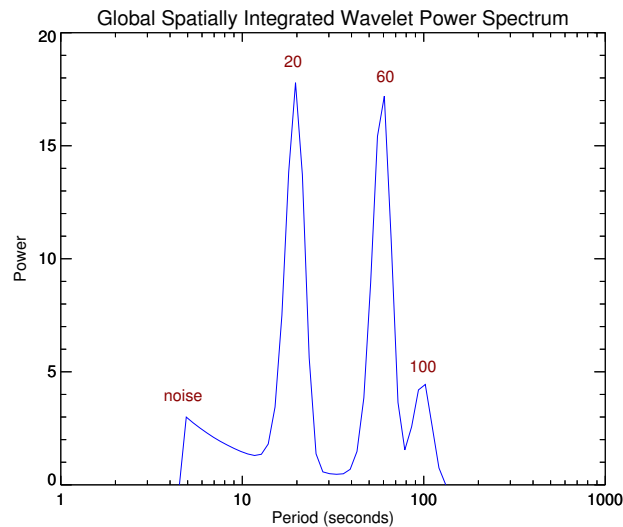
SOURCE: Torrence and Compo (1998), Sych and Nakariakov (2008)

In the same manner, we applied the wavelet transform in the time series of each pixel of ROI, obtaining a 4D data cube (x, y, t, P) , with P representing the period. Next, we filtered by period-bands previously chosen and calculate the inverse transform over this 4D cube. Thus we made a band pass filter to obtain a time signal for a specific period-band. Next, we find the power for each curve and made a broadband power cube which is used for visualising the spatial distribution of the spectrum of the oscillation sources.

The spatial distribution of the power corresponding to each period-band is called narrowband power map. Then, integrating this narrowband temporal signal over the spatial domain of each period-band, we obtain the global spatially integrated wavelet power spectrum (GSIWPS). The spectrum peaks show the oscillations found in the ROI.

The peaks shown in Figure 4.7 represent the periods found in the 3D data cube. There are three peaks indicating the presence of 20, 60, and 100 second oscillations. Also is present the signal noise in the spectrum. Figure 4.8 shows the temporal signal by each filtered period-band.

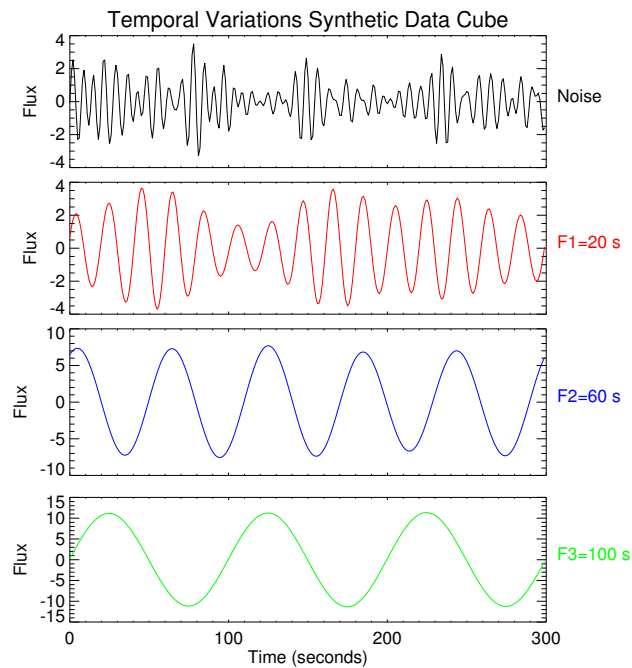
Figure 4.7 - Global Synthetic Integrated Wavelet Power Spectrum



The three peaks on the GSIWPS indicate that were found oscillations of 20, 60, and 100 seconds. Also the noise is showed in the spectrum .

SOURCE: Reproduction from [Sych and Nakariakov \(2008\)](#)

Figure 4.8 - Temporal signal filtered.

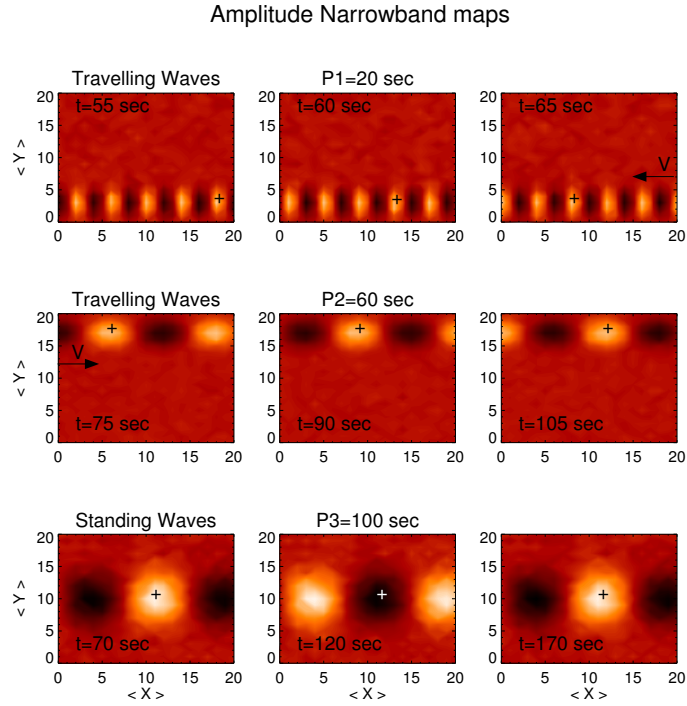


Temporal signal filtered by period-bands for oscillations present in the synthetic data cube. Filtered signal for noise and periods of 20, 60, and 100 seconds are presented.

SOURCE: Author production.

To establish what type of wave was found and to study the temporal evolution of these waves we made videos with the narrowband maps for each period-band. They are called dynamical map. In this example were found travelling waves of 20 and 60 seconds and standing waves of 100 seconds. In Figure 4.9 are showed travelling waves of 20 and 60 seconds in three instants of time (top and middle). In the same manner, standing waves of 100 seconds are presented in the data cube (bottom).

Figure 4.9 - Dynamical Maps.



Dynamical map for waves found in the synthetic 3D data cube. **Top:** Travelling waves of 20 seconds. **Middle:** Travelling waves of 60 seconds. **Bottom:** Standing waves of 100 seconds.

SOURCE: Reproduced from [Sych and Nakariakov \(2008\)](#)

In this work, we made the 3D data cubes taking a number of frames corresponding to sixty and thirty minutes of observation. For one hour, we made six principal and five secondary cubes overlapped by thirty minutes. Similarly, for thirty minutes we made twelve principal and eleven secondary cubes overlapped by fifteen minutes. All data cubes have the same dimensions ($122.4'' \times 146.4''$) and we chose the ROI before calculate the variance map.

We wrote a set of routines in IDL to calculate step by step the PWF in each 3D data cube according to [Sych et al. \(2010\)](#). At the end, we got the plots of variance map, wavelet transform power and amplitude spectra, GSIWPS indicating the oscillations present in the ROI, and a narrowband map for oscillations found in automatic

form. The set of routines were written considering the follow steps. The continuous wavelet transform, was calculated with Morlet mother function using the [Torrence and Compo \(1998\)](#) routines. We select the period-bands between $dt \times 2^{n-1}$ and $dt \times 2^n$, where dt is the temporal cadence in seconds and $1 \leq n \leq 6$. These period-bands were chose following to [Sych et al. \(2010\)](#). Thus, in the next step we calculated the wavelet transform pixel by pixel, filtering by the period-bands selected. Then, with the GSIWPS, we identified the frequencies present in the data cube, and with the broadband, narrowband maps we studied the spatial distribution of signal power.

One complete data cube is too large to calculate the PWF and need a lot of time and random access memory (RAM). So, to optimize the calculation time and RAM usage we divided these ROI cubes in parts (two, four, and six) depending on the number of frames contained in the data cube, e.g. for a cube of 171 Å with 300 frames, we divided it in six parts. The code divide the data cube with our specifications and put together the filtered results in just a few minutes.

5 3D MODEL OF WAVES ALONG OF CORONAL LOOPS

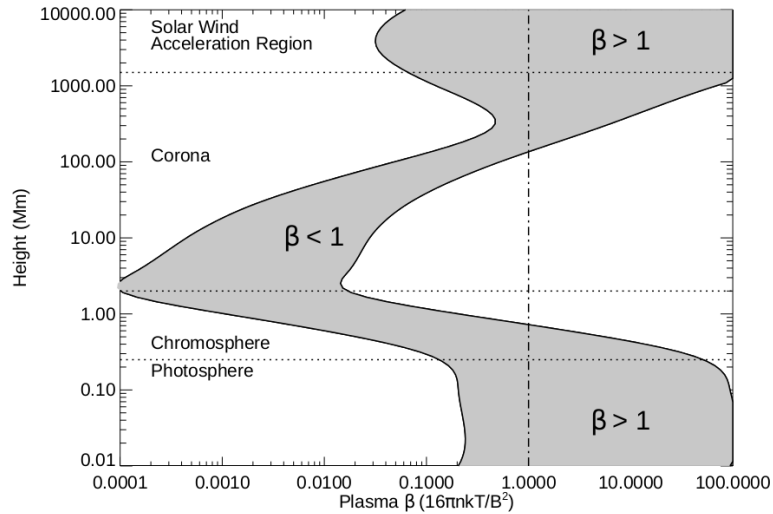
5.1 Linear Force-Free Field (LFFF) Approximation

The dynamics of most part of the solar atmosphere is dominated by the magnetic fields. This can be seen through the plasma- β parameter, which is defined as the ratio of the thermal plasma P_{th} to the magnetic P_B pressures.

$$\beta = \frac{P_{th}}{P_B} = \frac{2\xi n_e k_B T_e}{B^2/8\pi}, \quad (5.1)$$

where ξ is the ionization correction of pressure, $\xi = 1$ and $\xi = 0.5$ for the corona and photosphere respectively, B (G) the magnetic field strength, and T_e (K) the electron temperature (ASCHWANDEN, 2004). Figure 5.1 shows that between the photosphere and upper corona the magnetic pressure is dominant over the plasma pressure.

Figure 5.1 - Plasma β parameter in the solar atmosphere.



The plasma β determines the relation between the thermal gas P_{th} and magnetic P_m pressures.

SOURCE: Gary (2001)

For $\beta \ll 1$, if in the lowest order all non-magnetic forces, e.g., gravity and kinematic plasma flow pressure, are neglected and the Lorentz force is vanished, we can use the force-free field approximation (WIEGELMANN; SAKURAI, 2012).

For static configuration it is defined as:

$$\mathbf{j} \times \mathbf{B} = \mathbf{0}, \quad (5.2)$$

$$\mathbf{j} = \nabla \times \mathbf{B} / \mu_0, \quad (5.3)$$

where the relation (5.3) is the electric current density. This approximation also includes the Gauss' law (Equation (2.8)).

Inserting Equation (5.3) into (5.2) we have:

$$(\nabla \times \mathbf{B}) \times \mathbf{B} = \mathbf{0}, \quad (5.4)$$

which is satisfied by one of the following two cases ([WIEGELMANN; SAKURAI, 2012](#)):

- *Current-free or potential magnetic fields*: It is the simplest assumption for the coronal magnetic field. This is expressed by

$$\nabla \times \mathbf{B} = \mathbf{0}. \quad (5.5)$$

The magnetic field is measured from the Zeeman effect in the photosphere through of LOS magnetograms ([BECKERS, 1971](#)). This is used as boundary conditions to solve the Laplace equation for the scalar potential ϕ ,

$$\Delta \phi = 0. \quad (5.6)$$

The Laplacian operator Δ is the divergence of the gradient of the scalar field. The magnetic field is expressed as

$$\mathbf{B} = -\nabla \phi. \quad (5.7)$$

- *Force-free fields*

$$\mathbf{B} \parallel \nabla \times \mathbf{B} \quad (5.8)$$

This condition can be written as

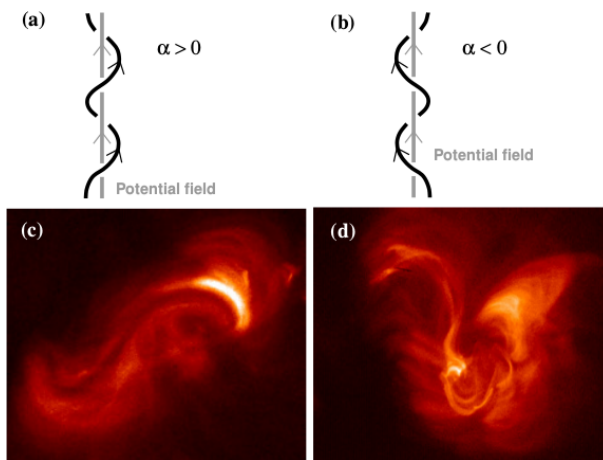
$$\nabla \times \mathbf{B} = \alpha \mathbf{B}, \quad (5.9)$$

$$\mathbf{B} \cdot \nabla \alpha = 0, \quad (5.10)$$

where $\alpha(\mathbf{r})$ is the force-free function.

The function $\alpha(\mathbf{r})$ depends only on the local geometry of field lines, not on the field strength. Considering the Gauss' Law α should be constant along magnetic field lines (MACKAY; YEATES, 2012), always. When α is constant also throughout different field lines, the solution of Equation (5.9) is the linear force-free set (LFFF) and when it is not, we get the non-linear force-free field set (NLFFF). For global solutions using the LFFF approach, the α values should be closer to potential and can be used for small regions not for the total solar disk (SEEHAFFER, 1978).

Figure 5.2 - Twist for force-free magnetic field



Direction of twist for a field line with $\alpha > 0$ **(a)** and $\alpha < 0$ **(b)** with respect to potential field $\alpha = 0$. Panels **(c)** and **(d)** correspond to the image of sigmoid structures for each α showed in **(a)** and **(b)** respectively. These images were taken with Hinode X-ray Telescope on 2007 February 16 and 2007 February 5, respectively.

SOURCE: Mackay and Yeates (2012)

The function $\alpha(\mathbf{r})$ also quantifies the magnetic “twist” (see Figure 5.2(a)–(b)). The potential field $\mathbf{j} = \mathbf{0}$ is recovered if $\alpha = 0$ in all places. On the other hand, if α is constant everywhere, then the curl of (5.9) leads to the vector Helmholtz equation

$$(\nabla^2 + \alpha^2)\mathbf{B} = 0, \quad (5.11)$$

which is linear and may be solved analytically in spherical harmonics (DURRANT, 1989).

5.2 Three Dimensional Reconstruction of the Magnetic Field Line

Images from SDO/AIA allow us to study the dynamics of structures (e.g., coronal loops) involved in transient events. We can observe well defined coronal loops in 171, 193, and 211 Å band passes. However, as the coronal loops structure is guided by the magnetic field, to obtain the magnetic field lines allow us to study the loops dynamic with more accuracy.

Extrapolating the magnetic field at photospheric level, using LOS magnetogram and numerical codes, we can know its value in the chromosphere and corona (NAKAGAWA; RAADU, 1972; AMARI et al., 1997; AMARI et al., 1999). Considering a force-free field, some methods have been made in attempt to reconstruct the coronal magnetic field from photosphere. For example, Nakagawa et al. (1971) and Sheeley Jr. and Harvey (1975) studied the magnetic configuration of sunspots and flux tubes at the solar surface. Also, Barnes and Sturrock (1972) and Low and Nakagawa (1975) studied the characteristics of magnetic field in coronal structures, considering different states of force-free field.

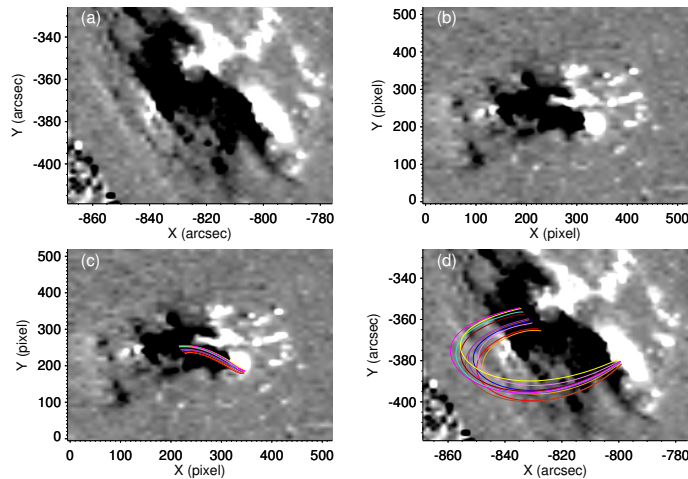
In this work, we used the method proposed by Nakagawa and Raadu (1972) where it is assumed that in the chromosphere and lower corona the quasi-static magnetic field must be nearly force-free (LFFF approximation). Besides, we also considered the conditions to determine the α value according the boundary value problem discussed by Seehafer (1978).

We used codes written in IDL to find the magnetic field lines. It is necessary a regular grid formed by plane surfaces, which is possible considering small regions in the solar disk. The codes obtain the magnetic field value since the vertical component B_z of LOS magnetogram, give us a resultant cube with the \mathbf{B} components value (B_x, B_y, B_z) and with this, we obtain the field lines coordinates (x, y, z) .

We choose a ROI with 512×512 pixels, which give us a 3D cube of $512 \times 512 \times 512$ pixels³. The process to obtain the field lines in this cube consume a lot of time and RAM memory. Then, we established some criteria in order to diminish the calculation time and optimize the use of the RAM memory. These criteria concerns on the lines maximum height and the selection of the region where we hope to find the field lines.

It is important to note that for regions closer to solar limb the Sun's geometry plays an important role and it is possible to obtain false values of α or not find the lines that match with the loops seen in EUV. In our analysis, we considered an active region near to the solar limb (S19E53). Then, we rotated this region to the Sun's centre and re-sampled it to obtain a regular grid, taking into account the spherical shape of the Sun. Next, we extrapolated and rotated back the field lines. Figure 5.3 shows the steps to extrapolate field lines in the solar limb for loops **G**. Panel (a) shows the ROI's HMI magnetogram. Panel (b) shows the same ROI moved to centre of solar disk and re-sampled. Over this were extrapolated the field lines which are shown in panel (c). We used a transformation matrix, generated when the ROI was rotated, to move the field lines to the solar limb as is shown in panel (d).

Figure 5.3 - Extrapolation of magnetic field in the solar limb



Process to extrapolate field lines in the solar limb for loops **G** of NOAA 11272. (a) ROI in the solar limb. (b) ROI moved to the solar disk centre and re-sampled. (c) Extrapolated lines in the solar disk centre. (d) The same lines seen in (c) but moved to the solar limb.

SOURCE: Author production

5.3 3D Model of Velocity Waves

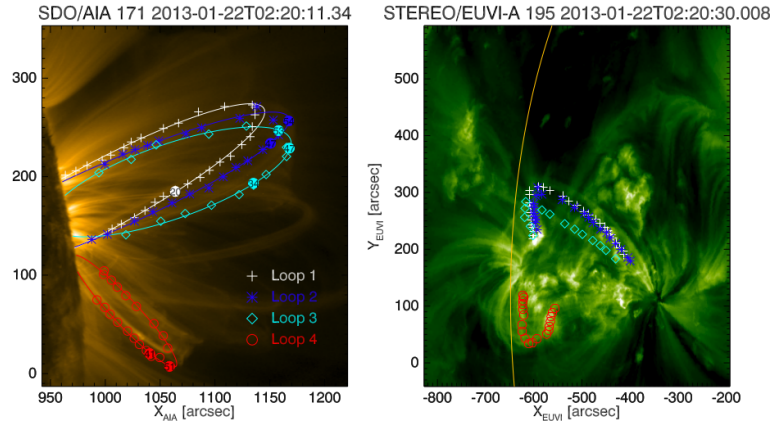
Most of works about waves in coronal loops have been done in 2D (ASCHWANDEN et al., 2002; MOORTEL et al., 2002; WANG et al., 2003a), because one of the problems is to reconstruct the loop in 3D.

The knowledge of the loop coordinates (x, y, z) allows us to do more accuracy analysis, about the characteristic of plasma along them. Thus, techniques to obtain the 3D magnetic field topology of coronal loops have been used (ASCHWANDEN et al., 1999; WHITE; VERWICHTE, 2012; ASCHWANDEN, 2016), some of them using magnetic extrapolation and others through of automatic detection from EUV images.

Aschwanden et al. (2008) and Aschwanden et al. (2009), used the stereoscopy-based tomography method to detect loops in EUV and represent them in 3D. In the same manner, Aschwanden (2005) and Rosa et al. (2009) obtained the geometry of loops observed in EUV through NLFFF extrapolations. Another alternative is proposed in the Vertical Current Approximation (VCA)-NLFFF code, developed by Aschwanden (2016) to reconstruct coronal loops for far regions of solar limb.

On the other hand, STEREO is a NASA mission and has two nearly identical space observatories (one ahead of Earth in its orbit, the other trailing behind) (EYLES et al., 2009; HOWARD et al., 2008). We can know the geometrical shape of loops in 3D space joining images from both STEREO and SDO/AIA (NISTICÒ et al., 2013b) and making a coordinate transformation. This has been used for studying loops in active regions located near to the solar limb (ANFINOGENTOV et al., 2013). However, due to the movement of STEREO observatories, images on the solar limb are not available all time. Then, this method can be used only in limited cases. Figure 5.4 shows the geometry of four loops observed from SDO and STEREO. Length of these loops was used to measure the period and amplitude of kink oscillations to determine the evolution phase along the oscillating loops (ANFINOGENTOV et al., 2013).

Figure 5.4 - Loops reproduced using SDO and STEREO images



Images of coronal loops reproduced using SDO and STEREO data. **Left:** Loops seen by SDO/AIA. **Right:** Loops seen by STEREO

SOURCE: Anfinogentov et al. (2013)

We made a three-dimensional model for describing the waves behaviour along the loops. This model was constructed over extrapolated field lines that reproduce the coronal loops seen in EUV.

We calculated the sound velocity for each line point, using the Equation (2.13) and temperature values from structure semi-empirical models. We used the Machado et al. (1980) model for chromospheric flare regions to heights between photosphere and low chromosphere. For greater heights, we used the SSW routines for automated detection of temperature developed by Aschwanden et al. (2013).¹

According to SDO/AIA thermal response and to flare-like temperatures determined by O'Dwyer et al. (2010), we calculated the sound velocity expected for each band pass of AIA, which are listed in Table 5.1.

¹Software available at <http://www.lmsal.com/~aschwand/software>

Table 5.1 - Sound velocities expected for SDO/AIA EUV lines, according to O'Dwyer et al. (2010) model.

Wavelength (Å)	T (MK)	c_s (km s ⁻¹)
131	11.22	492.39
171	0.70	122.98
193	17.78	619.84
211	1.99	207.36
335	2.81	246.41
94	7.07	390.86

SOURCE: Conde et al. (2016)

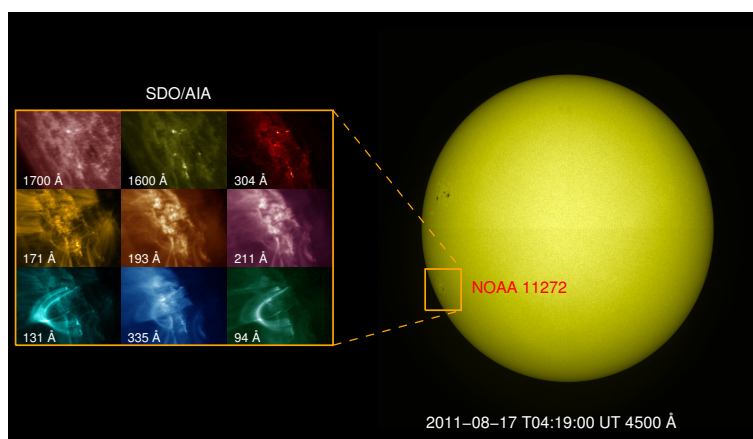
For Alfvén velocity, we used the magnetic field value corresponding to each line point and hydrogen number density n_h (cm⁻³) values from structure semi-empirical models. As we did for temperature, we used the Machado et al. (1980) model for heights below the chromosphere. For heights corresponding to chromosphere and transition region, we used the C7 model by Avrett and Loeser (2008). These values were used in the Equation (2.25) for determining v_A . We present the resulting velocities through three-dimensional graphics of the loops over the magnetogram located in the Sun's centre.

6 NOAA 11272

6.1 Active Region Characteristic

Active Region NOAA 11272, localised at S19E53 was analysed between 16 August 2011 at 23:45:00 UT and 17 August 2011 at 05:40:00 UT. For this study we used high-resolution UV (1600 and 1700 Å) and EUV (304, 131, 171, 193, 211, 335, and 94 Å) images taken by SDO/AIA, with temporal cadence of 24 and 12 seconds, respectively. We did not use images in 4500 Å, because the temporal cadence is 3600 seconds. The images were aligned and processed using the SSW routines as we explained in Chapter 3. Figure 6.1 (left-hand) shows the active region in nine SDO/AIA wavelengths on 2011-08-17 at 04:19:00 UT. Orange box on the full disk (right-hand) encloses the ROI selected for the wavelet analysis.

Figure 6.1 - Active Region NOAA 11272 seen in nine SDO/AIA wavelengths



At right-hand, an image of the Sun's surface in white light continuum. Orange box indicates the place of NOAA 11272. Active region seen in 1700, 1600, 304, 171, 193, 211, 131, 335 and 94 Å is shown at left-hand.

SOURCE: Author production

On 17 August 2011 GOES-15 spacecraft detected the B3.8, C1.9, and C2.3 class flares as is shown in Table 6.1. B3.8 class flare was located in NOAA 11271, however we compared the temporal signals for NOAAs 11271 and 11272 around 23:50:00 UT and observed that this flare occurred in NOAA 11272. Figure 6.2 shows the signal integrated for both active regions in 131 Å. We plotted this band pass because it was more sensible for detecting the B3.8 flare. The black line in Figure 6.2 is coherent

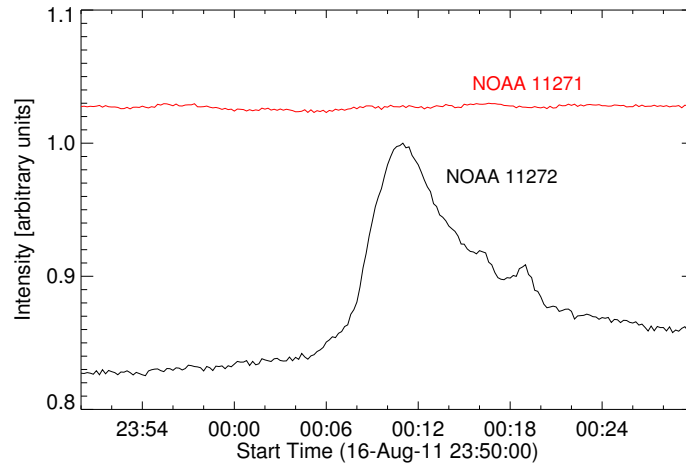
with the period in which this flare occurred and hence we included it in our analysis.

Table 6.1 - Flares occurred in NOAA 11272 on 17 August 2011.

Flare Class	Begin UT	Maximum UT	End UT
B3.8	00:06	00:11	00:20
C1.9	01:44	02:54	03:44
C2.3	04:19	04:29	05:07

SOURCE: Author production

Figure 6.2 - Time profile of signal for NOAAs 11271 and 11272 in 131 Å.



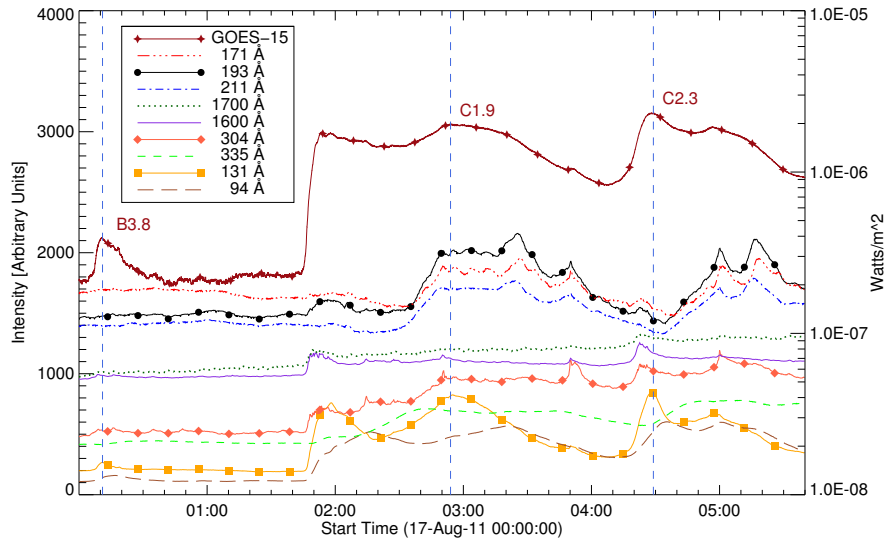
Time profile comparison between NOAA 11271 (red line) and 11272 (black line) during the corresponding time for B3.8 class flare.

SOURCE: Author production

Figure 6.3 shows the GOES-15 light curve for NOAA 11272. We indicate the maximum time of each flare with vertical dashed lines. In the same manner, we show the temporal signal integrated (in arbitrary units) of the AIA images in nine band passes. For 193 and 211 Å, the intensity was re-scaled subtracting 1150 and 150 arbitrary units, respectively. For 131, 304 and 1700 Å we used factors of 3, 6 and 5 and subtracted 150, 400 and 1200 arbitrary units, respectively. In 1600 Å we did it

with a factor of 5.5 and added 190 arbitrary units. Finally, 94 Å signal was re-scaled by a factor of 4. The GOES light curve and the temporal signals coincide in the maximum time of each flare. This is more evident in 131 Å.

Figure 6.3 - Time profile of intensity for NOAA 11272.

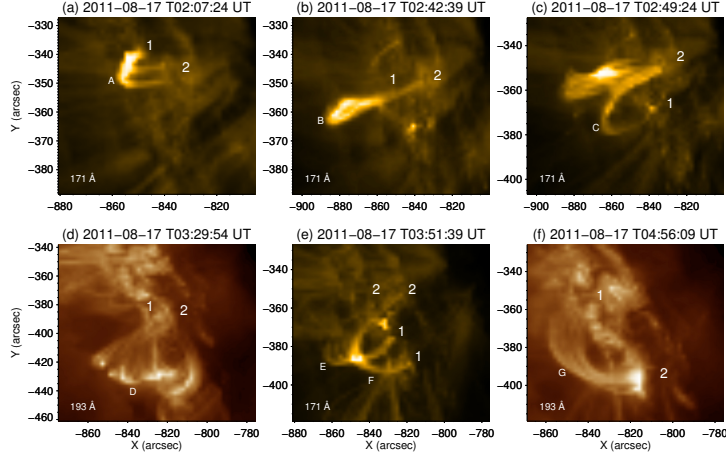


The time profile from nine AIA band passes is compared with the GOES light curve in 1–8 Å. The B3.8, C1.9, and C2.3 flares maximum time are indicated by vertical dashed line.

SOURCE: Author production

In Figure 6.4 we show seven loops related with each flare described in Table 6.1. These loops were seen in six EUV band passes of AIA images. According to this we chose the ROI with dimensions of $122.4'' \times 146.4''$ for the active region's oscillatory analysis. Numbers **1** and **2** indicate the footpoint positions for the active region loops. We designed these positions according the result of the magnetic field extrapolation, **1** and **2** refers to first and last line point, respectively. This, will be better explained in Section 6.4. Times in which appeared the loops are described in Table 6.2.

Figure 6.4 - Loops perturbed during the period of flares occurred in NOAA 11272.



Loops **A**, **B**, and **C** were perturbed during C1.9 flare (see panel (a), (b), and (c), respectively). Next, the loops **D**, **E** and **F** were perturbed (panel (d) and (e)). Finally, loop **G** was disturbed as is shown in panel (f). **1** and **2** refers to the footpoints of the loops.

SOURCE: Author production

Table 6.2 - Description of perturbed loops during the period of flares.

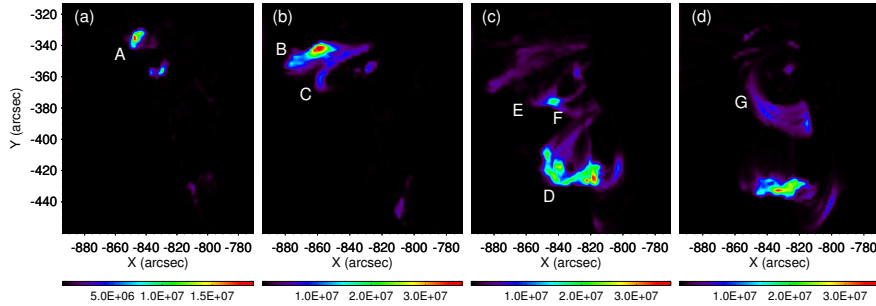
Flare	Band pass Å	Time	Loop
B3.8	131	00:06:09 UT – 00:30:09 UT	C
C1.9	171, 193	02:03:09 UT – 02:22:21 UT	A
C1.9	171, 193	02:35:57 UT – 03:39:45 UT	B
C1.9	171, 193	02:41:09 UT – 02:45:57 UT	footpoints B – C
C1.9	171, 193	02:41:09 UT – 03:16:09 UT	footpoint C
C1.9	171, 193	03:49:09 UT – 03:55:57 UT	footpoint C
C1.9	171, 193	02:49:33 UT – 03:34:09 UT	C
C1.9	131	01:44:09 UT – 02:30:45 UT	A, B, C
C1.9, C2.3	131, 171, 193	03:39:45 UT – 04:14:33 UT	E
C1.9, C2.3	131, 171, 193	03:48:45 UT – 04:15:09 UT	F
C1.9, C2.3	131	01:44:09 UT – 05:40:00 UT	G
C1.9, C2.3	171, 193	03:04:33 UT – 05:40:00 UT	G
C2.3	131	04:18:21 UT – 04:52:45 UT	D
C2.3	171, 193	04:45:33 UT – 05:33:21 UT	D

SOURCE: Author production

6.2 Waves Detected

We searched oscillatory presence along the loops **A–G** using the PWF method. In the first part, we obtained the variance maps to see the brightness spatial variation and the wavelet spectra for determining the significant periods. Figure 6.5 shows a variance map for 171 Å in different periods along the observation time. The variance map shows that there is high possibility of finding waves along the loops **A** (panel (a)), **B** and **C** (panel (b)), **D**, **E**, and **F** (panel (c)) and **G** (panel (d)).

Figure 6.5 - Variance map for loops perturbed during the flares occurred in NOAA 11272

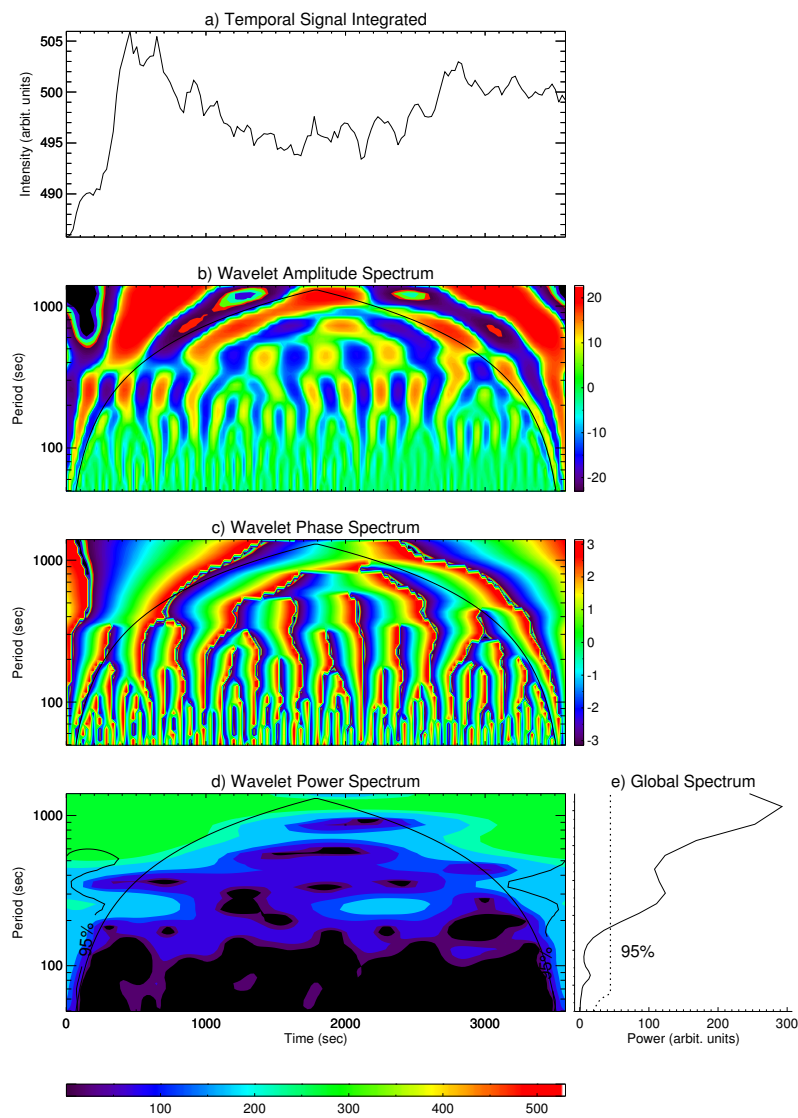


Variance map for images in 171 Å. The maps allow us to see the major spatial variation in each loop chosen for our analysis.

SOURCE: Author production

In Figure 6.6(b)–(d) we show the wavelet amplitude, phase, and power spectra of temporal signal integrated over the ROI (panel (a)), in 1700 Å band pass. In panel (b) it is possible to see the presence of oscillatory periods around 9, 5 and 2 minutes. In panel (d) the confidence level is seen outside of COI and the GWP (panel (e)) shows the 95 % of confidence level for periods of 19 and 9 minutes. Then, we selected the 19-, 9-, 5-, 2-, 1-, and 0.6-minute period-bands for filtering in the second part of PWF method (see Chapter 4).

Figure 6.6 - Wavelet spectra over temporal signal of 1700 Å .



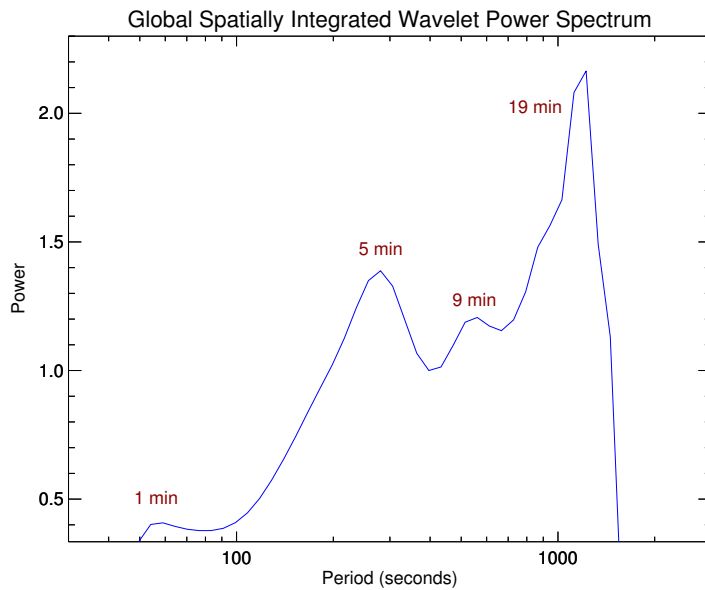
(a) Temporal signal integrated over the ROI, in arbitrary units. (b) wavelet amplitude spectrum indicating the periodicities included in the temporal signal. (c) Wavelet phase spectrum. (d) Wavelet power spectrum. (e) The global power spectrum shows the peaks of probably periodicities present in the signal. The 95 % of confidence level is shown in panels (d) and (e).

SOURCE: Author production

Hence, we obtained the global spatially integrated wavelet power spectra to identify the periodicities present in the data cube. Also, we can see the spatial distribution of these oscillations in the ROI through the narrowband maps.

Peaks in the GSIWPS showed the presence of 19-, 9-, 5-, 2-, 1-minute, and 36-second oscillations. The narrowband maps showed oscillations along all considered loops in EUV band passes and in the footpoints of the loops **A**, **B**, and **C**. For example, in Figure 6.7 we found 19-, 9-, 5- and 1-minute peaks in the spectrum for a data cube of 1600 Å, between 00:15:05 UT and 01:14:41 UT. In the same manner, Figures 6.8(a)–(e) show the first snapshot of narrowband map resulting of PWF for this data cube. Panel (f) represents a zoom for oscillations of 19 minutes seen in panel (e). Oscillations of 1, 2, 5, 9, and 19 minutes found in the data cube of 1600 Å are centred in the footpoint regions of the loops **A** and **C**. For determining if these oscillations are travelling or standing waves, we study the temporal evolution through the dynamical narrowband maps, *i.e.*, videos.

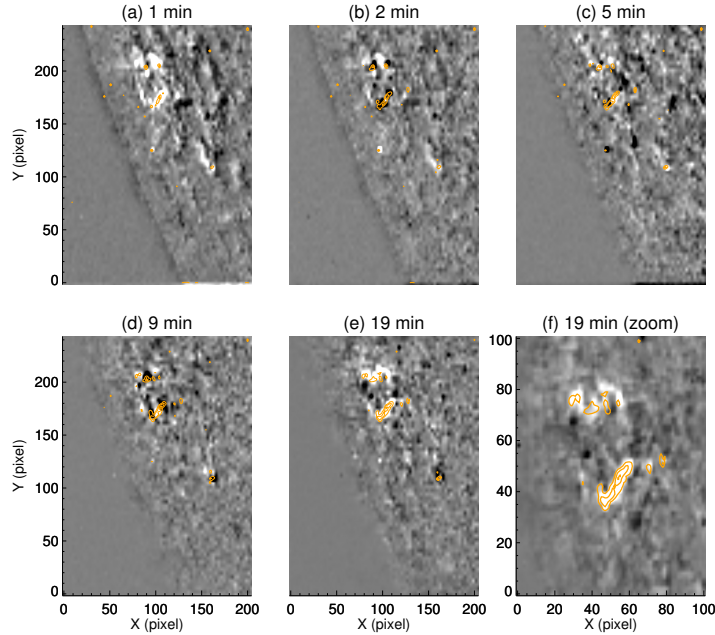
Figure 6.7 - Global spatially integrated wavelet power spectrum for 1600 Å.



The peaks show the presence of 19-, 9-, 5-, and 1-minute oscillations.

SOURCE: Author production

Figure 6.8 - narrowband map for 1600 \AA .



(a)-(e) The oscillation spatial variation is centered in the footpoint area of the loops **A** and **C**. In (f) is shown a zoom of the region where the oscillations of 19 minutes are centered.

SOURCE: Author production

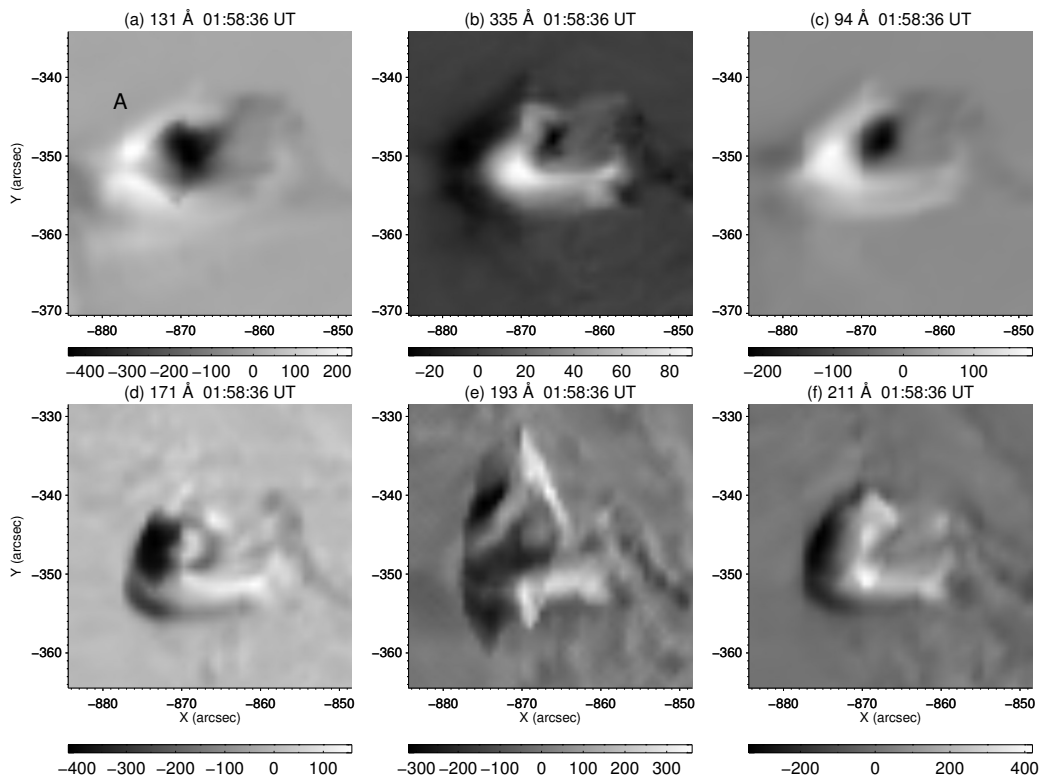
In the following, we will explain in more detail the waves found in the active region during the flares mentioned in Table 6.1.

19-minute standing waves

We found standing waves in the period-band of 19 minutes (19 ± 6 min) at the loops **A**, **B**, and **C** showed in Figures 6.4(a)–(c). These waves were observed during the C1.9 flare, from 01:15:00 UT to 03:44:48 UT, in six EUV band passes (171, 193, 211, 131, 335, and 94 \AA).

Figures 6.9(a)–(f) show snapshots of narrowband maps for the amplitude (in arbitrary units) of the waves seen at 01:58:36 UT. Comparing the maximum (bright details) and minimum (dark) amplitudes, we saw that detected waves in 131, 335, and 94 \AA (Figures 6.9(a)–(c)) and in 171, 193, and 211 \AA (Figures 6.9(d)–(f)) are in phase. However, the two groups are out of phase.

Figure 6.9 - Amplitude narrowband maps for waves of 19 minutes along the loop **A**.



Standing waves were seen in 131 Å (a), 335 Å (b), 94 Å (c), 171 Å (d), 193 Å (e) and 211 Å (f). The colorbar indicates the variation between the maxima and minima amplitudes.

SOURCE: Conde et al. (2016).

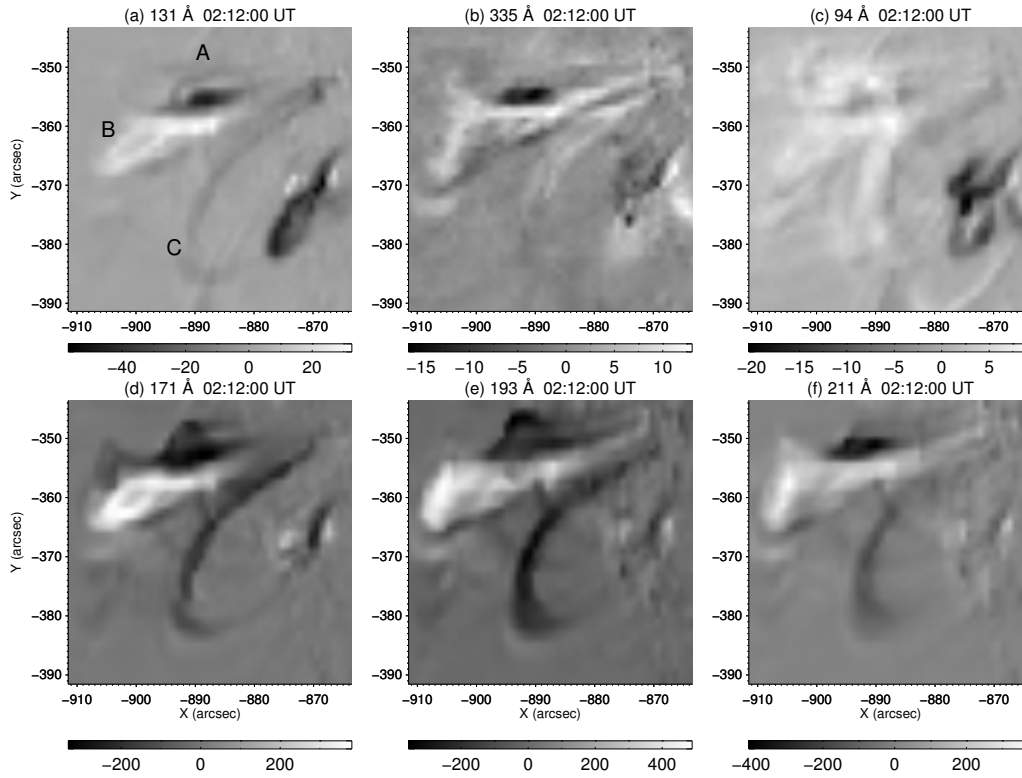
Loops **B** and **C** were perturbed after starting the C1.9 flare (Figure 6.10), from 01:45:00 UT to 02:44:48 UT, being clearly visible in 171, 193, and 211 Å lines (Figures 6.10(d)–(f)). In particular, the loop **C** is highlighted in the snapshots of 171, 193 and 211 Å. The variation between maximum and minimum amplitudes seen in the narrowband maps, shows waves in phase for loops **B** and **C** in all EUV band passes.

The amplitude dynamical maps confirmed the presence of standing waves along the loops **A**, **B**, and **C** in all six EUV band passes. These videos are available in the supplementary material of Conde et al. (2016).

We found a high spatial coincidence between the appearance of the waveform shown in Figure 6.9 and 6.10 and the shape of the loops seen in Figure 6.4(a)–(c).

Furthermore, these waves appeared in all moments of C1.9 flare, starting at loop **A** and continuing at loops **B** and **C**.

Figure 6.10 - Amplitude narrowband maps for waves of 19 minutes in loops **B** and **C**.

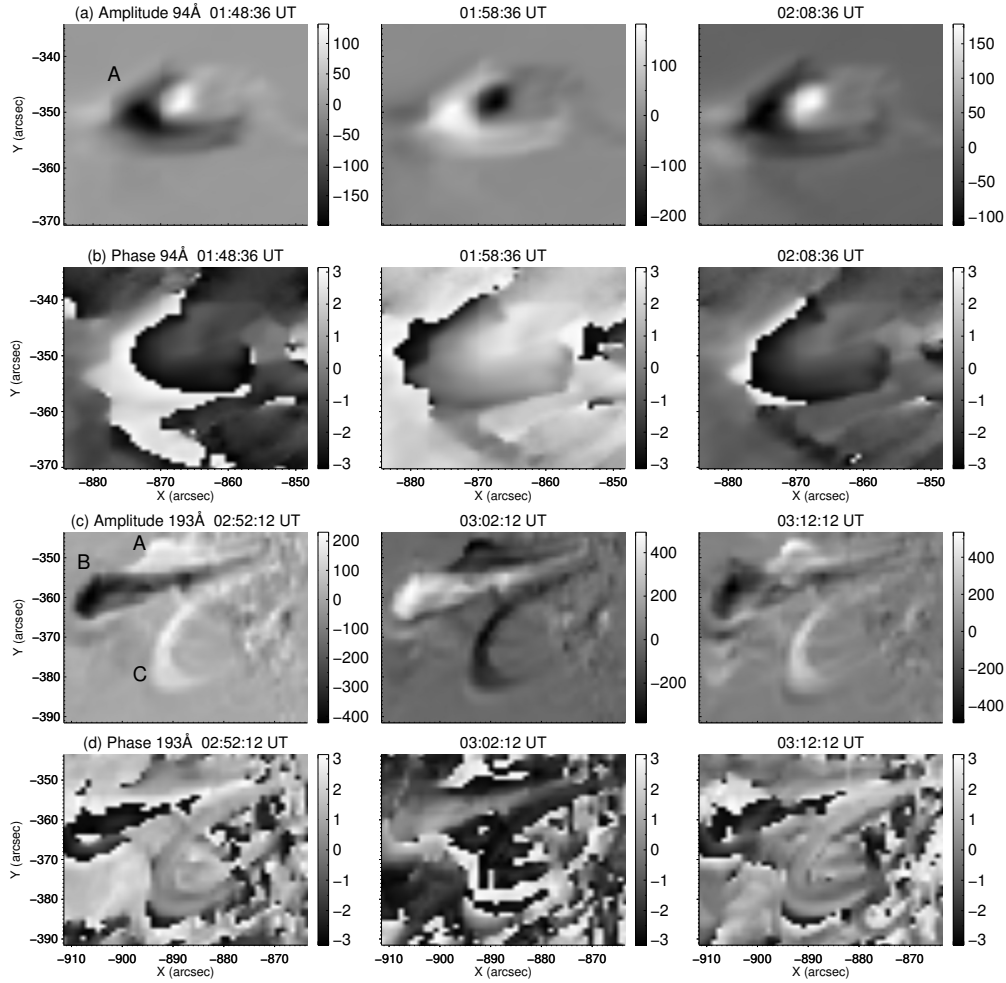


The waves were seen in 131 Å (a), 335 Å (b), 94 Å (c), 171 Å (d), 193 Å (e) and 211 Å (f). The colorbar indicate the variation between the maxima and minima of amplitude.

SOURCE: Conde et al. (2016).

Figures 6.11(a) and (c) show snapshots of amplitude narrowband maps (in arbitrary units) for 94 and 193 Å in three different instants of time (spaced 10 minutes each other). The time variation of the loops' bright and dark regions shows a static wave behaviour, which also is seen in the phase narrowband maps (in rad), Figure 6.11(b) and (d). This characteristic was seen in all data cubes studied and during all stages of C1.9 flare.

Figure 6.11 - Amplitude and phase narrowband maps for waves of 19 minutes.



Amplitude (arbitrary units) and phase (rad) narrowband maps for loops **A** in 94 Å (a)–(b) and loops **B** and **C** in 193 Å (c)–(d) for standing waves of 19 minutes.

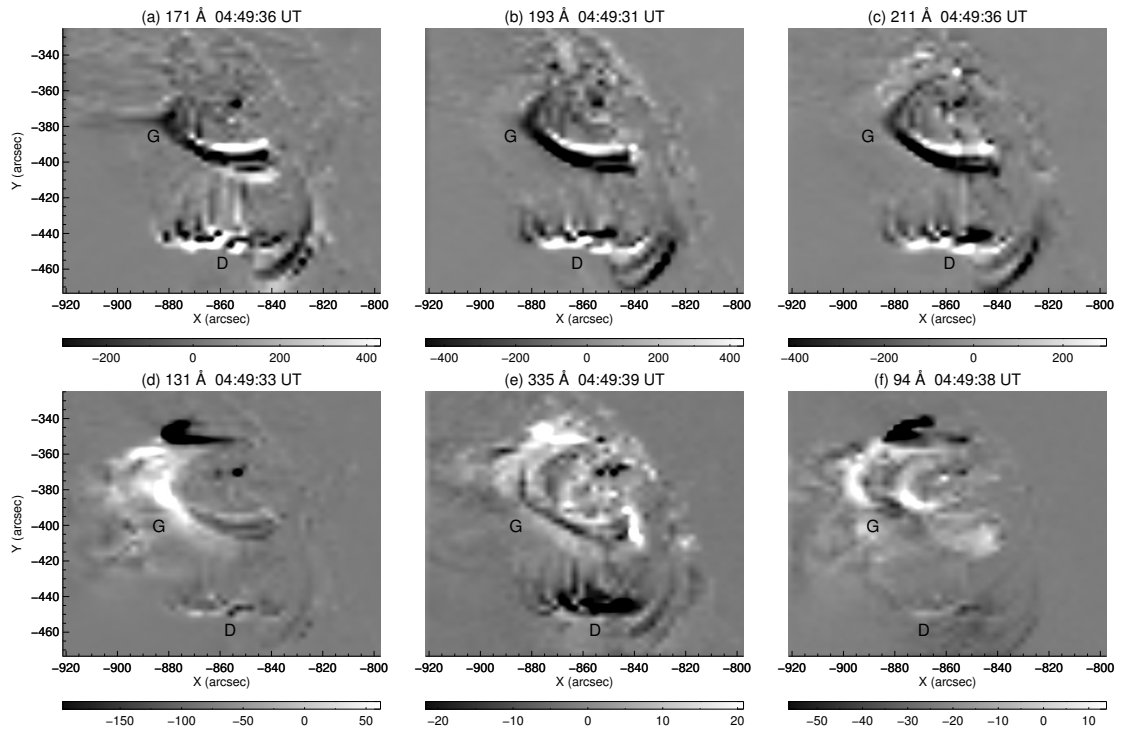
SOURCE: Conde et al. (2016).

We also found standing waves of 19 minutes along the loops **D**, **E**, **F**, and **G**, showed in Figure 6.4(d)–(f), just after of the C1.9 flare and during the C2.3 flare.

From 03:45:00 UT to 04:44:48 UT we observed waves along the loop **G** in 94 and 131 Å, also in loops **E**, **F**, and **D** in 171, 193, 211, and 335 Å. In the same time interval, we saw the waves along the loop **D** in 131 Å, in loop **A** in 94 Å, in footpoint of loop **F** and near to the footpoint of the loops **E** and **A**, in 1600 Å. In the same manner, we found waves in loops **D** and **G** from 04:15:00 UT to 05:14:48 UT in 131,

171, 193, 211, and 335 Å. For this period of time we saw waves along the loop **G** in 94 Å and in one footpoint of loop **F** in 1700 Å. After that, between 04:45:00 UT and 05:39:48 UT, we observed waves in loops **D** and **G** in 171, 193, 211, and 335 Å. In addition, these waves were seen again in loop **A** in 94, 131, 171, 193, 211, and 335 Å, and in loop **B** in 171, 193, and 211 Å.

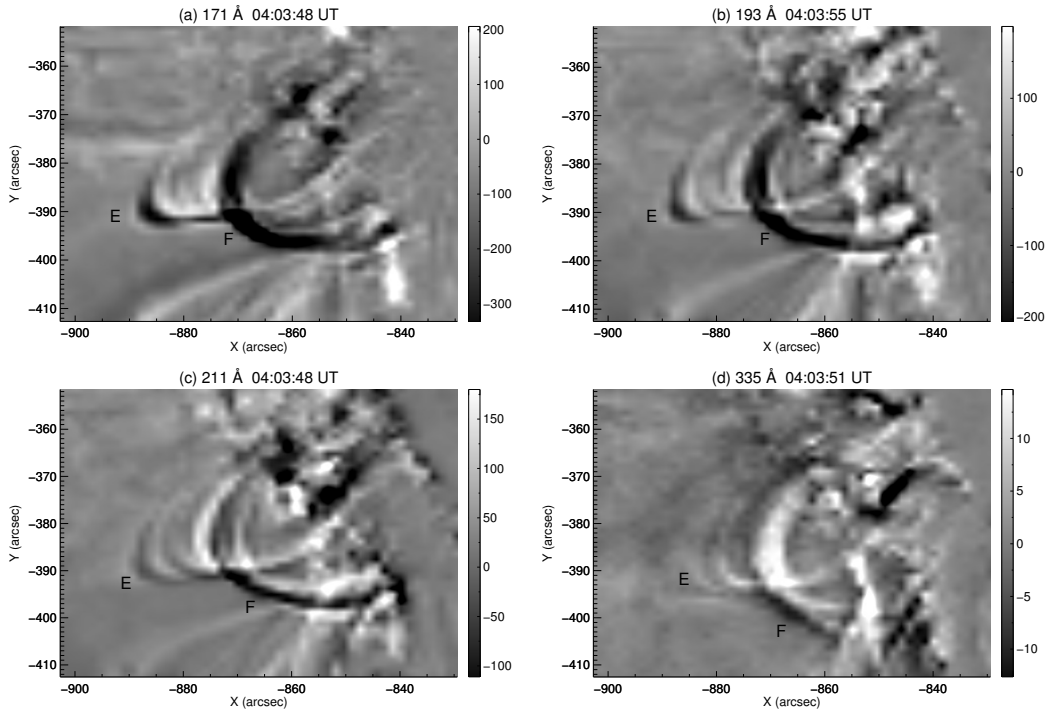
Figure 6.12 - Amplitude narrowband map for waves of 19 minutes in loops **D** and **G**.



Amplitude (arbitrary units) narrowband map for loops **D** and **G** in 171, 193, 211, 131, 335, and 94 Å **(a)–(f)** for standing waves seen at 04:49:36 UT.

SOURCE: Author production

Figure 6.13 - Amplitude narrowband maps for waves of 19 minutes in loops **E** and **F**.



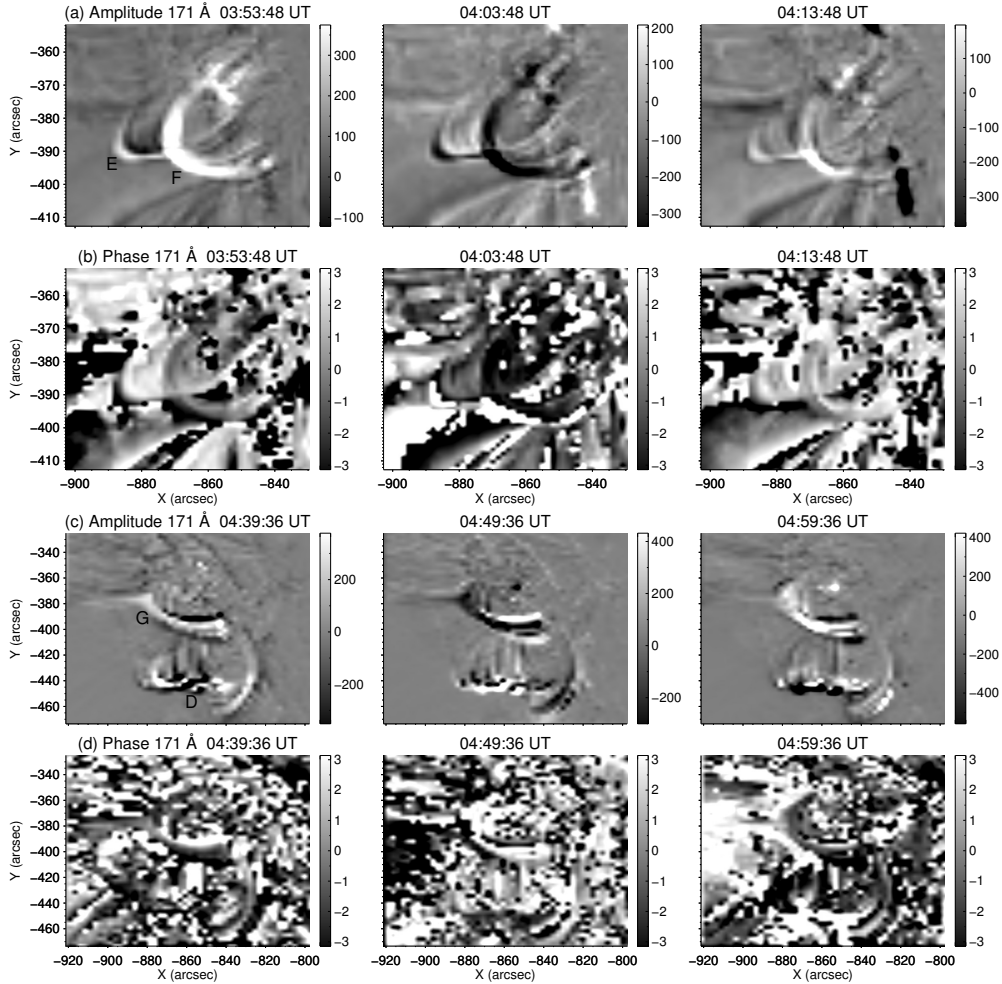
Amplitude (arbitrary units) for loops **E** and **F** observed in 171, 193, 211, and 335 Å (a)–(d) at 04:03:48 UT.

SOURCE: Author production

Figures 6.12 show waves along the loops **D** and **G**. For loops **D** the oscillation is more evident in 171 Å (panel (a)), however in 193, 211, and 335 Å (panels (b), (c), and (e), respectively) these waves were seen in the their top. For 131 and 94 Å the oscillation is slightly visible at the top of **D** (panels (d) and (f), respectively). These waves are in phase for 171, 193, and 211 Å band passes, but they are out of phase with respect to 131, 335, and 94 Å. In the same form, Figure 6.13 shows standing waves found along the loops **E** and **F**, which are in phase for 171 and 193 Å (panels (a) and (b), respectively) and out of phase with 335 Å (panel (d)). It is clearly visible the spatial coincidence between the waveform and the loops shape.

In Figure 6.14 we show the amplitude and phase narrowband maps for waves of 19 minutes along the loops **D**–**G** in 171 Å. The phase narrowband maps (panels (b) and (d)) confirm the existence of standing waves in these loops, which is clearly visible in the amplitude maps (panels (a) and (c)).

Figure 6.14 - Amplitude and phase narrowband maps for waves of 19 minutes from the loops **D** to **G**.



(a) Amplitude (arbitrary units) for loops **E** and **F** observed in 171 \AA . (c) Amplitude for loops **D** and **G**. (b) and (d) represent the phase (rad) narrowband maps for (a) and (c), respectively.

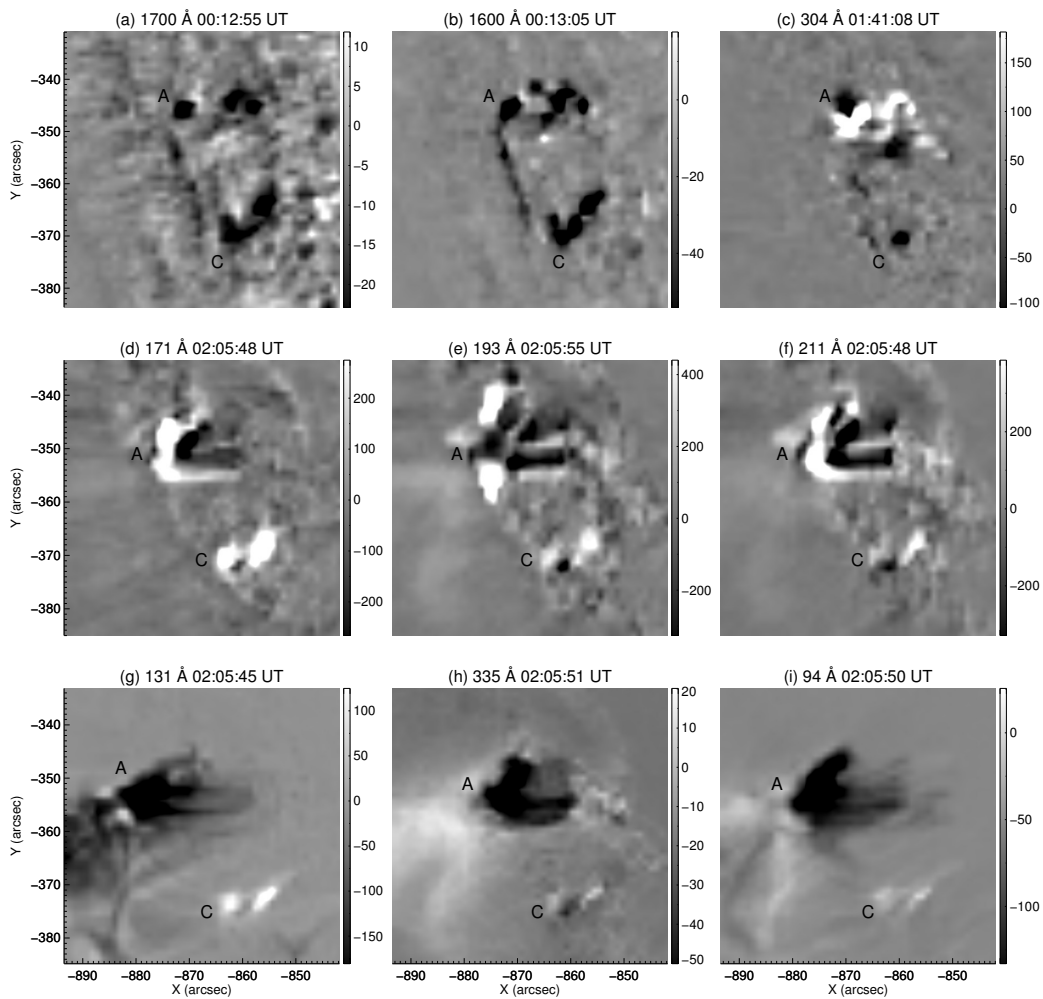
SOURCE: Author production

9-minute standing waves

We found standing waves in the period-band of 9 minutes ($9 \pm 3 \text{ min}$) along the loop **A** and footpoint regions of the loops **A** and **C**. These waves were seen in 1700 , 1600 and 304 \AA for loop **A**, in 131 and 94 \AA for loops **B** and **C** and in 131 \AA for loop **D**. They appeared from $23:45:00 \text{ UT}$ (just before the B3.8 flare starts) to

00:29:38 UT (after the flare ends). We also saw these waves in loop **A** from 01:30:00 to 02:29:48 UT, in 171, 193, 211, 131, 335, and 94 Å (Figure 6.15(d)–(i)) and in loop **B** from 02:15:00 UT to 03:14:48 UT in 171, 193, 211, and 335 Å band passes (Figure 6.16(c)–(f)). Figures 6.15(a)–(c) show waves of 9 minutes connecting the footpoint regions of loops **A** and **C**, between 00:13:00 UT and 01:41:00 UT.

Figure 6.15 - Amplitude narrowband maps for waves of 9 minutes in loop **A** and footpoint of loop **C**.

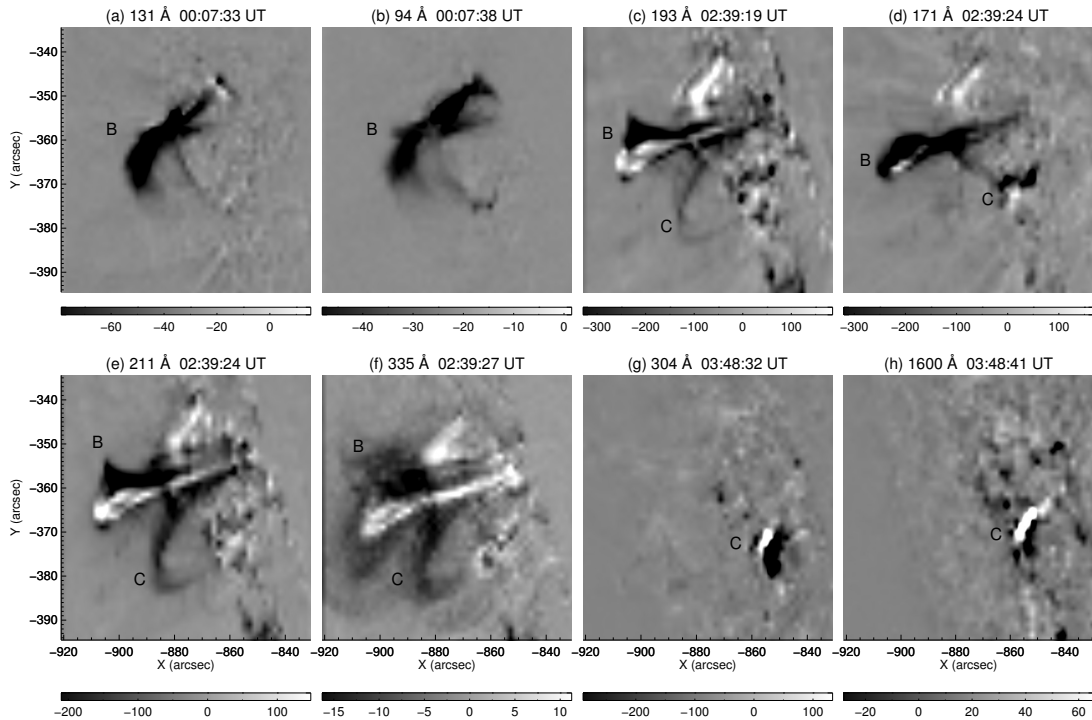


Amplitude (arbitrary units) narrowband map for loop **A** and footpoint of loop **C** in 1700, 1600, 304, 171, 193, 211, 131, 335, and 94 Å (a)–(i), respectively.

SOURCE: Author production

Figures 6.16(a) and (b) show 9-minute waves found along the loop **B** in 131 and 94 Å at 00:07:33 UT and 00:07:38 UT, respectively. Waves in footpoint of the loop **C** in 304 and 1600 Å were seen at 03:48:32 UT and 03:48:41 UT, respectively as is shown in 6.16(g) and (h).

Figure 6.16 - Amplitude narrowband maps for waves of 9 minutes in loops **B** and **C**.

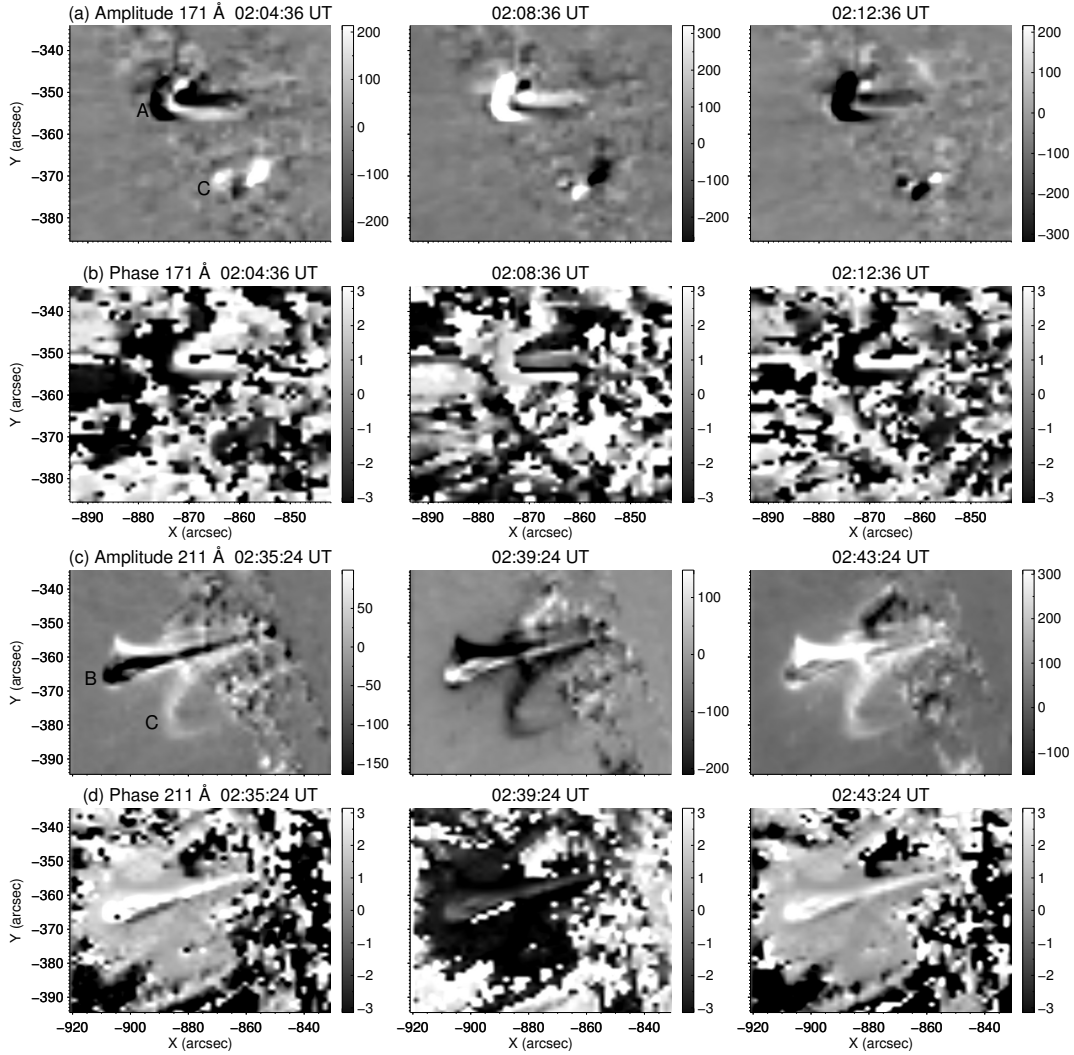


Amplitude (arbitrary units) narrowband map for loop **B** in 131 Å (a) and 94 Å (b). Panels (c)–(f) show loops **B** and **C** in 193, 171, 211, and 335 Å. In panels (g) and (h) the presence of waves is centered on the footpoint of loop **C** in 304 Å at 03:48:32 UT and 1600 Å.

SOURCE: Author production

Figure 6.17 shows a sequence of amplitude narrowband maps for 9-minute waves observed along of loops **A** in 171 Å (panel (a)), and **B** and **C** in 211 Å (panel (c)). The phase narrowband maps clearly shows standing waves for these loops (see panels (b) and (d)). Videos showing the development of these waves are available in the supplementary material of Conde et al. (2016).

Figure 6.17 - Amplitude and phase maps for waves of 9 minutes in loops **A**, **B**, and **C**.



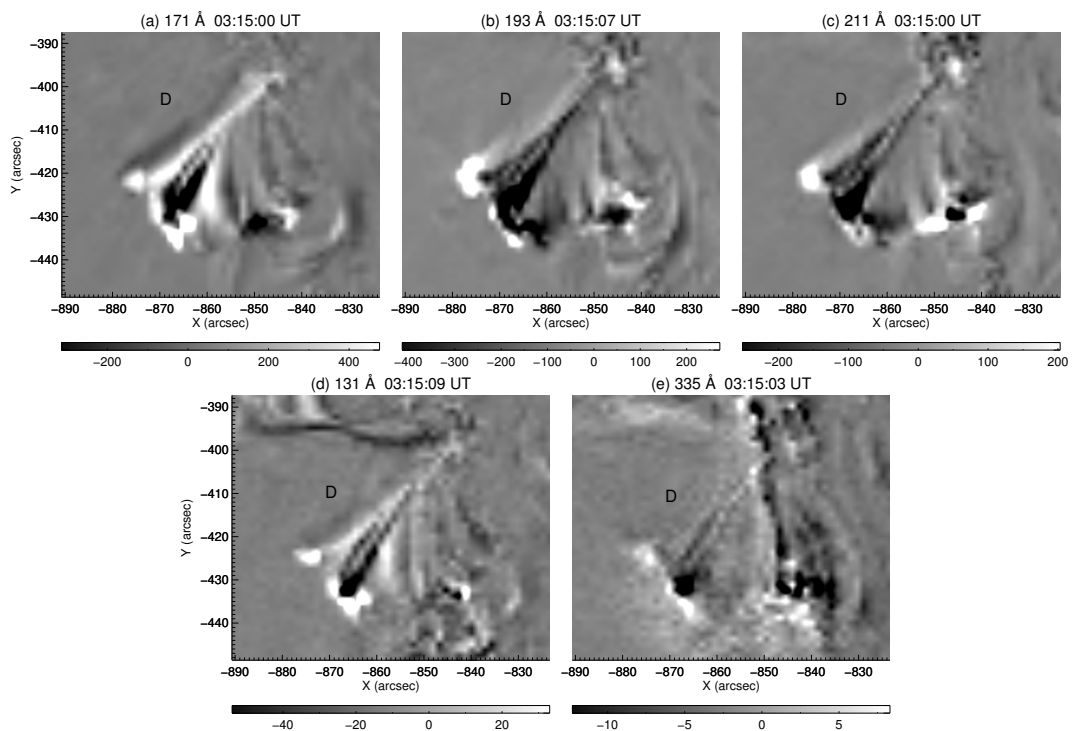
(a) Amplitude (arbitrary units) for loop **A** and footpoint of **C** observed in 171 Å. (c) Amplitude for loops **B** and **C** observed in 211 Å. Panels (b) and (d) represent the phase (rad) narrowband maps for (a) and (c), respectively.

SOURCE: Author production

The temporal interval of waves found in loops **A**, **B**, and **C** correspond to the C1.9 flare. However, we also detected waves of 9 minutes during the period of C1.9 and C2.3 flares in loops **D**, **E**, **F**, **G**, and footpoint of the loop **C**. We saw these waves from 03:30:00 UT to 04:14:48 UT along the loops **E** and **F** in 171, 193, 131 and 94 Å as is shown in Figures 6.19(a)–(d), respectively. In loop **D** they were seen from 02:45:00 UT to 05:39:48 UT in 171, 193, 211, 335 and 131 Å (see Figures 6.18(a)–(e),

respectively). In one footpoint of loop **C** we saw waves from 03:29:53 UT to 04:14:41 UT in 1600 Å and from 03:45:00 UT to 04:14:48 UT in 304 Å and again in the loops **B** and **C** from 04:30:00 UT to 05:14:48 UT in 335 Å. Between 04:00:00 UT and 05:39:48 UT we found waves in the loop **G** in 171, 193, 211, 131, 335, and 94 Å (Figures 6.21(a)–(f), respectively). Also, we saw oscillatory presence along the loop **A** in 131 and 94 Å around of 04:55:48 UT in the same Figures 6.21(d) and (f).

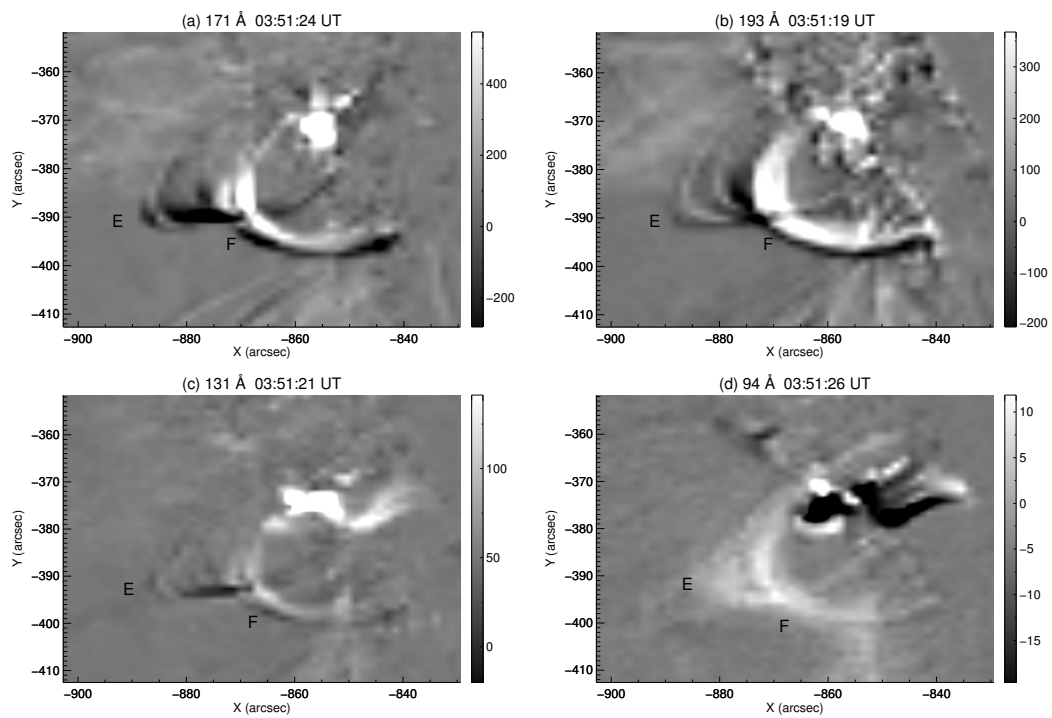
Figure 6.18 - Amplitude narrowband maps for waves of 9 minutes in loop **D**.



Amplitude (arbitrary units) for loop **D** observed in 171 (a), 193 (b), 211 (c), 131 (d), and 335 Å (e) at 03:15:00 UT.

SOURCE: Author production

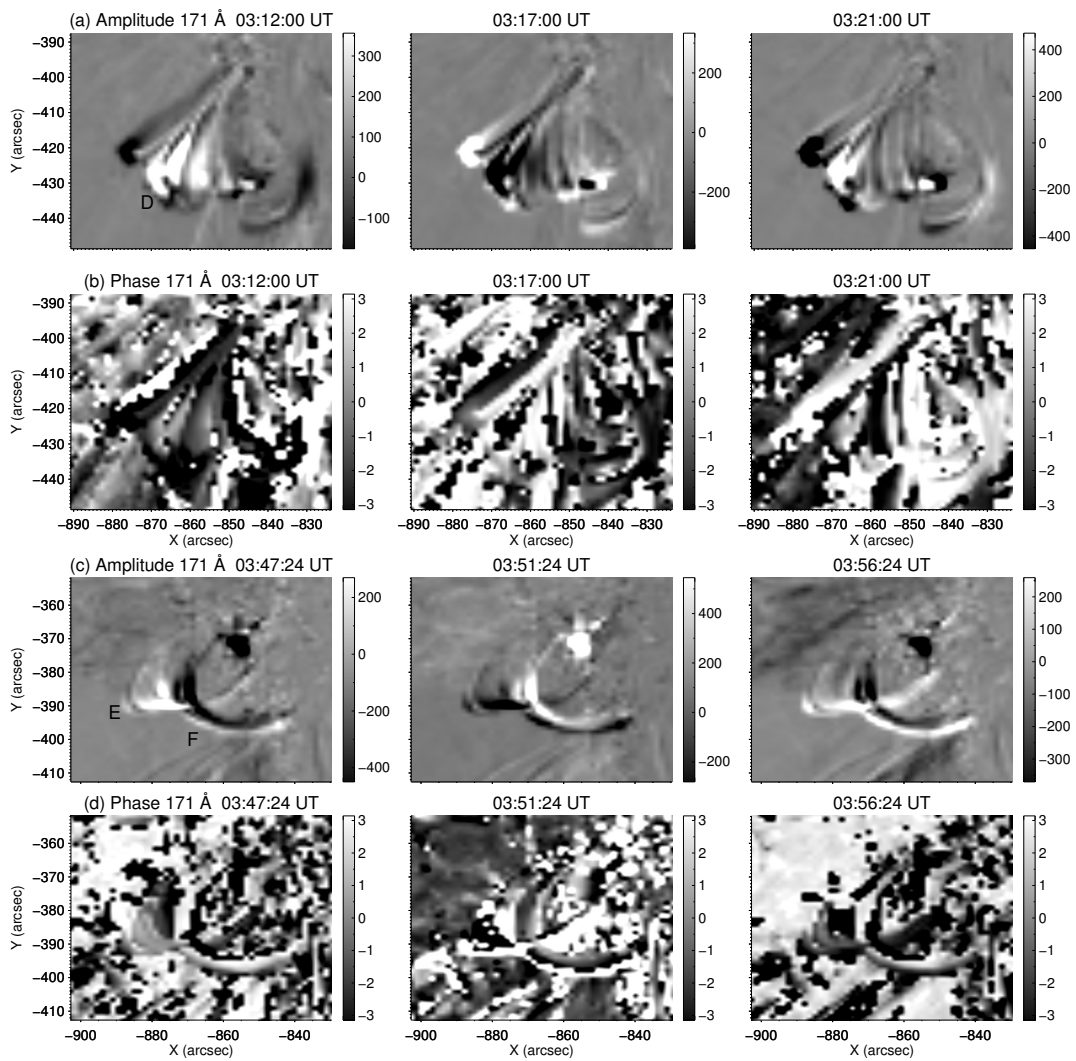
Figure 6.19 - Amplitude narrowband maps for waves of 9 minutes in loops **E** and **F**.



Amplitude (arbitrary units) narrowband map of standing waves in loops **E** and **F** in 171 (a), 193 (b), 131 (c), and 94 Å (d) around of 03:51:24 UT.

SOURCE: Author production

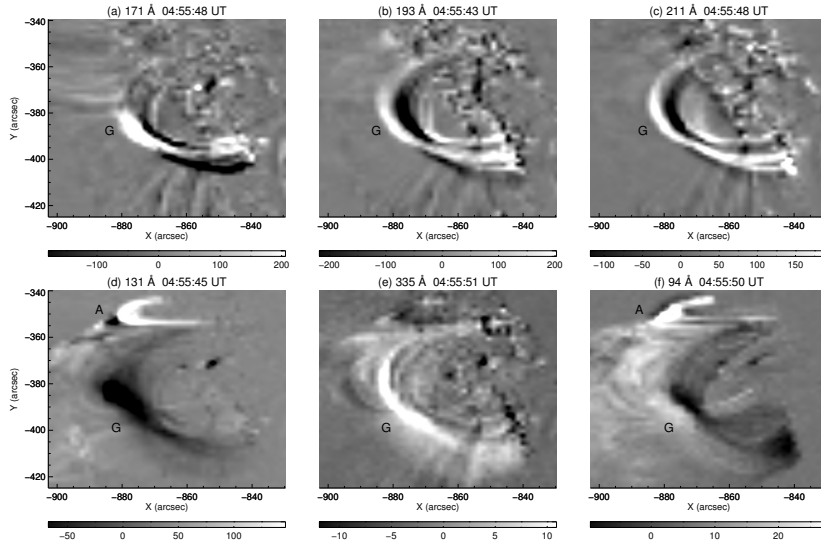
Figure 6.20 - Amplitude and phase for waves of 9 minutes in loops **D**, **E**, and **F**.



(a) Amplitude (arbitrary units) and for loop **D** in 171 Å. (c) Amplitude for loops **E** and **F** in 211 Å. (b) and (d) represent the phase (rad) for (a) and (c), respectively.

SOURCE: Author production

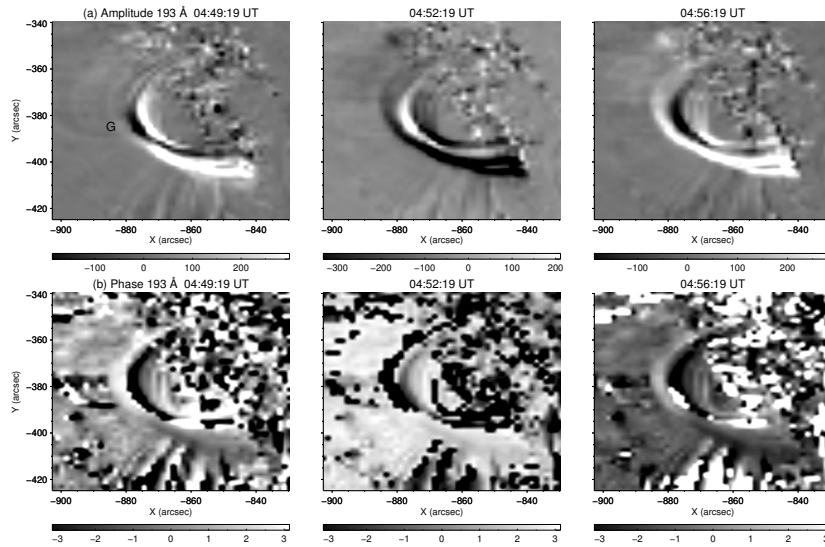
Figure 6.21 - Amplitude narrowband maps for waves of 9 minutes in loop **G**.



Amplitude (arbitrary units) for loop **G** observed in 171 (a), 193 (b), 211 (c), 131 (d), 335 (e), and 94 Å (f) around 04:55:45 UT.

SOURCE: Author production

Figure 6.22 - Amplitude and phase narrowband maps for waves of 9 minutes in loop **G**.



(a) Amplitude (arbitrary units) for loop **G** in 193 Å. (b) The phase (rad) narrowband maps shows the presence of standing waves.

SOURCE: Author production

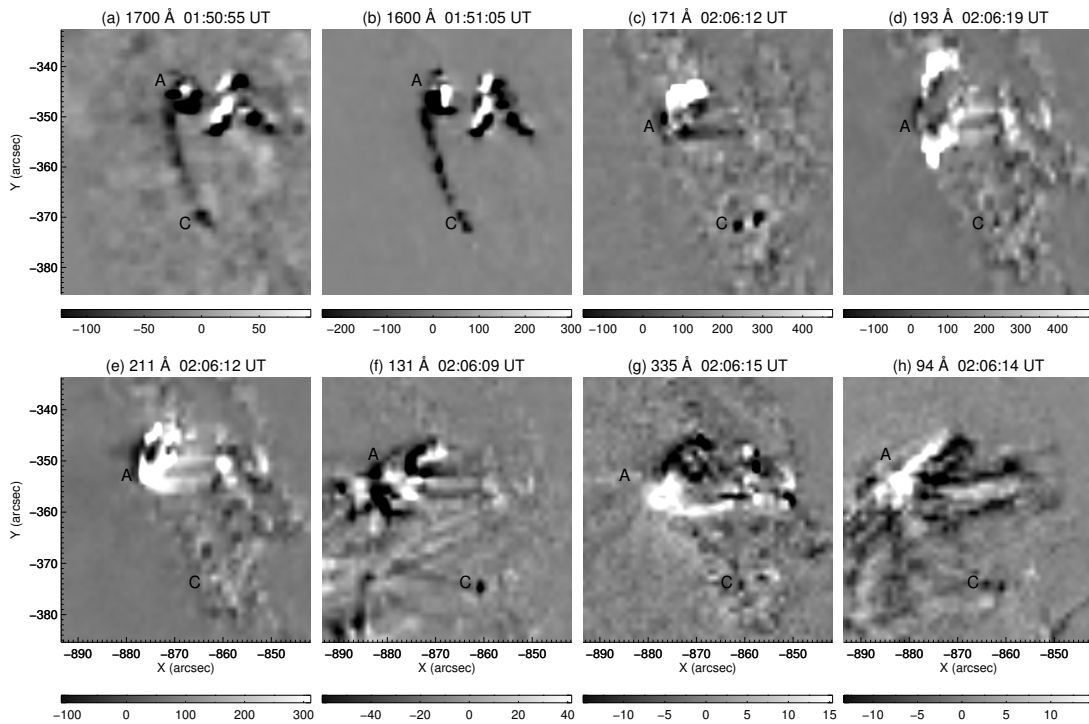
The phase narrowband confirmed that the oscillations found along the loops **D**, **E**, **F** (Figures 6.20(a)–(b), and (c)–(d), respectively), and **G** (Figures 6.22(a)–(b)) are standing waves. We also saw that exists a high spatial coincidence between the waveform and the loops shape.

5-minute standing waves

We found 5-minute waves (5 ± 2 min) in the loops **A**–**D** and **G** of Figure 6.4, in the corresponding time of B3.8, C1.9, and C2.3 class flares.

During the B3.8 flare we found waves in loop **A** from 23:45:00 UT to 00:14:48 UT in 304 \AA and in loop **C** between 00:00:00 UT and 00:29:48 UT in 94 \AA . On the footpoint **1** of loop **C** (see Figure 6.4) we detected these waves from 00:00:00 UT to 00:26:36 UT in 304 \AA .

Figure 6.23 - Amplitude narrowband maps for waves of 5 minutes in loop **A** and footpoint **1** of loop **C**.

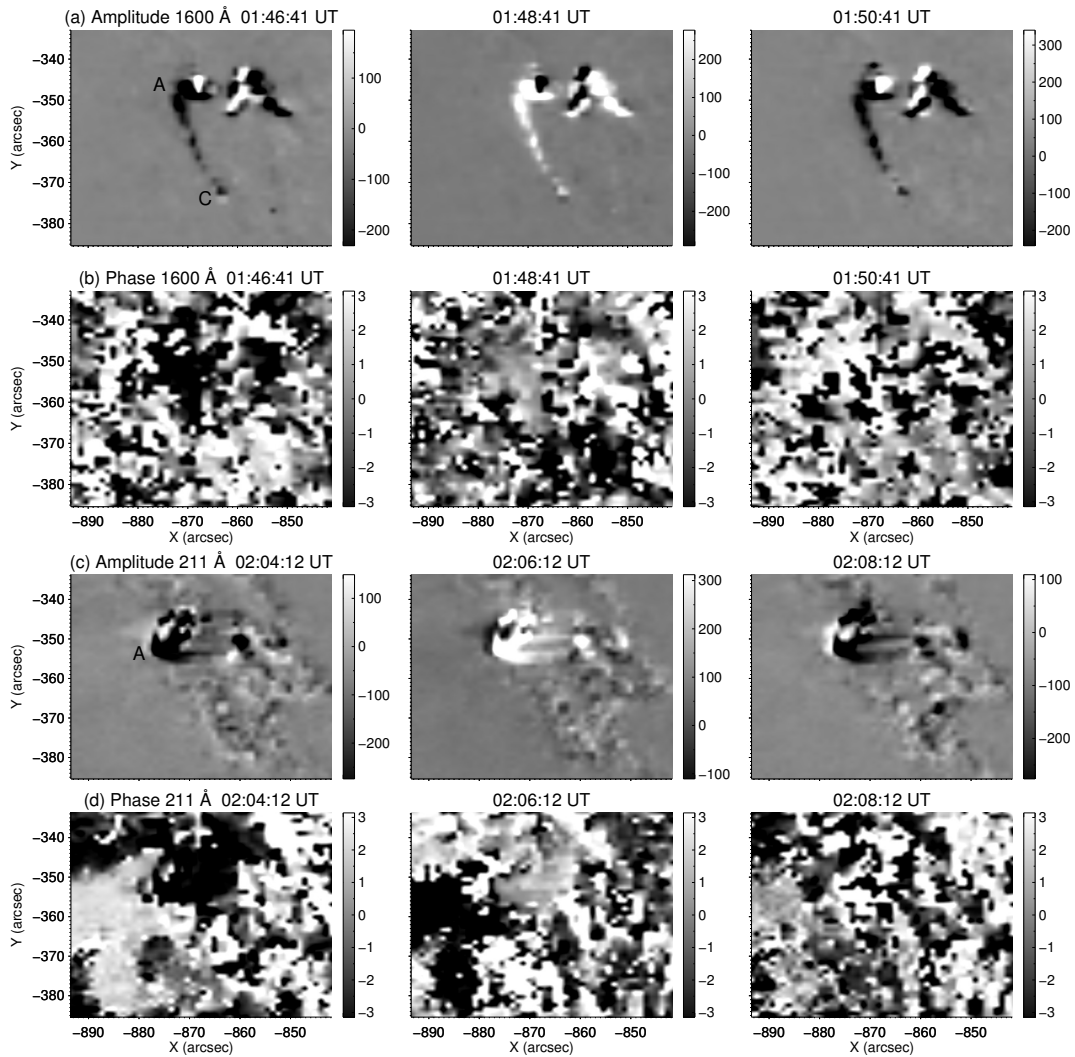


(a)–(b) waves between the loops **A** and **C** in 1700 and 1600 \AA at $01:50:55$ UT. (c)–(h), waves in loop **A** 171 , 193 , 211 , 131 , 335 , and 94 \AA around of $02:06:12$ UT.

SOURCE: Author production

Figure 6.23(a) and (b) shows waves of 5 minutes from region of loop **A** to **C** seen in 1700 and 1600 Å at 01:50:55 UT. These waves also were seen along the loop **A** (Figure 6.23(c)–(h)) in 171, 193, 211, 131, 335, and 94 Å around of 02:06:12 UT. Panels (c) and (f) show waves in the footpoint **1** of loop **C** in 171 and 131 Å, respectively.

Figure 6.24 - Amplitude and phase for waves of 5 minutes in loops **A** and **C**.



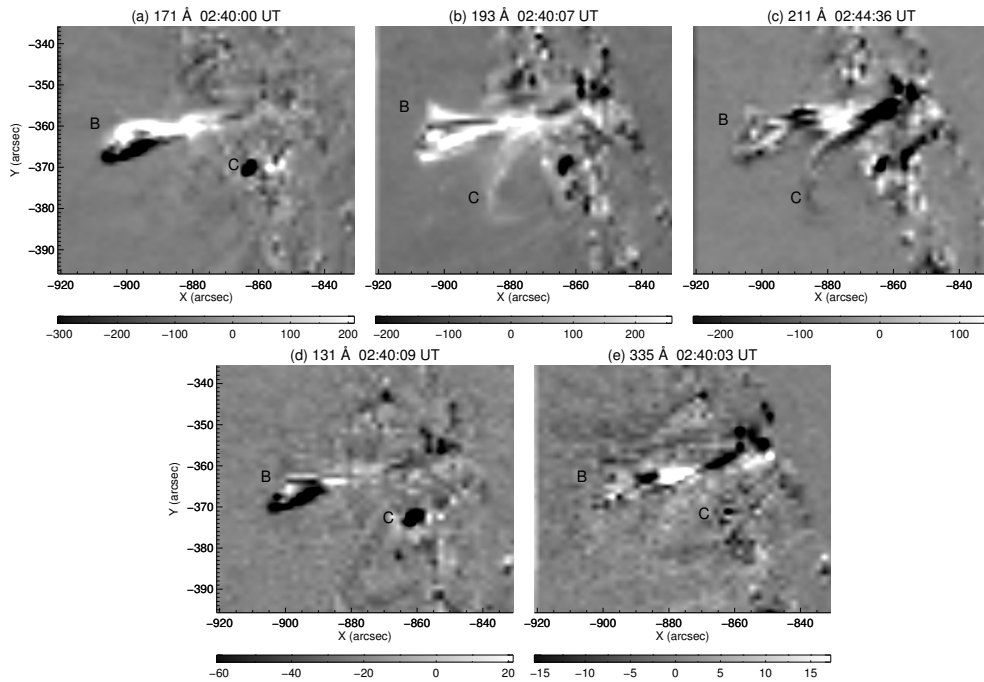
(a) Amplitude (arbitrary units) for loop **A** and footpoint **1** of the loop **C** observed in 1600 Å. (c) Amplitude for waves observed in 211 Å along of loop **A**. Panels (b) and (d) represent the respective phase (rad) for (a) and (c)

SOURCE: Author production

During the C1.9 flare, between 01:29:53 UT and 02:29:48 UT we found waves in loop **A** in 1700, 1600, 304, 171, 193, 211, 131, 335, and 94 Å. Also we saw waves in loops **B** and **C** from 02:15:00 UT to 03:11:00 UT in 171, 193, 211, 131, and 335 Å. We found waves in the footpoint **1** of the loop **C** from 01:45:00 UT to 03:23:24 UT in 1600, 304, 171, 131 and 94 Å and in loop **D** from 03:15:00 UT to 03:44:48 UT in 131 Å.

Figure 6.25 shows the amplitude narrowband map in arbitrary units for waves along the loop **B** in 171, 193, 211, 131 and 335 Å around of 02:40:00 UT. Loop **C** is seen oscillating in 193 and 211 Å (6.25(b)–(c) respectively). Footpoint **1** of loop **C** is observed in 171, 131 and 335 Å (6.25(a),(d), and (e), respectively).

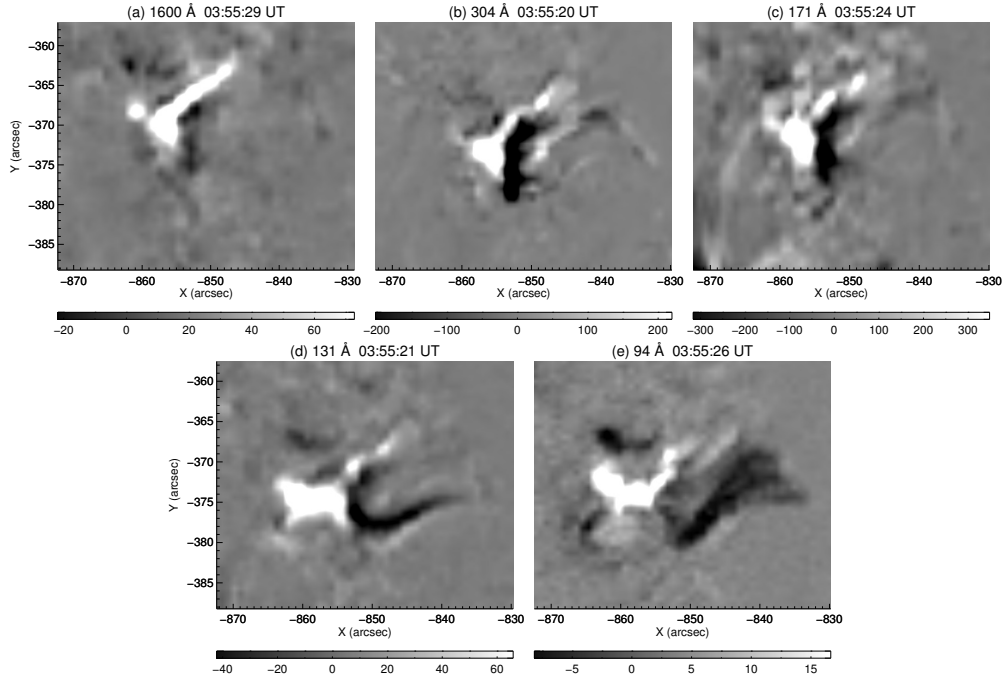
Figure 6.25 - Amplitude narrowband maps for waves of 5 minutes in loops **B** and **C**.



Amplitude (arbitrary units) for standing waves in loop **B** and footpoint **1** of **C** observed in 171, 193, 211, 131 and 335 Å around of 02:40:00 UT (a)–(e). In panels (b) and (c) are shown waves along the loop **C** in 193 and 211 Å.

SOURCE: Author production

Figure 6.26 - Amplitude narrowband maps for 5-minutes waves in footpoint 1 of loop C.



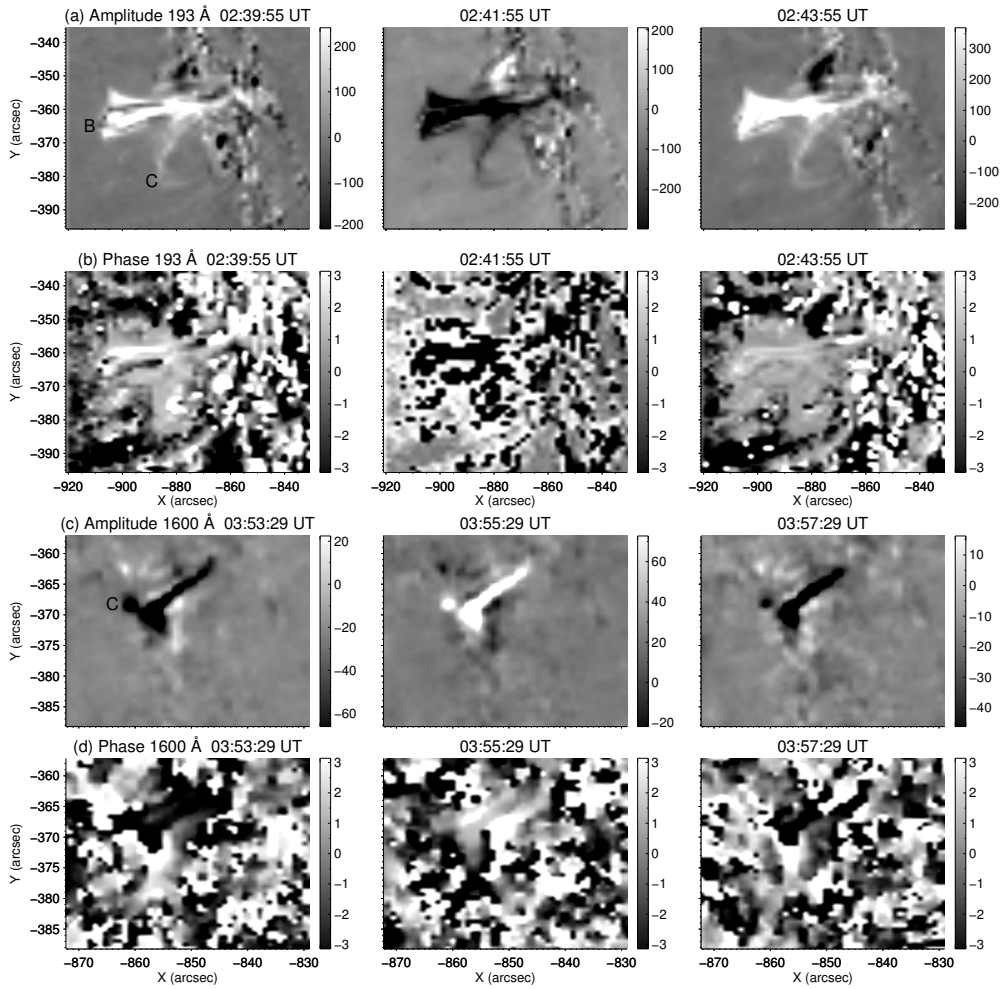
Waves seen in the footpoint 1 of loop C in 1600 (a), 304 (b), 171 (c), 131 (d) and 94 Å (e) at 03:55:20 UT.

SOURCE: Author production

Standing waves of 5 minutes were seen in the footpoint 1 of the loop C (see Figures 6.26(a)–(e)) in 1600, 304, 171, 131, and 94 Å between 03:29:53 UT and 04:14:41 UT. In the top of loop D were seen in 131, 171, 193, 211 and 335 Å from 03:20:48 UT to 04:44:48 UT (Figures 6.28(a)–(e)). This time period corresponds to C1.9 and C2.3 flares.

Finally, during the C2.3 flare, we observed waves from 04:00:00 UT to 05:39:48 UT along the loop G in 171, 193, 211, 335, and 94 Å band passes (Figure 6.29(a)–(d), respectively). From 04:45:00 UT to 05:10:12 UT these waves were seen in the footpoint 1 of loop C in 171 Å. Again, we saw waves in loop D from 03:01:12 UT to 05:39:48 UT in 171, 193, 211, and 335 Å. These loops registered waves from the begin of C1.9 flare until after of C2.3 flare. After of C2.3 flare we detected waves from 05:00:00 UT to 05:39:48 UT in 171, 193, and 211 Å in loops A, B, and C but the form of these loops is a little different.

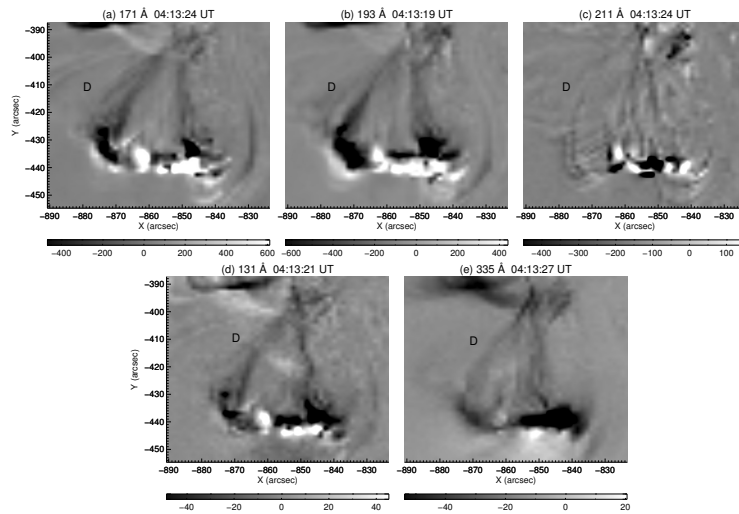
Figure 6.27 - Amplitude and phase for 5-minutes waves in loop **B** and footpoint **1** of **C**.



(a) Amplitude (arbitrary units) for loops **B** and **C** in 193 Å. (c) Amplitude for footpoint **1** of **C** in 1600 Å. Panels (b) and (d) represent the phase (rad) for (a) and (c), respectively.

SOURCE: Author production

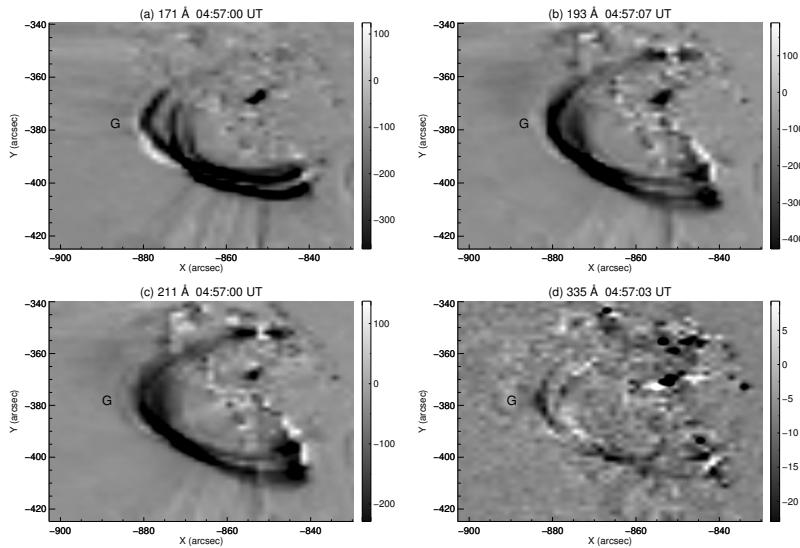
Figure 6.28 - Amplitude narrowband maps for waves of 5 minutes in loop **D**.



Amplitude (arbitrary units) for loop **D** in 171 (a), 193 (b), 211 (c), 131 (d), and 335 Å (e) at 04:13:79 UT.

SOURCE: Author production

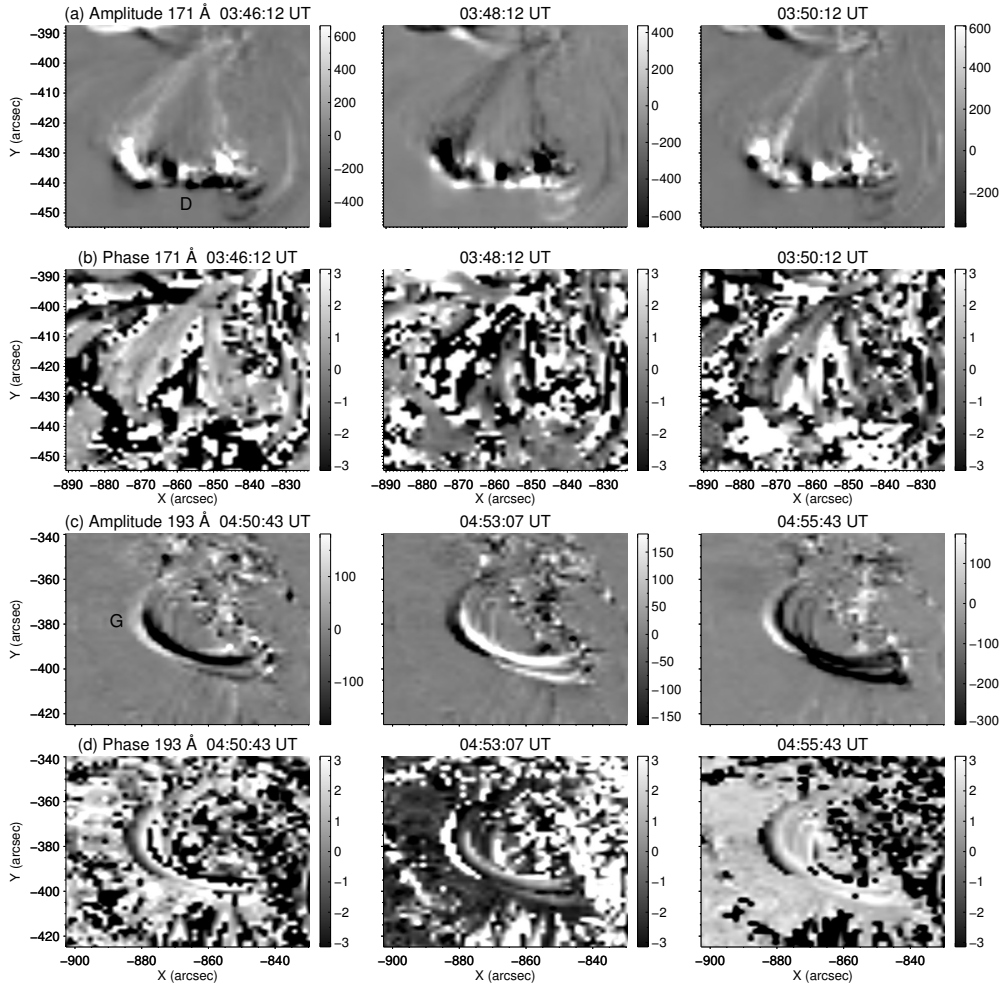
Figure 6.29 - Amplitude narrowband maps for waves of 5 minutes in loop **G**.



Amplitude (arbitrary units) for loop **G** observed in 171 (a), 193 (b), 211 (c), and 335 Å (d) around 04:57:03 UT.

SOURCE: Author production

Figure 6.30 - Amplitude and phase for waves of 5 minutes in loops **D** and **G**.



(a) and (c) Amplitude (arbitrary units) for loops **D** and **G** in 171 and 193 Å, respectively. (b) and (d) represent the phase for (a) and (c), respectively.

SOURCE: Author production

Figure 6.29 shows standing waves of 5 minutes along of loop **G** around 04:57:03 UT. These waves are highly visible along the loop **G** in 171, 193 and 211 Å (panels (a)–(c), respectively), however in 335 Å (panel (d)) is faintly visible. Figure 6.30 shows the amplitude and phase narrowband for waves of 5 minutes in loops **D** and **G** (panels (a)–(b) and (c)–(d), respectively).

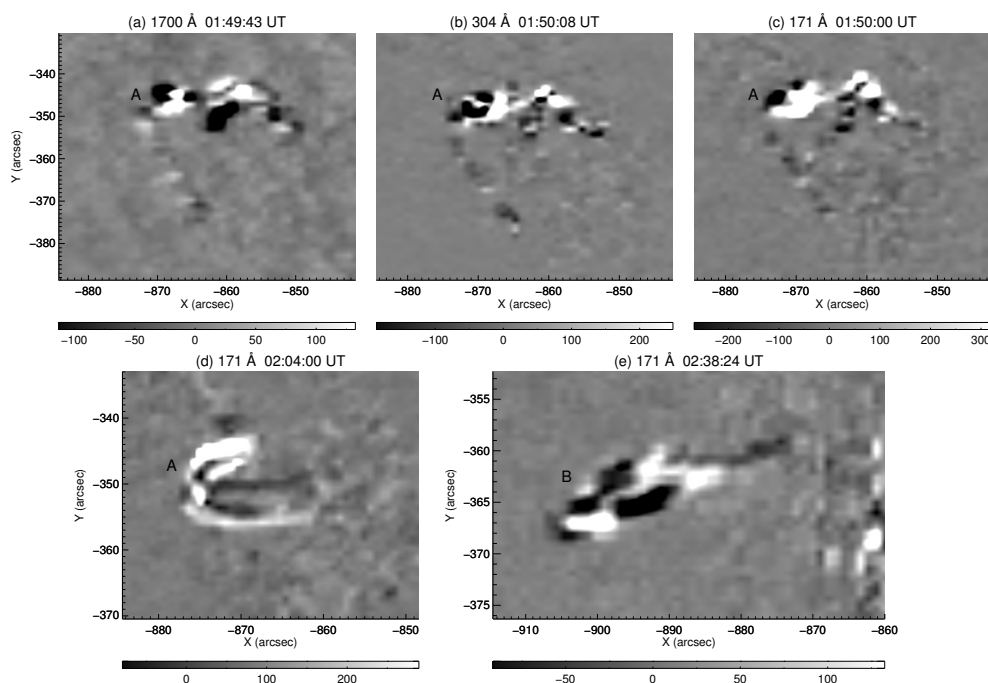
The amplitude (arbitrary units) and phase (rad) narrowband maps of Figures 6.24, 6.27, and 6.30 show clearly the presence of standing waves along the loops **A**–**G** and in the footpoints of the loops **A** and **C**.

2-minute travelling waves

We found waves in the period-band of 2 minutes (2 ± 0.8 min) for loops **A**, **B**, and **C**. They were seen in different moments of each flare mentioned in Table 6.1.

We saw these waves from 01:30:00 UT to 02:14:48 UT propagating in the footpoints of loop **A** in 1700, 304, and 171 Å (see Figure 6.31(a)–(c)). Particularly, we observed the waves along the loop **A** in 171 Å at 02:04:00 UT (Figure 6.31(d)) and along the loop **B** in 171 Å, from 02:37:36 UT to 02:44:48 UT (Figure 6.31(e)).

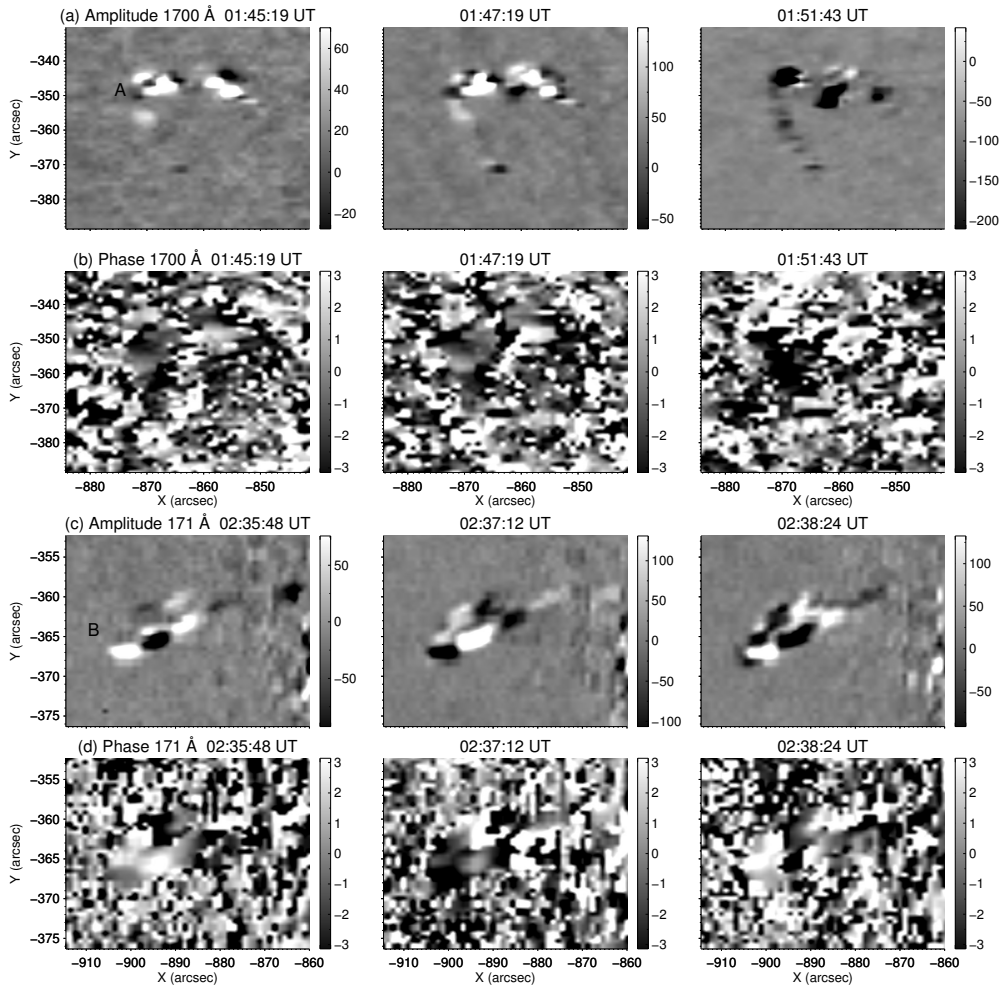
Figure 6.31 - Amplitude of 2-min travelling waves in loops **A** and **B**.



Amplitude (arbitrary units) of waves in the footpoints of loops **A** in 1700 (a), 304 (b), and 171 (c) Å, around of 01:50:00 UT. Panels (d) and (e) show waves along of loops **A** and **B** in 171 Å at 02:04:00 UT and 02:38:24 UT, respectively.

SOURCE: Author production

Figure 6.32 - Amplitude and phase maps for waves of 2 minutes in loops **A** and **B**.

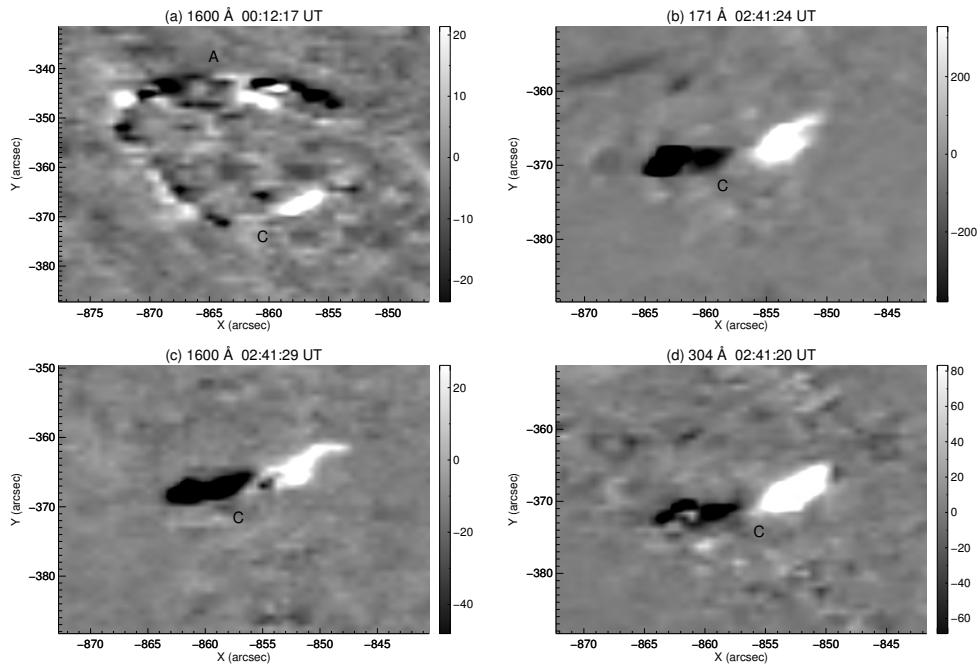


(a) Amplitude (arbitrary units) for loop **A** in 1700 Å. (c) Amplitude for **B** in 171 Å. (b) and (d) phase (rad) for (a) and (c), respectively.

SOURCE: Author production

During the B3.8 flare, between 23:56:24 UT and 00:24:36 UT, we saw 2-minute waves propagating between the footpoints of loops **A** and **C** in 1600 Å band pass (see Figure 6.33(a)). In the same manner, from 01:43:53 UT to 02:29:29 UT these waves were seen travelling from **A** to **C** footpoints in 1600 and 94 Å, but from 02:10:36 UT to 03:14:48 UT in 171, 1600, and 304 Å they were seen only in the footpoint **1** of loop **C** as is shown in Figure 6.33(b)–(d). This period correspond to C1.9 flare. Finally, during the C2.3 flare we saw travelling waves in the footpoint **1** of loop **C**, between 04:45:05 UT and 05:23:05 UT in 1600 Å.

Figure 6.33 - Amplitude narrowband maps for waves of 2 minutes in loops **A** and **C**.

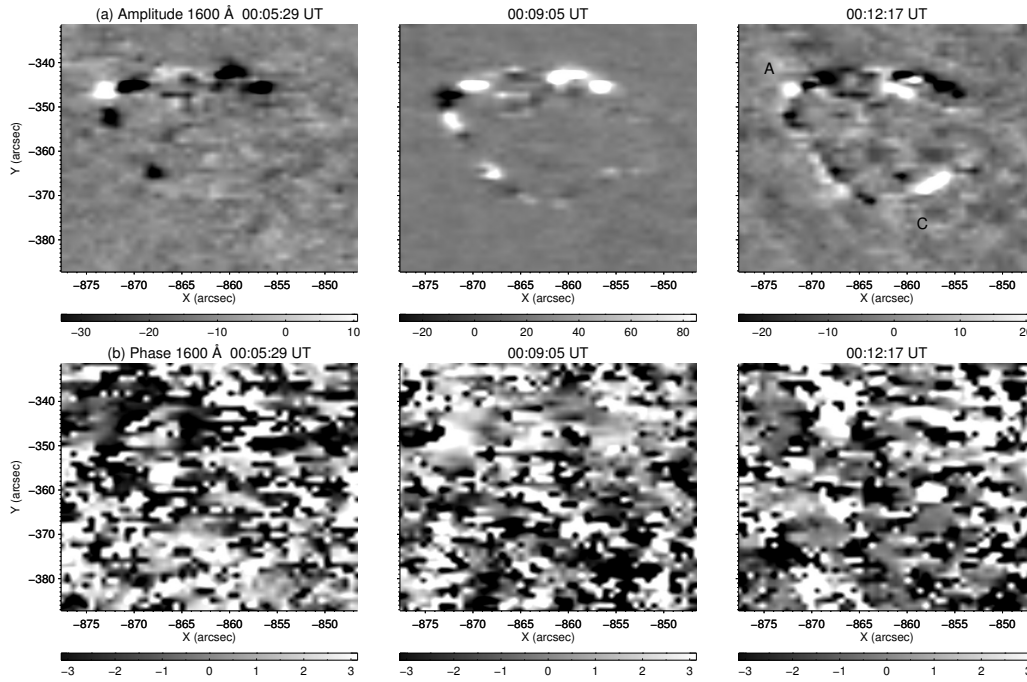


(a) Waves found in the loops **A** and **C** footpoint regions in 1600 Å at 00:12:17 UT. Panels (b)–(d), waves in the footpoint 1 of loop **C**, around of 02:41:24 UT in 171, 1600 and 304 Å, respectively.

SOURCE: Author production

The amplitude (arbitrary units) and phase (rad) narrowband maps of Figure 6.32 show waves propagating in the footpoints of loop **A** (panels (a)–(b)) and along of loop **B** (panels (c)–(d)). In addition, Figures 6.34(a)–(b) show waves moving between the loops **A** and **C** footpoint regions.

Figure 6.34 - Amplitude and phase maps for waves of 2 minutes in loops **A** to **C**.



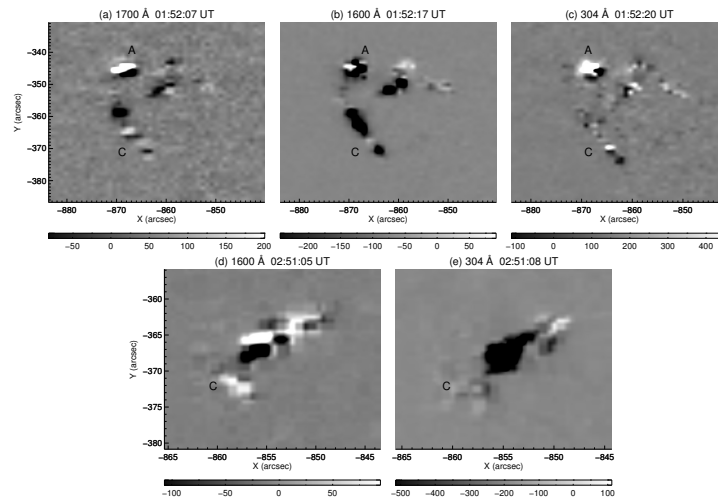
Amplitude in arbitrary units (a) and phase in rad (b) narrowband maps for travelling waves from loop **A** to **C** footpoints in 1600 Å.

SOURCE: Author production

1-minute travelling waves

We found 1-minute (1 ± 0.4 min) travelling waves in the chromosphere and temperature minimum regions. These waves were seen during the B3.8 flare in the footpoints of loop **A**, from 00:04:00 UT to 00:19:53 UT in 1600 and 304 Å. In the same loop, but during the C1.9 flare the waves appeared from 01:30:00 UT to 02:29:29 UT in 1700, 1600 and 304 Å as is shown in Figure 6.35(a)–(c). The waves were seen in the footpoint **1** of loop **C**, from 02:42:41 UT to 03:57:36 UT in 1600 and 304 Å (see Figure 6.35(d) and (e)) and during the C2.3 flare, from 04:57:24 UT to 05:12:24 UT in 304 Å. In Figure 6.36 we show the amplitude and phase narrowband (panels (a) and (b), respectively) for travelling waves of 1 minute in the footpoint area of the loops **A** and **C** in 1700 Å.

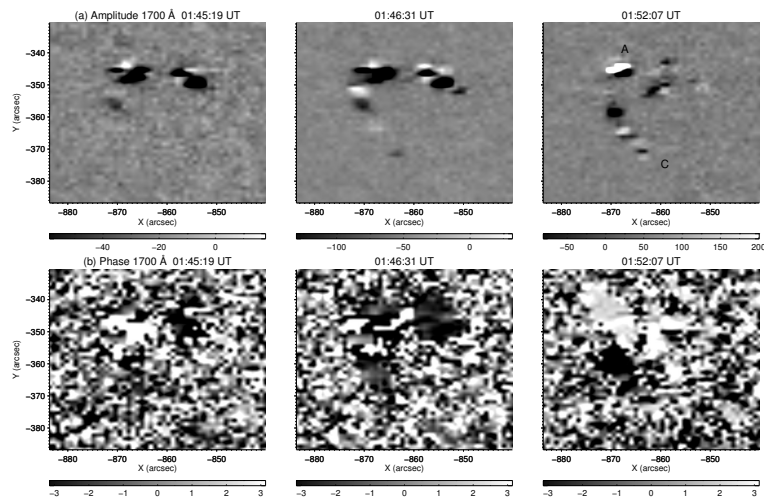
Figure 6.35 - Amplitude narrowband maps for travelling waves of 1 minute in the footpoints of the loops **A** and **C**.



Panels (a)–(c) waves in the footpoint regions of the loop **A** and **C** around of 01:52:17 UT in 1700, 1600, and 304 Å, respectively. Panels (d) and (e), waves in the footpoint of loop **C**, around of 02:51:05 UT in 1600 and 304 Å, respectively.

SOURCE: Author production

Figure 6.36 - Amplitude and phase maps for waves of 1 minute between the loops **A** to **C** footprints.



Amplitude (arbitrary units) and phase (rad) for waves propagating between the loops **A** to **C** footprint area.

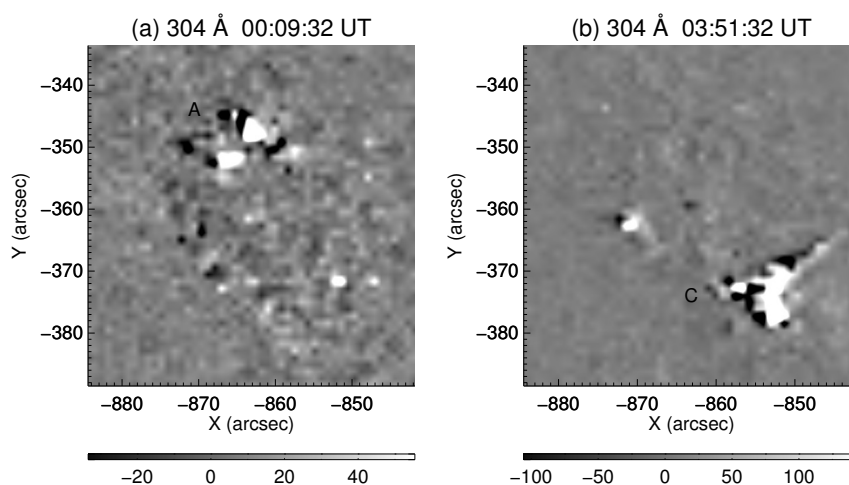
SOURCE: Author production

36-second travelling waves

We found 36-second (36 ± 12 s) waves in 304 \AA . We detected these waves in the footpoints of loop **A** from 00:06:48 UT to 00:12:36 UT (Figure 6.37(a)) and from 01:32:36 UT to 01:59:48 UT, i.e., during the B3.8 and C1.9 flares, respectively. We also saw these waves in the footpoint **1** of loop **C** from 03:48:24 UT to 03:55:48 UT (Figure 6.37(b)) and between 04:58:24 UT and 05:14:48 UT, i.e., during the period without flares and ending the C2.3 flare, respectively.

In Figure 6.38 we show the amplitude and phase narrowband for travelling waves of 36 seconds in the footpoints of loops **A** and **C**. In panel (a) the waves are triggered in the footpoint **1** of loop **A** and moves toward the footpoint **1** of loop **C**. In panel (c) these waves start in the footpoint **1** of loop **C** and propagate outward in three different directions.

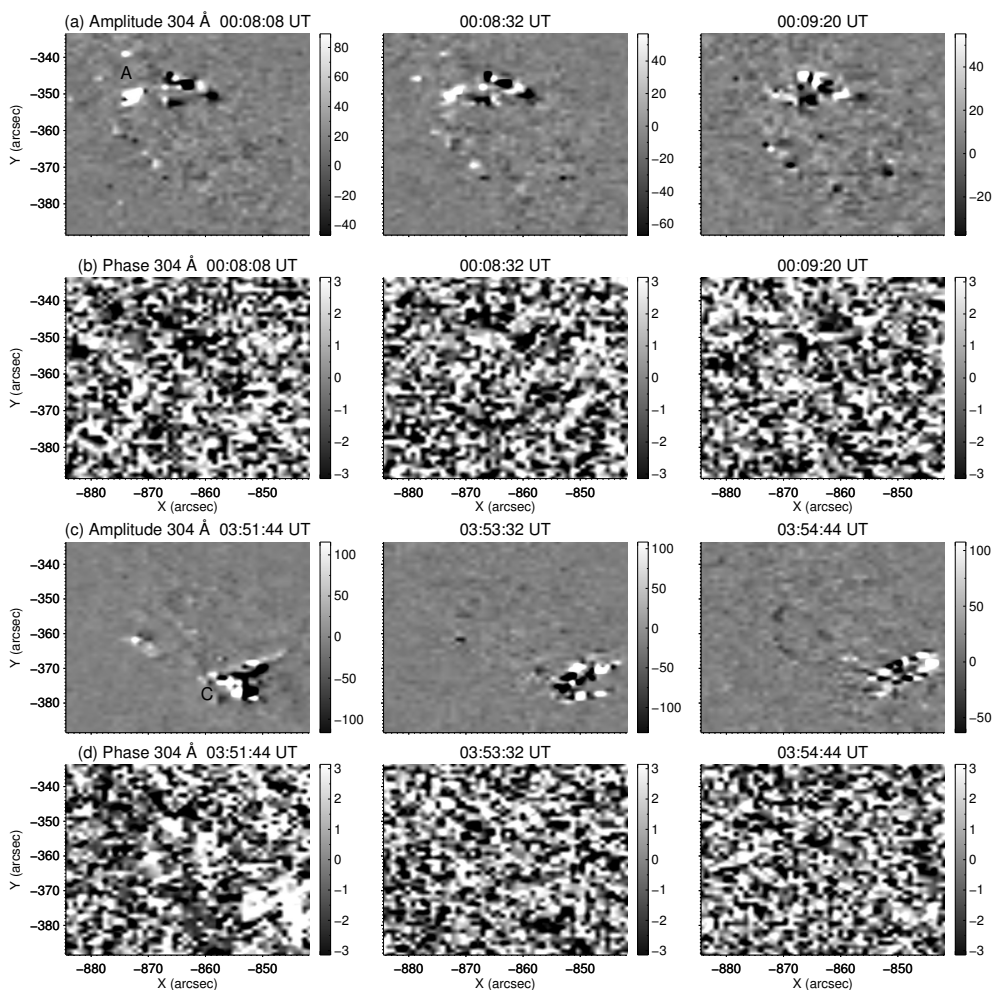
Figure 6.37 - Amplitude narrowband maps for waves of 36 seconds in the footpoint of loops **A** and **C**.



Amplitude (arbitrary units) for waves found in 304 \AA . (a) Footpoint region of loop **A** at 00:09:32 UT. (b) Footpoint of loop **C** at 03:51:32 UT.

SOURCE: Author production

Figure 6.38 - Amplitude and phase narrowband maps for travelling waves of 36 seconds in the footpoints of loops **A** and **C**.



(a) and (c) Amplitude (arbitrary units) in footpoints of loops **A** and **C**, respectively observed in 304 Å. (b) and (d) represent the phase (rad) for (a) and (c), respectively.

SOURCE: Author production

6.3 Curve Fitting for Waves Found

We extracted the temporal signal of the waves found, integrating the narrowband maps cube for each period-band (19, 9, 5, 2, 1 min, and 36 s), and we used a curve-fitting method to determine the amplitude, phase, and decay time of the oscillations. We fitted a decaying sine function to the temporal profile of waves that we found.

$$f(t) = A_0 + A \sin\left(\frac{2\pi}{P}t + \delta\right) e^{t/\tau}, \quad (6.1)$$

where t , A , A_0 , P , δ , τ are the time, amplitude, vertical shift, period, phase, and decay time, respectively.

The fitting error is computed as

$$E = \frac{|Signal - Fitting|}{Signal}. \quad (6.2)$$

In Table 6.3 we present the parameters of best fitted functions, with a fitting error of $\approx 5\%$. The decay times $\tau_{19min} \approx 24$ min, $\tau_{9min} \approx 10$ min and $\tau_{5min} \approx 8$ min are in agreement with the values found in the literature and are characteristic of slow magneto-acoustic waves (WANG et al., 2002; WANG et al., 2003b).

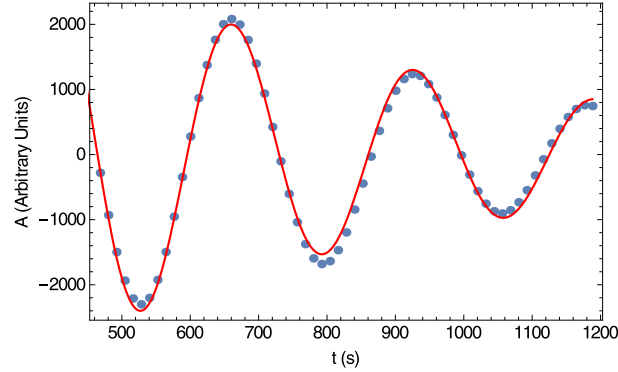
Table 6.3 - Fitting parameters for waves found in NOAA 11272.

Period band (min)	A (10^5) (arb. unit)	A_0 (10^2) (arb. unit)	P (min)	δ (rad)	τ (min)
19 ± 6	1.80	39.80	18.20	3.20	24.10
9 ± 3	1.10	23.30	9.10	3.20	10.80
5 ± 2	0.45	5.44	4.70	3.22	8.09
2 ± 0.8	23.37	10.78	2.08	2.15	3.51
1 ± 0.4	7.30	0.83	1.15	8.34	1.66
0.6 ± 0.2	6.17	6.02	0.57	10.74	4.16

SOURCE: Conde et al. (2016)

In Figure 6.39 we show the best fitted curve (red line) for waves of 5 minutes seen in 94 \AA . These waves were seen closer to footpoint **1** of the loop **C**, during the maximum period of C1.9 class flare, between 02:45:00 UT and 03:23:24 UT. The curve fitted showed a decay time of ≈ 10 minutes.

Figure 6.39 - Best fitted decaying curve



Temporal signal integrated for waves of 19 minutes in 171 \AA (blue points). The red line shows the best fitted curve using the Equation (6.1).

SOURCE: Author production

6.4 Magnetic Field Extrapolation and Waves Velocity

In this section we will show the velocities along the extrapolated field lines, that better match with the loops presented in Figure 6.4. The upper label of Figures 6.4(a)–(f) shows the time in which the loops were better observed and it is related with the flares time mentioned in Table 6.1. Comparing the results of Table 6.1 and Section 6.2 we saw that there is high temporal coincidence between flares and waves found in the active region studied. Hence, we calculated the sound and Alfvén velocities of the extrapolated lines as a function of height.

In order to do this, we chose six magnetograms that coincided temporally with the loops observed in EUV on August 17, 2011. The loops were organized according to the moment in which they appeared during the flares occurred in NOAA 11272. Thus, the selected time was established as:

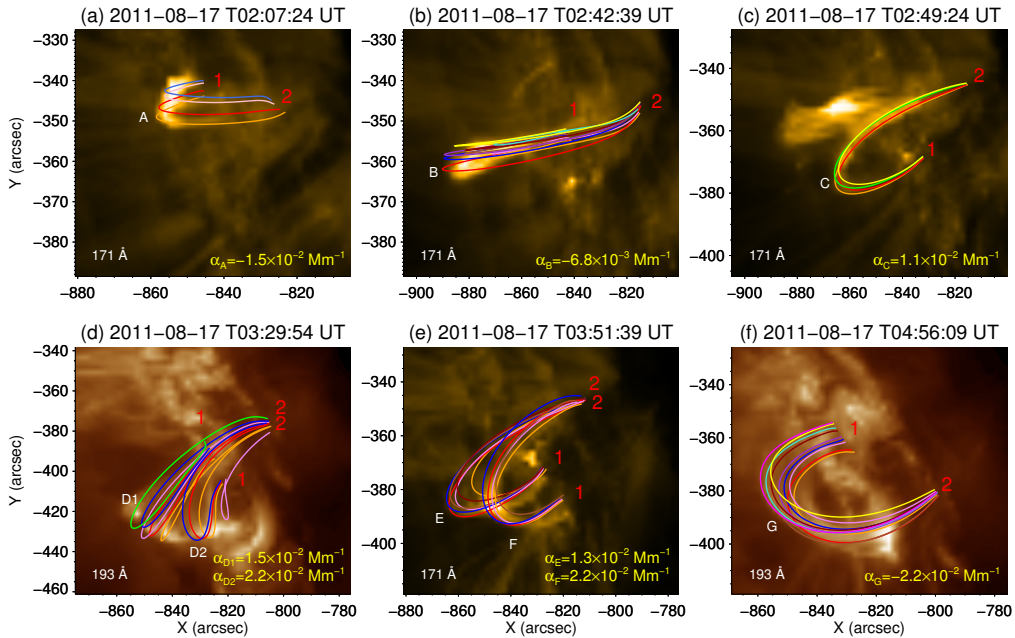
- Loop **A**: 02:07:24 UT
- Loop **B**: 02:42:39 UT
- Loop **C**: 02:49:24 UT
- Loop **D**: 03:29:54 UT
- Loops **E** and **F**: 03:51:39 UT

- Loop **G**: 04:56:09 UT

We processed and aligned the magnetograms as explained in Chapter 3 and extrapolated the magnetic field lines using the linear force free approximation as mentioned in Section 5.1.

In Figures 6.40(a)–(f) we show lines with $\alpha_A = -1.5 \times 10^{-2} \text{ Mm}^{-1}$, $\alpha_B = -6.8 \times 10^{-3} \text{ Mm}^{-1}$, $\alpha_C = 1.1 \times 10^{-2} \text{ Mm}^{-1}$, $\alpha_{D_1} = 1.5 \times 10^{-2} \text{ Mm}^{-1}$, $\alpha_{D_2} = 2.2 \times 10^{-2} \text{ Mm}^{-1}$, $\alpha_E = 1.3 \times 10^{-2} \text{ Mm}^{-1}$, $\alpha_F = 2.2 \times 10^{-2} \text{ Mm}^{-1}$ and $\alpha_G = -2.2 \times 10^{-2} \text{ Mm}^{-1}$, that better match with the loops **A**–**G** showed in Figure 6.4(a)–(f), respectively. In addition, we indicated the footpoint of each loop through of numbers **1** and **2**, which refers to the first and last point of the extrapolated field line. Footpoint position was established according to the α value obtained from the magnetic field extrapolation, i.e., lines with $\alpha > 0$ (**C**–**F**) placed these footpoints contrary to lines with $\alpha < 0$ (**A**, **B**, and **G**).

Figure 6.40 - Magnetic field lines plotted over AIA images.

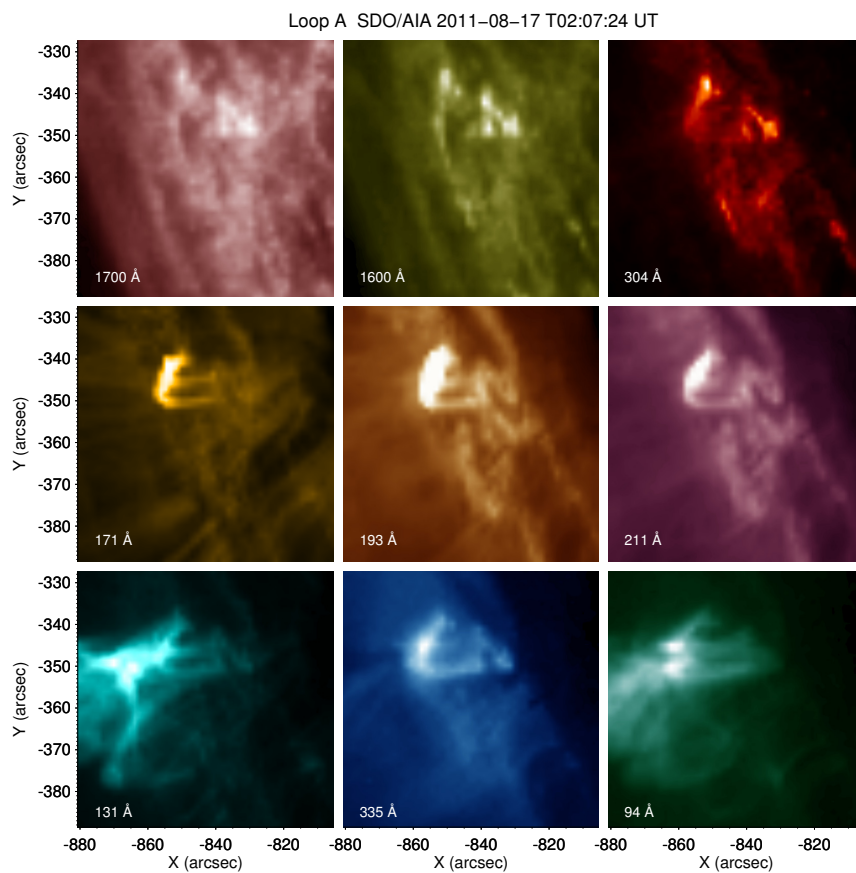


Magnetic field lines that better match with the loops observed in 171 and 193 Å, showed in Figure 6.4. **1** and **2** represent the footpoints of the loops.

SOURCE: Author production

In Figures 6.41, 6.44, 6.47, 6.50, 6.53, and 6.56 we present the loops **A**, **B**, **C**, **D**, **E**, **F**, and **G** seen in nine SDO/AIA band passes (1700, 1600, 304, 171, 193, 211, 131, 335, and 94 Å). The extrapolated field lines that better match with the loops observed in the AIA images can be seen in Figures 6.42, 6.45, 6.48, 6.51, 6.54, and 6.57. In the same manner, Figures 6.43, 6.46, 6.49, 6.52, 6.55, and 6.58 shows these lines over the magnetogram corresponding at the time of each observed loop.

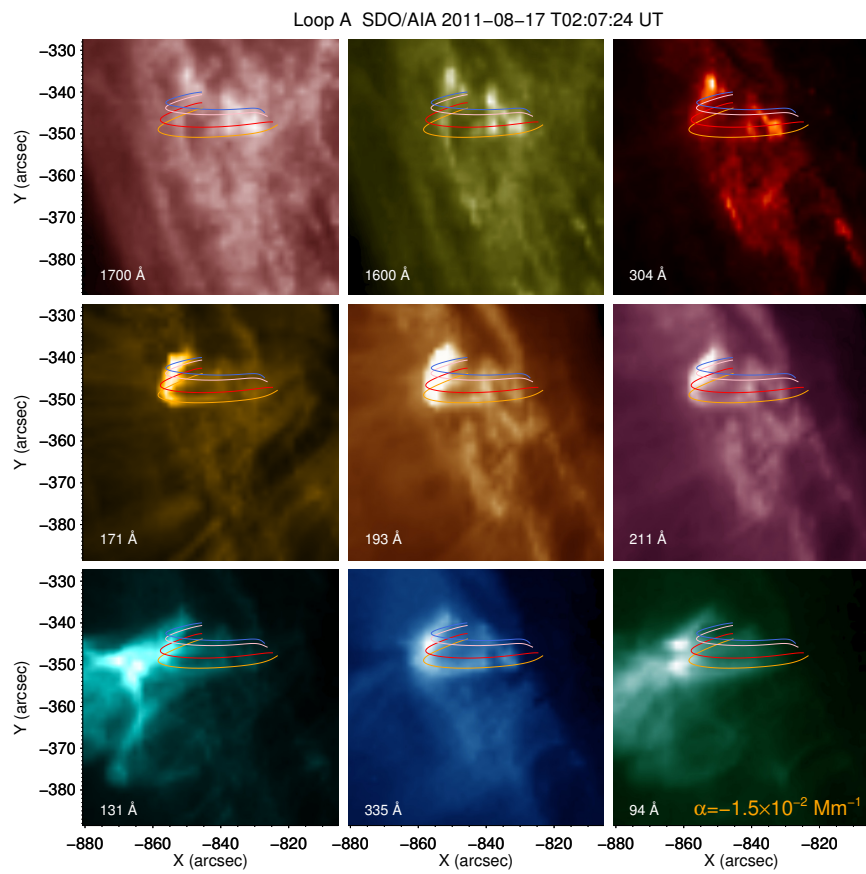
Figure 6.41 - Image of loop **A** obtained by SDO/AIA in nine wavelengths.



Loop **A** is highly defined in 171, 193 and 211 Å. Also it is visible in 131, 335, and 94 Å.

SOURCE: Author production

Figure 6.42 - Magnetic field lines for $\alpha_A = -1.5 \times 10^{-2} \text{ Mm}^{-1}$ over images of SDO/AIA.

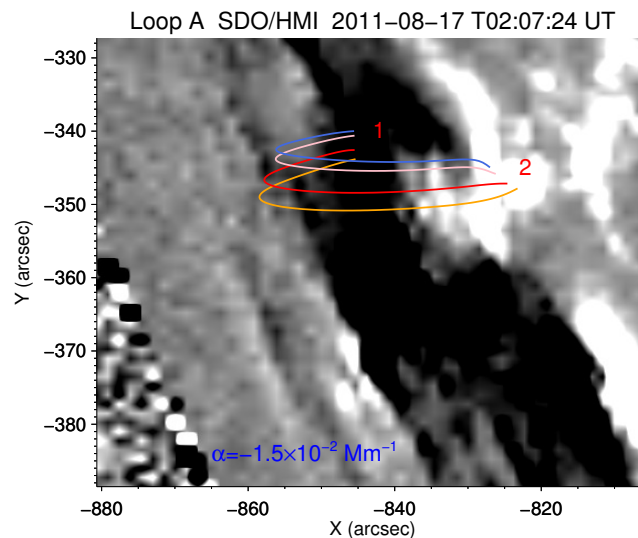


Magnetic field lines reproducing the loop **A** as seen in 171, 193, and 211 Å wavelengths.

SOURCE: Author production

Figure 6.41 shows the loop **A** in nine band passes on 2011-08-17 at 02:07:00 UT. The loop shape is well defined in 171, 193, and 211 Å, however in 131, 335, and 94 Å is high visible but surrounded by hot plasma. We show the extrapolated field lines with $\alpha_A = -1.5 \times 10^{-2} \text{ Mm}^{-1}$ over AIA and HMI images (see Figures 6.42 and 6.43, respectively). These lines match with the loops observed by SDO/AIA, particularly in 171 Å.

Figure 6.43 - Magnetic field lines for $\alpha_A = -1.5 \times 10^{-2} \text{ Mm}^{-1}$ over an image of SDO/HMI.

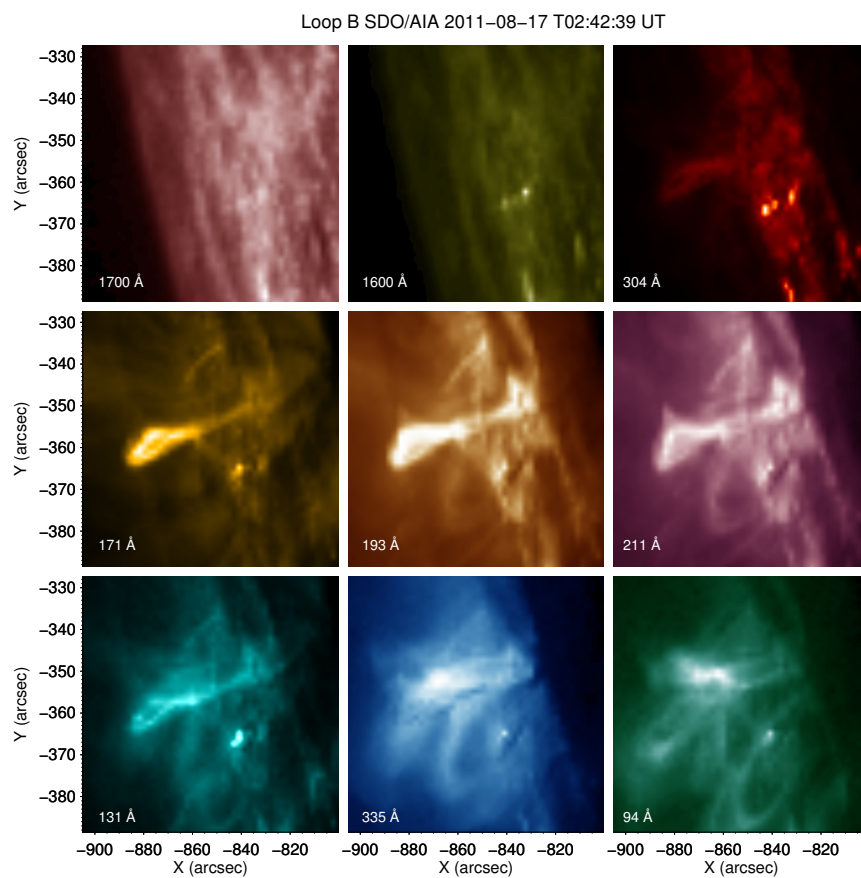


Magnetic field lines plotted over the magnetogram at 02:07:24 UT. **1** and **2** represent the footpoints of the loops.

SOURCE: Author production

Figure 6.44 shows the loop **B** in nine band passes on 2011-08-17 at 02:42:39 UT. The loop shape is well defined in 171, 193, and 211 Å and partially visible in 131 and 304 Å. The loop is not well defined in 335 and 94 Å. We show the extrapolated field lines with $\alpha_B = -6.8 \times 10^{-3} \text{ Mm}^{-1}$ over AIA and HMI images (see Figures 6.45 and 6.46, respectively). These lines match with the loops observed by SDO/AIA, in 171, 193, 211, 304, and 131 Å.

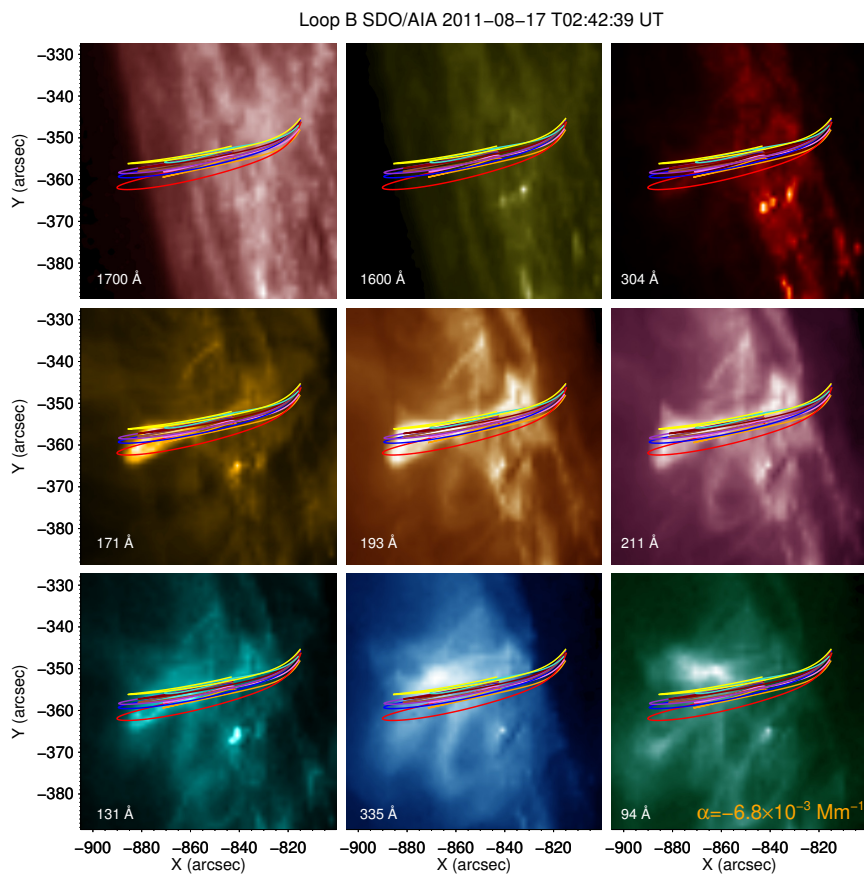
Figure 6.44 - Image of loop **B** obtained by SDO/AIA in nine wavelengths.



Loop **B** is well defined in 171, 193 and 211 Å, but not in 335, and 94 Å. The loop is partially visible in 131 and 304 Å.

SOURCE: Author production

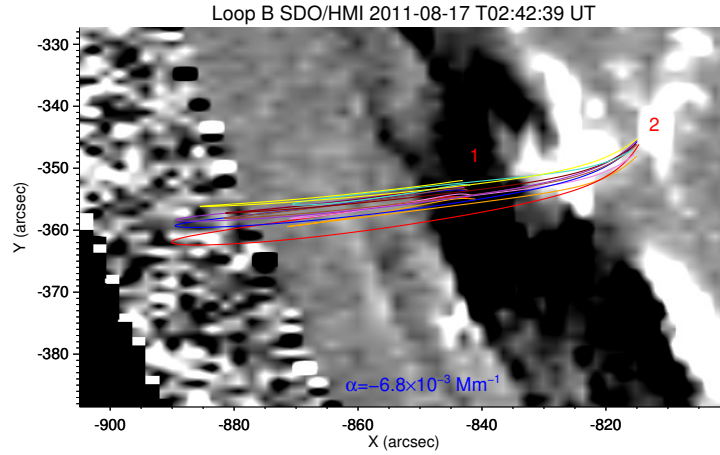
Figure 6.45 - Magnetic field lines for $\alpha_B = -6.8 \times 10^{-3} \text{ Mm}^{-1}$ over images of SDO/AIA.



Magnetic field lines reproducing the loop **B** as seen in 171, 193, 211, 304, and 131 Å wavelengths.

SOURCE: Author production

Figure 6.46 - Magnetic field lines for $\alpha_B = -6.8 \times 10^{-3} \text{ Mm}^{-1}$ over an image of SDO/HMI.

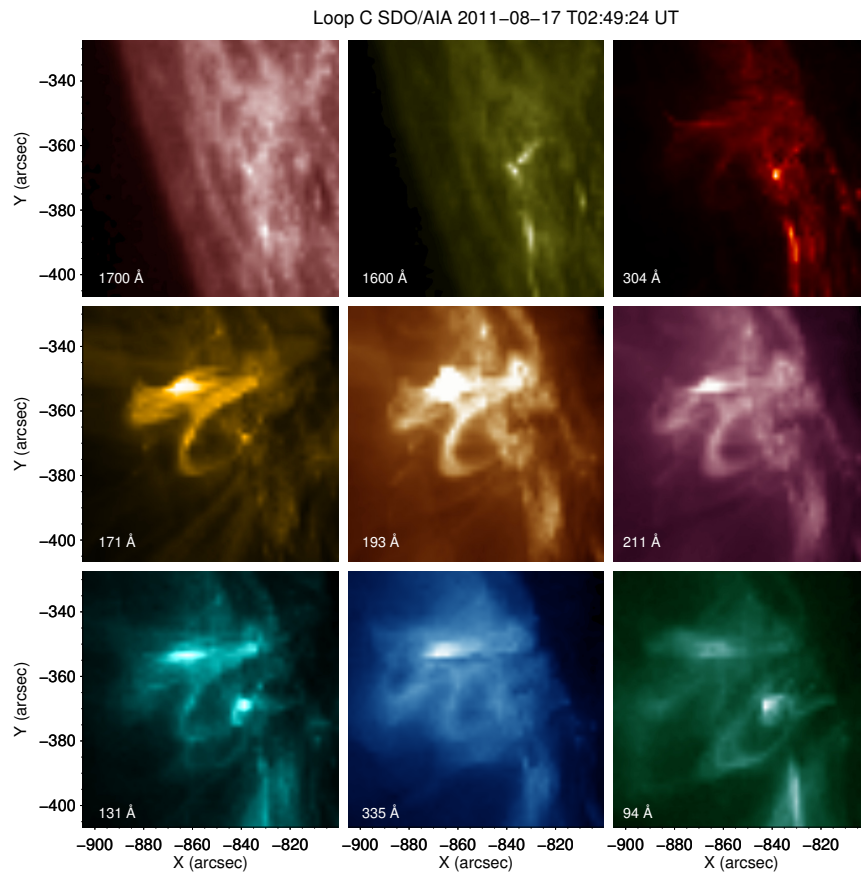


Magnetic field lines plotted over the magnetogram at 02:42:39 UT. **1** and **2** represent the footpoints of the loops.

SOURCE: Author production

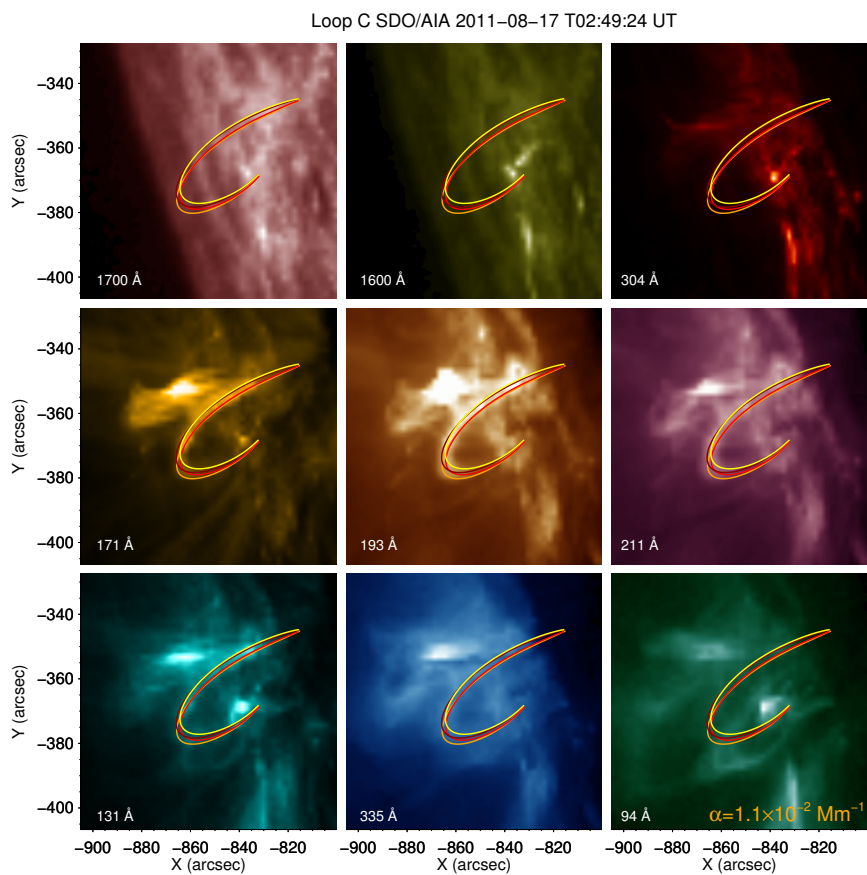
Figure 6.47 shows the loop **C** in nine band passes on 2011-08-17 at 02:49:24 UT. The loop shape is well defined in 171, 193, 211, and 131 Å and it is partially visible in 94 Å. We show the extrapolated field lines with $\alpha_C = 1.1 \times 10^{-2} \text{ Mm}^{-1}$ over AIA and HMI images (see Figures 6.48 and 6.49, respectively). Note that these lines match with the loops observed by SDO/AIA, in 171, 193, 211, and 131 Å.

Figure 6.47 - Image of loop C obtained by SDO/AIA in nine wavelengths.



Loop C is well defined in 171, 193, 211, and 131 Å
SOURCE: Author production

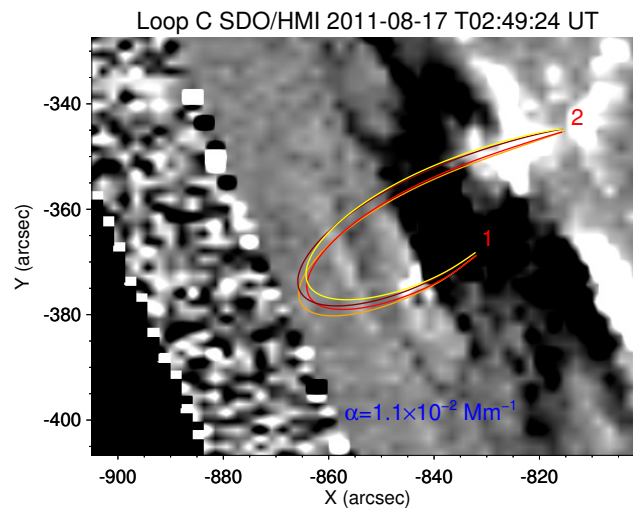
Figure 6.48 - Magnetic field lines for $\alpha_C=1.1\times 10^{-2} \text{ Mm}^{-1}$ over images of SDO/AIA.



Magnetic field lines reproducing the loop **C** as seen in 171, 193, 211, and 131 Å wavelengths.

SOURCE: Author production

Figure 6.49 - Magnetic field lines for $\alpha_C=1.1\times 10^{-2} \text{ Mm}^{-1}$ over an image of SDO/HMI.

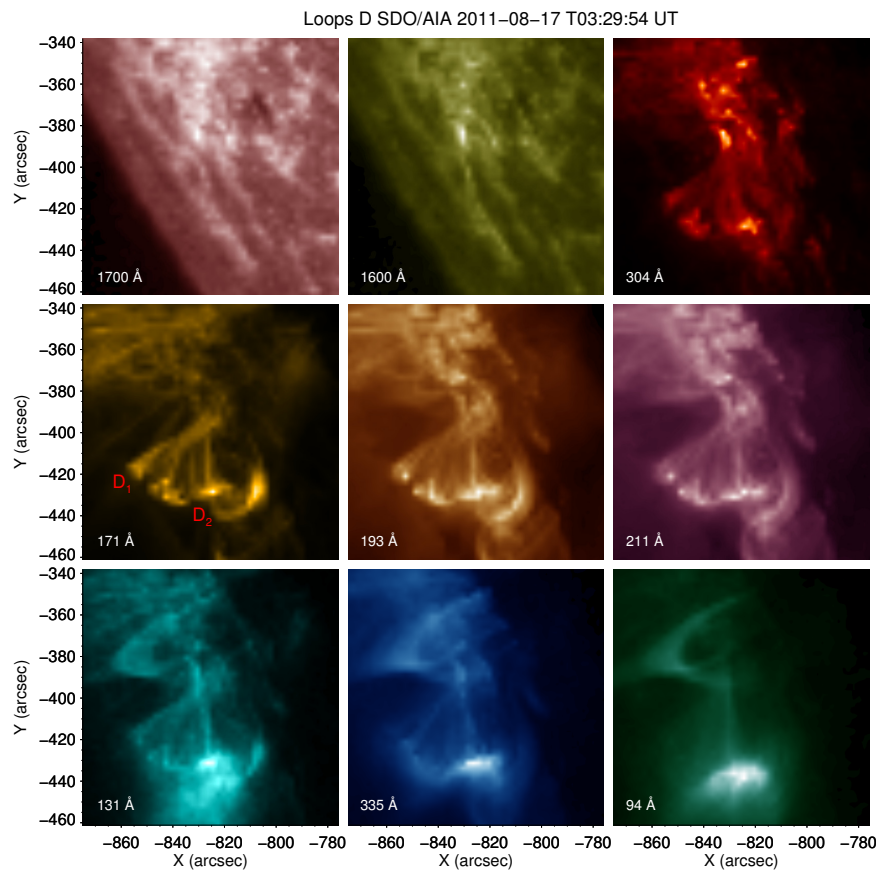


Magnetic field lines plotted over the magnetogram at 02:49:24 UT. **1** and **2** represent the footpoints of the loops.

SOURCE: Author production

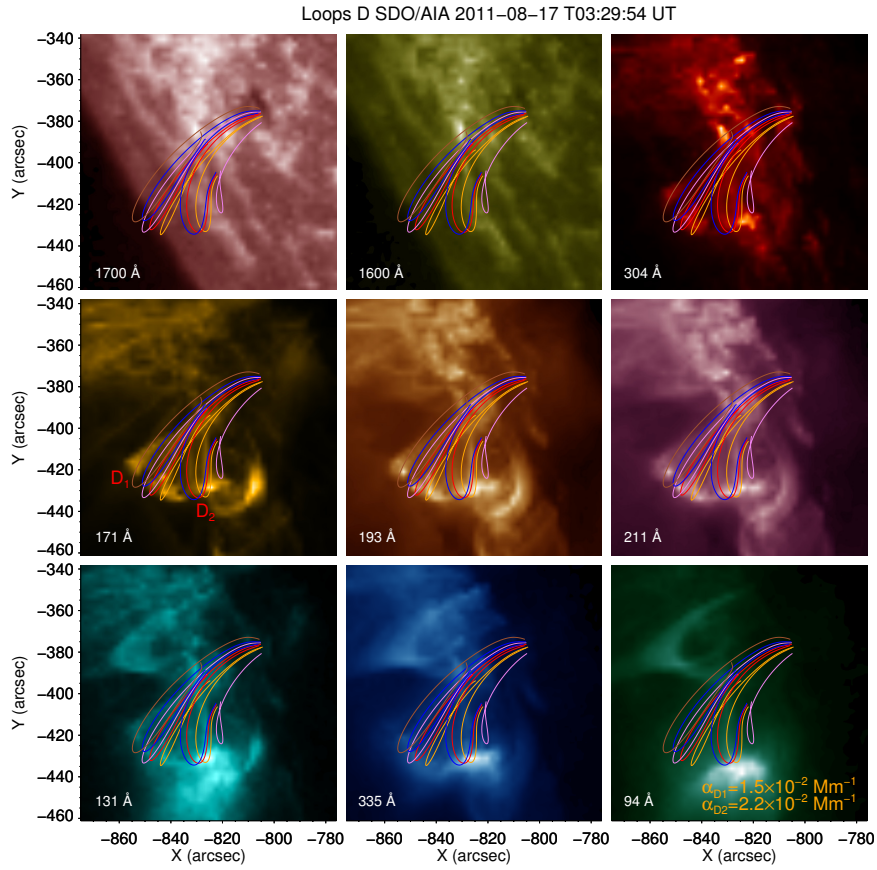
Figure 6.50 shows the loops **D** in nine band passes on 2011-08-17 at 03:29:54 UT. We observed the loops in all band passes except in 1700 and 1600 Å. We show the extrapolated field lines with $\alpha_{D_1} = 1.5 \times 10^{-2} \text{ Mm}^{-1}$ and $\alpha_{D_2} = 2.2 \times 10^{-2} \text{ Mm}^{-1}$ over AIA and HMI images (see Figures 6.51 and 6.52, respectively). These lines match with the loops observed by SDO/AIA in all EUV band passes.

Figure 6.50 - Image of loop **D** obtained by SDO/AIA in nine wavelengths.



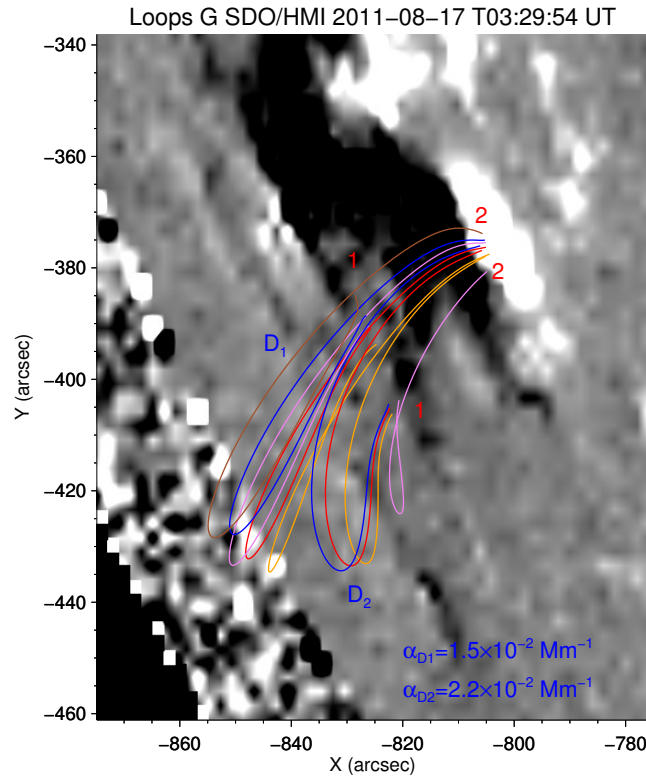
Loops **D** were seen in all wavelengths except in 1700 and 1600 Å.
SOURCE: Author production

Figure 6.51 - Magnetic field lines for $\alpha_{D_1}=1.5\times 10^{-2} \text{ Mm}^{-1}$ and $\alpha_{D_2}=2.2\times 10^{-2} \text{ Mm}^{-1}$ over images of SDO/AIA.



Magnetic field lines reproducing the loop **D** as seen in EUV band passes.
 SOURCE: Author production

Figure 6.52 - Magnetic field lines for $\alpha_{D_1}=1.5\times 10^{-2} \text{ Mm}^{-1}$ and $\alpha_{D_2}=2.2\times 10^{-2} \text{ Mm}^{-1}$ over an image of SDO/HMI.

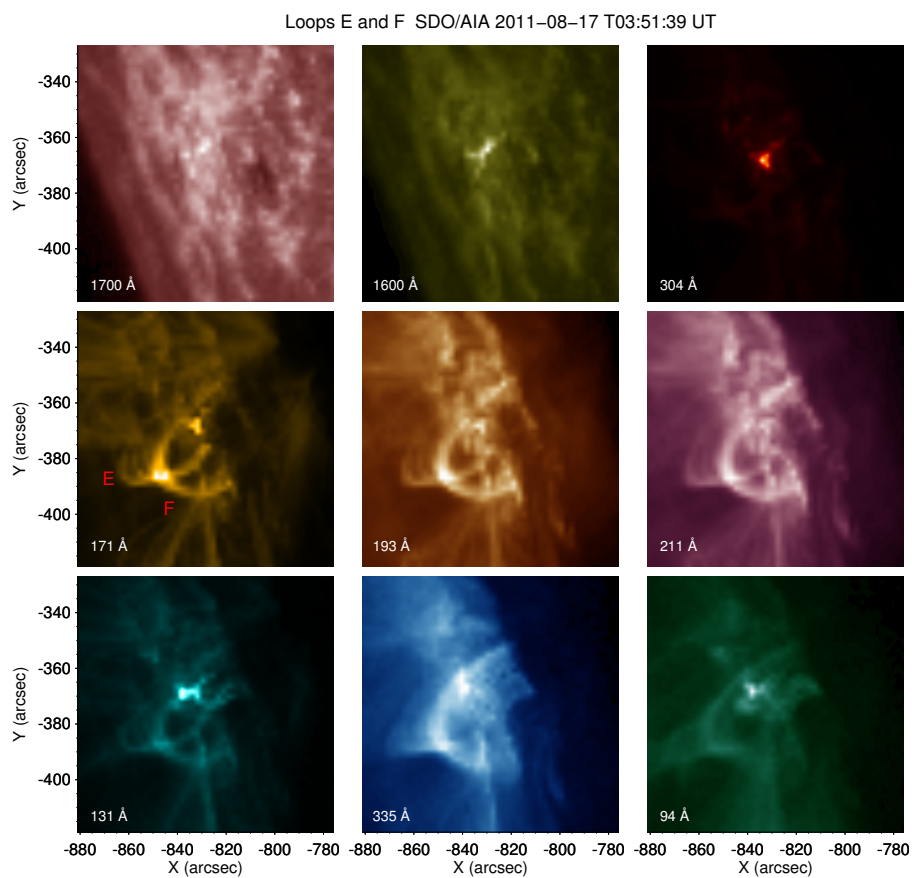


Magnetic field lines that reproduce the loop **D** seen in EUV images, plotted over the magnetogram at 03:29:54.80 UT. **1** and **2** represent the footpoints of the loops.

SOURCE: Author production

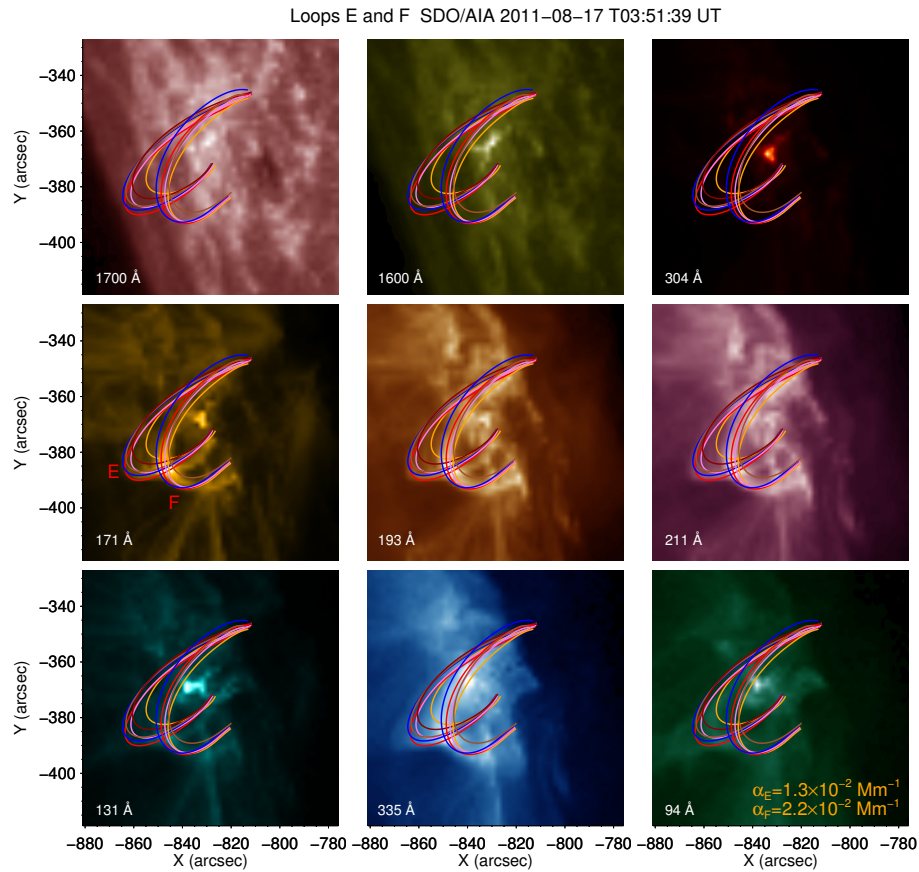
Figure 6.53 shows the loops **E** and **F** in nine band passes on 2011-08-17 at 03:51:36 UT. The loops shape is well defined in 171, 193, 211, and 131 Å and it is diffuse in 335 and 94 Å. Footpoint **1** of the loop **C** is clearly visible in 304 Å. We show the extrapolated field lines with $\alpha_E = 1.3 \times 10^{-2} \text{ Mm}^{-1}$ and $\alpha_F = 2.2 \times 10^{-2} \text{ Mm}^{-1}$ (see Figures 6.54 and 6.55, respectively). Note that these lines match with the loops observed by SDO/AIA, in 171, 193, 211, and 131 Å.

Figure 6.53 - Image of loops **E** and **F** obtained by SDO/AIA in nine wavelengths.



Loops **E** and **F** are well defined in 171, 193, 211, and 131 Å
SOURCE: Author production

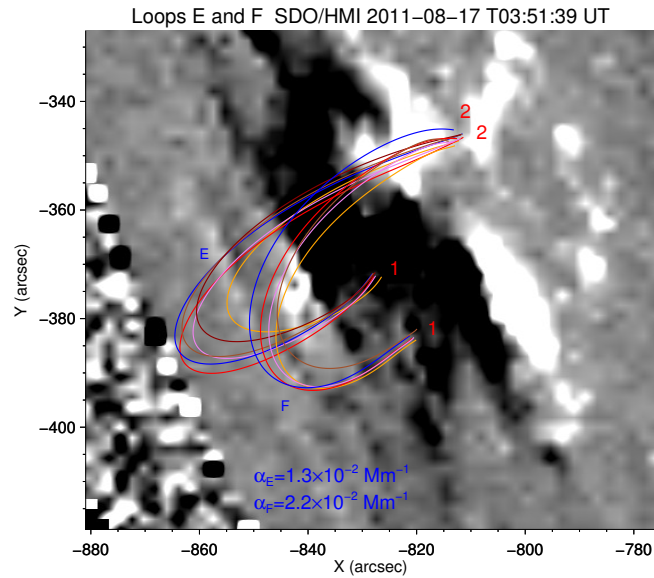
Figure 6.54 - Magnetic field lines for $\alpha_E=1.3\times 10^{-2} \text{ Mm}^{-1}$ and $\alpha_F=2.2\times 10^{-2} \text{ Mm}^{-1}$ over images of SDO/AIA.



Magnetic field lines reproducing the loops **E** and **F** as seen in 171, 193, 211, and 131 Å wavelengths.

SOURCE: Author production

Figure 6.55 - Magnetic field lines for $\alpha_E=1.3\times 10^{-2} \text{ Mm}^{-1}$ and $\alpha_F=2.2\times 10^{-2} \text{ Mm}^{-1}$ over an image of SDO/HMI.



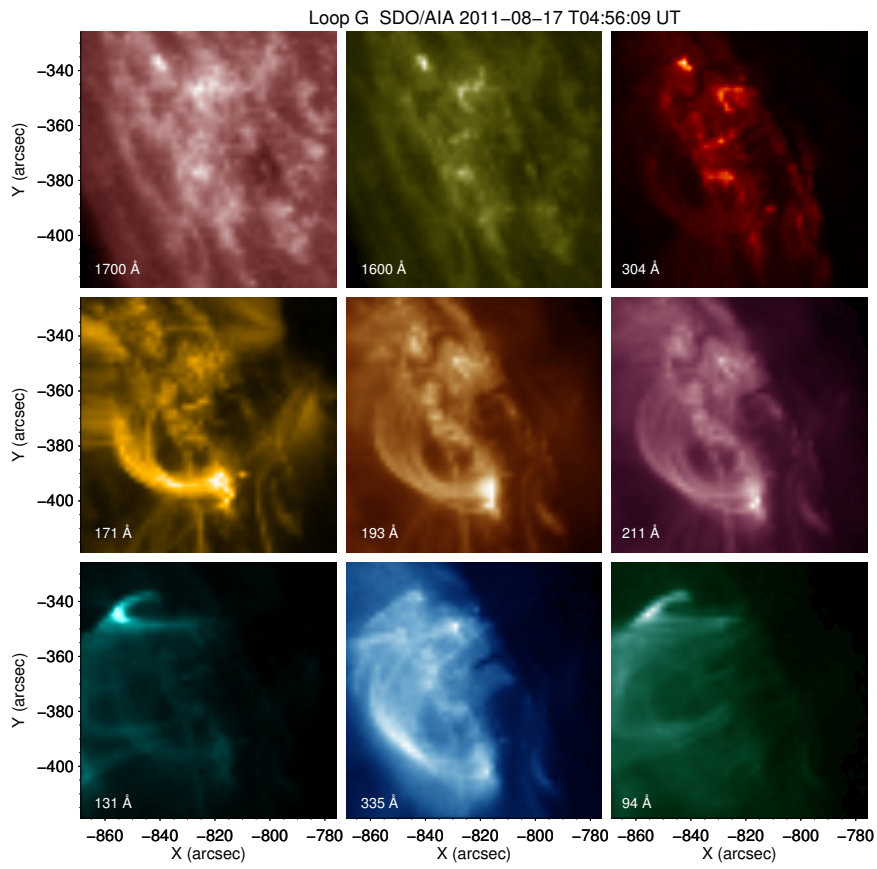
Magnetic field lines that reproduce the loops **E** and **F** seen in EUV images, plotted over the magnetogram at 03:51:39.80 UT. **1** and **2** represent the footpoints of the loops.

SOURCE: Author production

Figure 6.56 shows the loop **G** in nine band passes on 2011-08-17 at 04:56:09 UT. The loop shape is well defined in 171, 193, 211, and 335 Å, partially visible in 304 Å and diffuse in 131 Å.

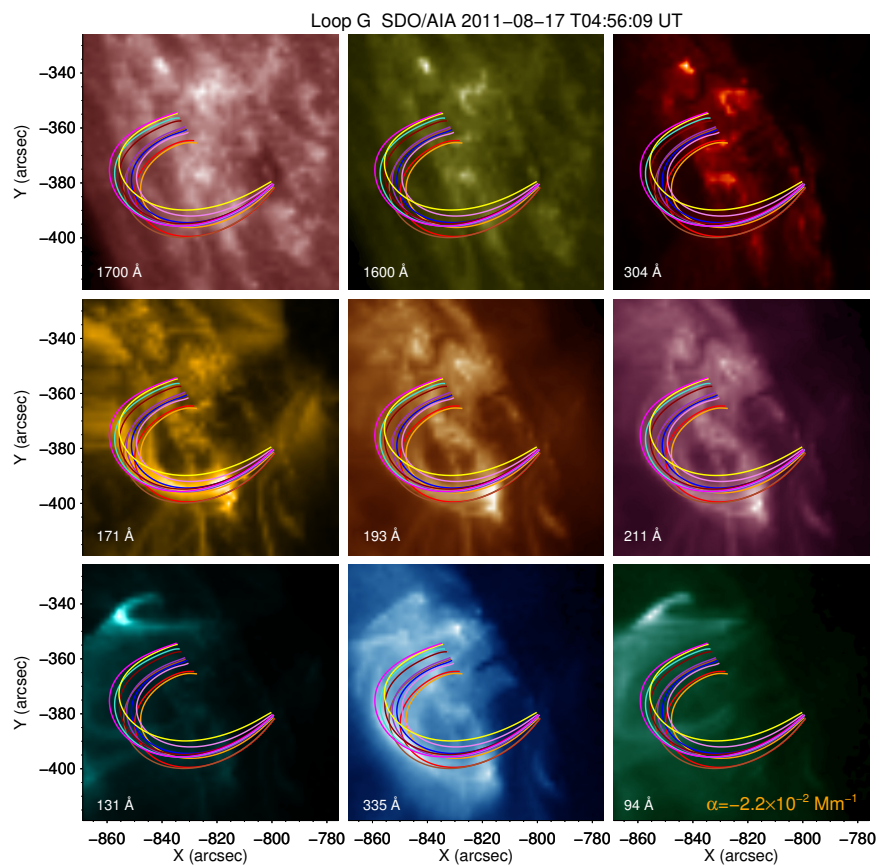
We show the extrapolated field lines with $\alpha_G = -2.2 \times 10^{-2} \text{ Mm}^{-1}$ (see Figure 6.57 and 6.58, respectively). These lines match with the loops observed by SDO/AIA, in 171, 193, 211, and 335 Å.

Figure 6.56 - Image of loop **G** obtained by SDO/AIA in nine wavelengths.



Loop **G** is well defined in 171, 193, 211, and 335 Å
SOURCE: Author production

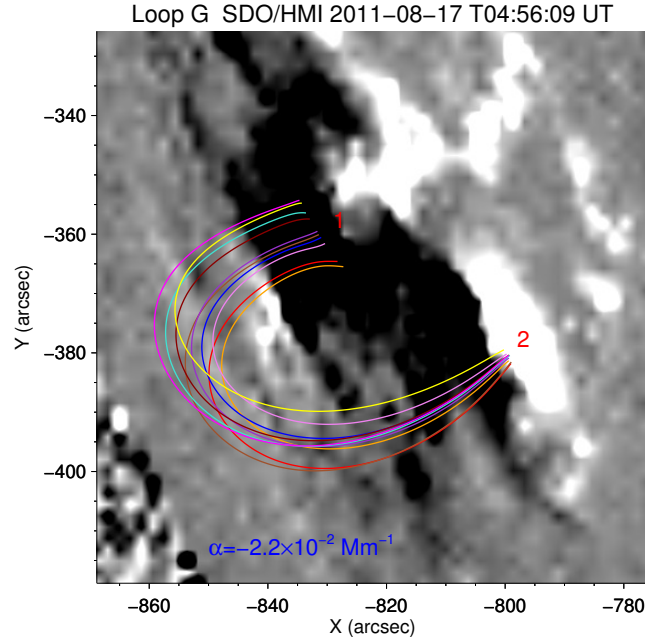
Figure 6.57 - Magnetic field lines for $\alpha_G = -2.2 \times 10^{-2} \text{ Mm}^{-1}$ over images of SDO/AIA.



Magnetic field lines reproducing the loop **G** as seen in 171, 193, 211, and 335 Å wavelengths.

SOURCE: Author production

Figure 6.58 - Magnetic field lines for $\alpha_G = -2.2 \times 10^{-2} \text{ Mm}^{-1}$ over an image of SDO/HMI.



Magnetic field lines plotted over the magnetogram at 04:56:09.80 UT. **1** and **2** represent the footpoints of the loops.

SOURCE: Author production

In Table 6.4 we present the most important characteristics of extrapolated field lines.

Table 6.4 - Length L (Mm), height h (km) and magnetic field B (G) of extrapolated field lines.

Loop name	α (Mm^{-1})	h_{max} (km)	L (Mm)	B (G)
A	-1.5×10^{-2}	20591.4	34 - 70	46.21 - 465.76
B	-6.8×10^{-3}	49059.0	60 - 136	11.41 - 457.03
C	1.1×10^{-2}	41549.6	76 - 116	17.16 - 492.11
D1	1.5×10^{-2}	44869.2	115 - 141	13.51 - 715.63
D2	2.2×10^{-2}	37552.9	80 - 135	21.93 - 962.95
E	1.3×10^{-2}	39101.2	73 - 110	20.17 - 404.07
F	2.2×10^{-2}	29639.5	77 - 91	34.47 - 318.49
G	-2.2×10^{-2}	37384.7	81 - 114	20.19 - 818.14

SOURCE: Author production

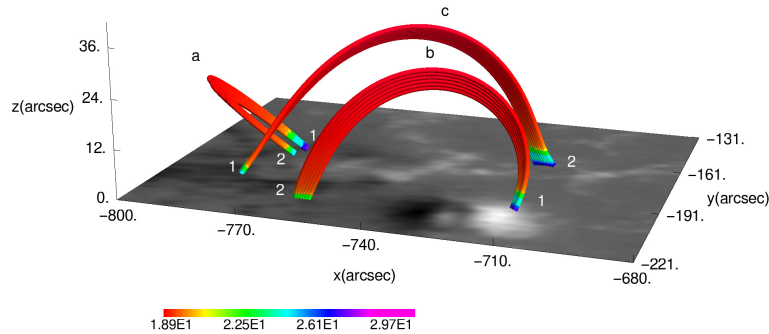
6.4.1 Waves Velocity

The extrapolated field lines showed height values less than 50 Mm. Then, according to the structure model explained in Section 5.3 we obtained the density and temperature distributions for the loops **A–F**, and with this we calculated the sound c_s and Alfvén v_A velocities.

For plotting our results, we divided the loops in two groups. One group contains the loops **A**, **B**, and **C**, which were seen during the C1.9 flare and the other group contains the loops **D**, **E**, **F**, and **G**, observed after C1.9 and during the C2.3 flare. Thus, we select the LOS magnetograms at 02:42:39 UT and 03:51:39 UT for plotting the lines. Next, moved them to the solar disk's centre and re-sampled to plot the modelled loops.

We obtained number density values between $n \approx 10^{17} \text{ cm}^{-3}$ (loop footpoints) and $n \approx 10^7 \text{ cm}^{-3}$ (loop apex). As an example, in Figure 6.59 we show the logarithm of the number density distribution $n \text{ (cm}^{-3}\text{)}$ as a function of height $h \text{ (km)}$, for loops **A**, **B**, and **C**.

Figure 6.59 - Logarithm of the number density along the loops **A–C**.

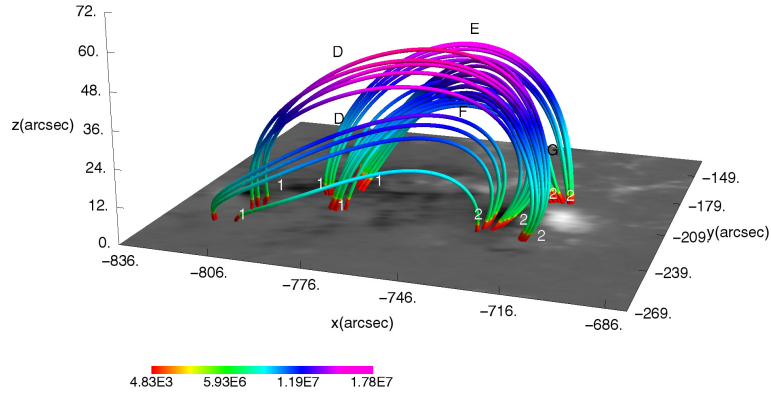


Logarithm of the number density $\log(n) \text{ (cm}^{-3}\text{)}$ distribution as a function of the extrapolated field lines' height. Footpoints **1** and **2** are indicated for all loops.

SOURCE: Conde et al. (2016)

We found temperatures of $\approx 10^3$ (K) to reach values of $T \approx 18$ MK. Loops **A**, **D1**, and **E** had higher temperature values. As an example, Figure 6.60 shows the temperature distribution T (K) as a function of height h (km) along the loops **D–G**.

Figure 6.60 - Temperature distribution along the loops **D–G**.



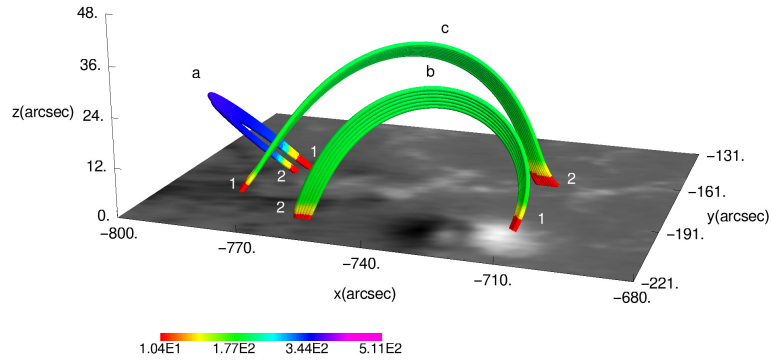
Temperature distribution T (K) as a function of the extrapolated field lines' height. Footpoints **1** and **2** are indicated for all loops.

SOURCE: Author production

We used the obtained temperature values to calculate the sound velocity as a function of height, for the extrapolated field lines **A–G**. We found $c_{s_{max}} \approx 344$ km s⁻¹ for loop **A**, which is compatible with the established c_s value for 94 Å given in Table 5.1. In the same manner, loops **D1** and **E** reached $c_{s_{max}} \approx 638$ km s⁻¹, that are in agreement with the c_s value for 193 Å given in Table 5.1.

Figure 6.61 shows the acoustic velocity distribution along the loops **A**, **B**, and **C**. The maximum value of sound velocity correspond to the loop apex, in which also were seen the higher temperature values. Loop **A**, where the C1.9 flare started, shows an high velocity value compared with loops **B** and **C**. On the other hand, in Figure 6.62 we present the c_s distribution for loops **D–G**. Higher values were seen in loop **E** which was perturbed after C1.9 and during C2.3 flares.

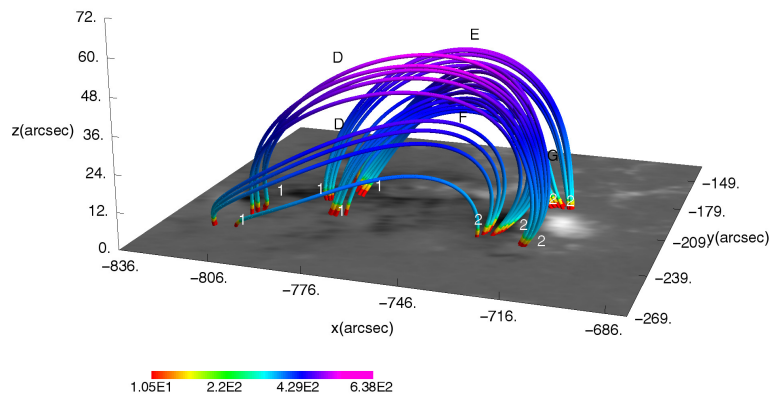
Figure 6.61 - Sound velocity c_s along the loops **A–C**.



Sound velocity c_s (km s^{-1}) as a function of height h (km) for loops **A**, **B** and **C**. Footpoints **1** and **2** are indicated for all loops.

SOURCE: Conde et al. (2016)

Figure 6.62 - Sound velocity c_s along the loops **D–G**.



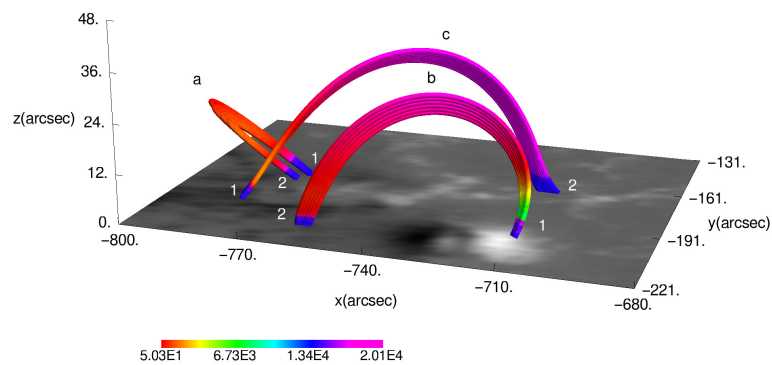
Sound velocity c_s (km s^{-1}) for loops **D**, **E**, **F** and **G**. Footpoints **1** and **2** are indicated for all loops.

SOURCE: Author production

We made a 3D model for Alfvén velocity using the magnetic field values directly from the extrapolated lines. We also used the density values obtained from the structure models, which were presented in Figure 6.59. We obtained $v_A > 10000 \text{ km s}^{-1}$ for heights where $B \approx 100\text{--}300 \text{ G}$ and $n \approx 10^8 \text{ cm}^{-3}$. These values are in agreement with reported studies in the literature (BROSIUS et al., 1992; SCHMELZ et al., 1992; SCHMELZ et al., 1994).

We also found that the magnetic field distribution was not symmetric ($B_2 < B_1$ or contrary) along the loops. This was reflected in the Alfvén velocity distribution ($v_{a2} < v_{a1}$). We also saw that the maximum value of B and v_A are inclined towards one loop leg and it coincides with the bright distribution along the loops.

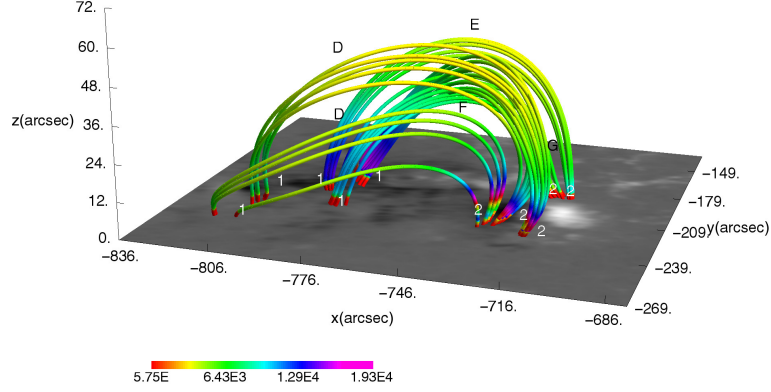
Figure 6.63 - Alfvén velocity v_a along the loops **A–C**.



Alfvén velocity v_a (km s^{-1}) along the loops **A**, **B** and **C**. Footpoints **1** and **2** are indicated for all loops.

SOURCE: Conde et al. (2016)

Figure 6.64 - Alfvén velocity v_a along the loops **D–G**.



Alfvén velocity v_a (km s^{-1}) along the loops **D–G**. Footpoints **1** and **2** are indicated for all loops.

SOURCE: Author production

Comparing the sound and Alfvén velocities distributions we found fast magneto-acoustic waves ($v_A > c_s$) in the loops **B**, **C**, **E**, **F**, and **G**, and in the footpoint of the loops **A** and **D**. In addition, we observed slow magneto-acoustic waves ($v_A < c_s$) at the loop apex **A** and we saw the intermediate mode for loop apex **D** ($v_A \approx c_s$).

Table 6.5 - Phase velocity v_{ph} for 0.6-, 1- and 2-minute waves.

Loop	L (Mm)	v_{ph} 36-s (km s^{-1})	v_{ph} 1-min (km s^{-1})	v_{ph} 2-min (km s^{-1})
Footpoint of loop A	34 - 70	2827 - 3479	1696 - 2087	848 - 1043
B	60 - 136	2368 - 7467	1421 - 4480	710 - 2240
C	76 - 116	1831 - 5606	1098 - 3363	549 - 1681
Footpoint of loop D1	115 - 141	2490 - 7708	1494 - 4625	747 - 2312
Footpoint of loop D2	80 - 135	1736 - 6258	1041 - 3755	520 - 1877
E	73 - 110	4929 - 6138	2957 - 3682	1478 - 1841
F	77 - 91	1394 - 5074	836 - 3044	418 - 1522
G	81 - 114	2053 - 6089	1232 - 3653	616 - 1826

SOURCE: Author production

Table 6.6 - Phase velocity v_{ph} for 5-, 9- and 19-minute waves.

Loop	L (Mm)	v_{ph} 5-min (km s ⁻¹)	v_{ph} 9-min (km s ⁻¹)	v_{ph} 19-min (km s ⁻¹)
A	34 - 70	339 - 417	188 - 231	89 - 109
B	60 - 136	284 - 896	157 - 497	74 - 235
C	76 - 116	219 - 672	122 - 373	57 - 177
D1	115 - 141	298 - 925	166 - 513	78 - 243
D2	80 - 135	208 - 751	115 - 417	54 - 197
E	73 - 110	591 - 736	328 - 409	155 - 193
F	77 - 91	167 - 608	92 - 338	44 - 160
G	81 - 114	246 - 730	136 - 405	64 - 192

SOURCE: Author production

From Equation (2.28) we calculated the phase velocity v_{ph} of waves for each period found. According to v_{ph} values we determined that the fast magneto-acoustic waves corresponding to lower periods, i.e., 36-second, 1- and 2-minute period-band (see Table 6.5), and the slow magneto-acoustic waves to higher periods, i.e., 5-, 9-, and 19-minute (see Table 6.6). These results are in a good agreement with fast (WILLIAMS et al., 2002) and slow (WANG et al., 2003b) modes observed in coronal loops.

7 CONCLUSIONS AND FINAL REMARKS

We analysed the active region NOAA 11272 during six hours in which occurred B and C class flares. In this time period, we observed seven loops (**A**, **B**, **C**, **D**, **E**, **F**, and **G**) being sequentially perturbed since the first flare (B3.8). These loops were clearly visible in all EUV wavelengths of SDO/AIA. The time profiles for the nine AIA band passes showed the moments in which the flares occurred.

Through the PWF method (SYCH; NAKARIAKOV, 2008), we found standing waves in the period-band of 5, 9, and 19 minutes. Waves of 9 and 19 minutes were seen along the loops **A**–**G** in all EUV wavelengths. 5-minute waves were not seen in loops **E** and **F**, but interestingly they were observed between the footpoints of the loops **A** and **C** when C1.9 flare started, and in the footpoint **1** of loop **C** when the same flare ended.

In the same manner, we found travelling waves in the period-bands of 2, 1, and 0.6 minutes. We observed waves of 2 and 1 minutes moving between footpoint regions of the loops **A** and **C** during the B3.8 class flare, in 1700, 1600 and 304 Å principally. 36-seconds (0.6 min) waves were seen in loops **A** and **C** during the B3.8 and C2.3 flares respectively.

One important aspect refers to high frequency waves moving from **A** to **C**. These waves started in loop **A** and before B3.8 class flare. It is very likely, that the waves found in loop **A** triggered the flare. However, also is possible that the loop **A** had been perturbed by the flare and successively the loops **B** and **C**. Similarly, the high frequency waves found on footpoint **1** of loop **C** may be responsible by the perturbation of the loops **E** and **F**.

We found the decay time $\tau \sim 1 - 24$ minutes, fitting a decaying sine function to the time profile of the waves found. Decay time for 5-, 9-, and 19-minute standing waves are in agreement with values found in the literature for slow magneto-acoustic waves (WANG *et al.*, 2002; WANG *et al.*, 2003b). It could be interesting to extend the analysis of these waves to estimate the dissipated energy in the region and to determine if these waves can be the source to trigger the flares studied here. In the same manner, we could calculate the dissipative coefficients for determining the mechanism responsible for damping wave, i.e., conductivity, viscosity, etc.

Using the LFFF approximation we obtained the magnetic field lines that better match with the loops observed in EUV, in such manner that we reproduced the 3D

geometry of the loop. Thus, we proposed to analyse the plasma physical behaviour as a function of line height and not as a function of line length as before models did, e.g., Anfinogentov et al. (2013).

We made a 3D model for describing the temperature, number density and velocities along the loops. In order to do this, we used the coordinates (x, y, z) and magnetic values obtained directly from extrapolated field lines. In addition we used structure models for flares regions (MACHADO et al., 1980) and quiet sun (AVRETT; LOESER, 2008) to find the density distribution as a function of the height. With these values we calculated the Alfvén velocity (v_A) for all loops. In a similar form we put together the structure model for flare region with SSW routines (ASCHWANDEN et al., 2013) to obtain the temperature distribution and calculate the sound velocity (c_s) as a function of the height.

We got extrapolated lines with an $h_{max} = 50$ Mm and from the 3D model we found density and temperature values of $n \approx 10^7 - 10^{17} \text{ cm}^{-3}$ and $T \approx 10^3 - 10^7 \text{ K}$, respectively. Then, we obtained sound velocity values of $c_s \approx 10^2 \text{ km s}^{-1}$ which were consistent with the expected values given in Table 5.1.

On the other hand, the magnetic field distribution along the line was not symmetric and this was reflected in the Alfvén velocity distribution. Hence, the v_A maximum values were in one leg of the loop and not in its apex. In some line points we found $v_A \approx 3 \times 10^4 \text{ km s}^{-1}$ which is in agreement with the literature (BROSIUS et al., 1992; SCHMELZ et al., 1992; SCHMELZ et al., 1994). We also found a high spatial coincidence between the waveform and the bright distribution along the loops studied, particularly for standing waves.

We found slow magneto-acoustic waves at the loop apex **A** and fast mode in the other loops except in **D** where we found the intermediate mode. The slow mode corresponds to lower frequencies, i.e., period-bands of 5, 9, and 19 minutes, while the fast mode to higher frequencies, i.e., period-bands of 0.6, 1 and 2 minutes. These results were established through the decay time τ and calculating the phase velocity as a function of loop length.

The standing waves detected during the C1.9 class flare, principally in loop **A**, may be related with QPP of long periods (NAKARIAKOV; MELNIKOV, 2009). It is possible to do the same appreciation for travelling waves between loops **A** and **C** during the B3.8 and C1.9 flares, but for QPP of high periods. For determining the relation between the QPP and the magneto-acoustic waves found, it is necessary to analyse

the same region in additional wavelengths and modulation depths for each time signal. This could be done in a future work.

Our 3D model represents an unprecedented method to analyse waves in coronal loop, because the most studies are made in 2D or considering only the loop length. In fact, we can extend our model considering magneto-gravity waves because we obtain the values as a function of height and hence we could consider the gravity effects in each loop point.

Also in a future work, we could study with more detail the influence of the Sun geometry in the field lines extrapolation. We could compare these results with observations from STEREO and with the VCA-NLFFF code.

Finally, it is worthwhile to mention that energy dissipation by MHD waves in null points has been an interesting topic for the flares physic study. One reconnection point was observed when the C2.3 flare started (SU et al., 2013). This region involve the loops **E**, **F**, and **G**. We are looking the field lines that reproduce the reconnection point, to study the wave behaviour along these lines and to determine if there is energy dissipation contributing to electron acceleration in this region.

REFERENCES

- AMARI, T.; ALY, J. J.; LUCIANI, J. F.; BOULMEZAOUD, T. Z.; MIKIC, Z. Reconstructing the solar coronal magnetic field as a force-free magnetic field. **Solar Physics**, v. 174, n. 1, p. 129–149, 1997. ISSN 1573-093X. Available from: <<http://dx.doi.org/10.1023/A:1004966830232>>. 40
- AMARI, T.; BOULMEZAOUD, T. Z.; MIKIC, Z. An iterative method for the reconstruction of the solar coronal magnetic field. I. Method for regular solutions. **Astronomy and Astrophysics**, v. 350, p. 1051–1059, oct 1999. 40
- ANFINOGENTOV, S.; NISTICÒ, G.; NAKARIAKOV, V. M. Decay-less kink oscillations in coronal loops. **Astronomy and Astrophysics**, v. 560, p. A107, dec. 2013. 2, 42, 43, 108
- ASCHWANDEN, M. J. **Physics of the Solar Corona**: An introduction. [S.l.]: Praxis Publishing Ltd, 2004. 1, 6, 10, 11, 37
- _____. 2D feature recognition and 3D reconstruction in solar EUV images. **Solar Physics**, v. 228, p. 339–358, may 2005. 42
- _____. The vertical-current approximation nonlinear force-free field code. description, performance tests, and measurements of magnetic energies dissipated in solar flares. **Astrophysical Journal Supplement Series**, v. 224, p. 25, jun. 2016. 42
- ASCHWANDEN, M. J.; BOERNER, P.; SCHRIJVER, C. J.; MALANUSHENKO, A. Automated temperature and emission measure analysis of coronal loops and active regions observed with the Atmospheric Imaging Assembly on the Solar Dynamics Observatory (SDO/AIA). **Solar Physics**, v. 283, n. 1, p. 5–30, 2013. ISSN 1573-093X. Available from: <<http://dx.doi.org/10.1007/s11207-011-9876-5>>. 2, 43, 108
- ASCHWANDEN, M. J.; LEE, J. K.; GARY, G. A.; SMITH, M.; INHESTER, B. Comparison of five numerical codes for automated tracing of coronal loops. **Solar Physics**, v. 248, p. 359–377, apr. 2008. 42
- ASCHWANDEN, M. J.; NEWMARK, J. S.; DELABOUDINIÈRE, J.-P.; NEUPERT, W. M.; KLIMCHUK, J. A.; GARY, G. A.; PORTIER-FOZZANI, F.; ZUCKER, A. Three-dimensional stereoscopic analysis of solar active region loops.

- I. SOHO/EIT observations at temperatures of $(1.0-1.5) \times 10^6$ K. **The Astrophysical Journal**, v. 515, p. 842–867, apr. 1999. 42
- ASCHWANDEN, M. J.; PONTIEU, B. D.; SCHRIJVER, C. J.; TITLE, A. M. Transverse oscillations in coronal loops observed with TRACE. II. Measurements of geometric and physical parameters. **Solar Physics**, v. 206, p. 99–132, mar. 2002. 42
- ASCHWANDEN, M. J.; WUELSER, J.-P.; NITTA, N. V.; LEMEN, J. R.; SANDMAN, A. First three-dimensional reconstructions of coronal loops with the STEREO A+B spacecraft. III. Instant stereoscopic tomography of active regions. **The Astrophysical Journal**, v. 695, p. 12–29, apr. 2009. 42
- ATHAY, R. G.; WHITE, O. R. Chromospheric and coronal heating by sound waves. **The Astrophysical Journal**, v. 226, p. 1135–1139, dec 1978. 3
- AVRETT, E. H.; LOESER, R. Models of the solar chromosphere and transition region from sumer and hrts observations: Formation of the extreme-ultraviolet spectrum of hydrogen, carbon, and oxygen. **The Astrophysical Journal Supplement Series**, v. 175, n. 1, p. 229, 2008. Available from: <http://stacks.iop.org/0067-0049/175/i=1/a=229>. 2, 44, 108
- BARNES, C. W.; STURROCK, P. A. Force-free magnetic-field structures and their role in solar activity. **The Astrophysical Journal**, v. 174, p. 659, jun. 1972. 40
- BECKERS, J. M. The measurement of solar magnetic fields. In: Howard, R. (Ed.). **Solar Magnetic Fields**. [S.l.: s.n.], 1971. (IAU Symposium, v. 43), p. 3. 38
- BEŞLIU-IONESCU, D.; DONEA, A.-C.; CALLY, P.; LINDSEY, C. Significant acoustic activity in AR10720 on January 15, 2005. **Romanian Astronomical Journal**, v. 16, p. 203, 2006. 14
- BIERMANN, L. Zur deutung der chromosphärischen turbulenz und des exzesses der uv-strahlung der sonne. **Naturwissenschaften**, v. 33, p. 118–119, aug 1946. 1
- BOERNER, P.; EDWARDS, C.; LEMEN, J.; RAUSCH, A.; SCHRIJVER, C.; SHINE, R.; SHING, L.; STERN, R.; TARBELL, T.; TITLE, A.; WOLFSON, C. J.; SOUFLI, R.; SPILLER, E.; GULLIKSON, E.; MCKENZIE, D.; WINDT, D.; GOLUB, L.; PODGORSKI, W.; TESTA, P.; WEBER, M. Initial calibration of the Atmospheric Imaging Assembly (AIA) on the Solar Dynamics Observatory (SDO). **Solar Physics**, v. 275, n. 1, p. 41–66, 2012. ISSN 1573-093X. Available from: <http://dx.doi.org/10.1007/s11207-011-9804-8>. 21

- BOHM-VITENSE, E. Theory of transition-layer emission measures and coronae. **The Astrophysical Journal**, v. 317, p. 750–759, jun 1987. 12
- BROSIUS, J. W.; WILLSON, R. F.; HOLMAN, G. D.; SCHMELZ, J. T. Coronal magnetic structures observing campaign. IV. Multiwaveband observations of sunspot and plage-associated coronal emission. **The Astrophysical Journal**, v. 386, p. 347–358, feb 1992. 104, 108
- BROWN, D.; REGNIER, S.; MARSH, M.; BEWSHER, D. **Working with data from the Solar Dynamics Observatory**. [S.l.], jan. 2011. 28 p. Available from: <https://www.uclan.ac.uk/sdo/assets/sdo_primer_V1.2.pdf>. 22, 23
- BRUNER JR., . E. C. Dynamics of the solar transition zone. **The Astrophysical Journal**, v. 226, p. 1140–1146, dec 1978. 3
- CHEN, P. F.; PRIEST, E. R. Transition-region explosive events: Reconnection modulated by p-mode waves. **Solar Physics**, v. 238, p. 313–327, nov. 2006. 14
- CONDE, C. S. M.; COSTA, J. E. R.; CEDEÑO, M. C. E. Oscillations in the flaring active region NOAA 11272. **Solar Physics**, v. 291, p. 3289–3302, nov. 2016. 44, 53, 54, 55, 60, 80, 101, 103, 104
- DERE, K. P.; LANDI, E.; MASON, H. E.; FOSSI, B. C. M.; YOUNG, P. R. CHIANTI - an atomic database for emission lines. **Astronomy and Astrophysics Supplement Series**, v. 125, oct. 1997. 19
- DURRANT, C. J. Linear force-free magnetic fields and coronal models. **Australian Journal of Physics**, v. 42, p. 317–329, 1989. 40
- ERDÉLYI, R.; BALLAI, I. Heating of the solar and stellar coronae: a review. **Astronomische Nachrichten**, v. 328, p. 726–733, oct 2007. 13
- ERDÉLYI, R.; MENDOZA-BRICEÑO, C. A. Damping of loop oscillations in the stratified corona. In: LACOSTE, H. (Ed.). **SOHO 13 Waves, Oscillations and Small-Scale Transients Events in the Solar Atmosphere: Joint View from SOHO and TRACE**. [S.l.: s.n.], 2004. (ESA Special Publication, v. 547), p. 441. 1
- EYLES, C. J.; HARRISON, R. A.; DAVIS, C. J.; WALTHAM, N. R.; SHAUGHNESSY, B. M.; MAPSON-MENARD, H. C. A.; BEWSHER, D.; CROTHERS, S. R.; DAVIES, J. A.; SIMNETT, G. M.; HOWARD, R. A.; MOSES, J. D.; NEWMARK, J. S.; SOCKER, D. G.; HALAIN, J.-P.; DEFISE,

J.-M.; MAZY, E.; ROCHUS, P. The heliospheric imagers onboard the STEREO mission. **Solar Physics**, v. 254, p. 387–445, feb. 2009. 42

FARGE, M. Wavelet transforms and their applications to turbulence. **Annual Review of Fluid Mechanics**, v. 24, p. 395–457, 1992. 25, 26, 28

FERRARO, V. C. A.; PLUMPTON, C. **An introduction to magneto-fluid mechanics**. Clarendon P., 1966. Available from:
<<http://books.google.com.br/books?id=3fJQAAAAMAAJ>>. 4, 10

FREELAND, S.; BENTLEY, R. SolarSoft. In: _____. **Encyclopedia of Astronomy and Astrophysics**. [S.l.: s.n.], 2000. 22

GARY, G. A. Plasma beta above a solar active region: Rethinking the paradigm. **Solar Physics**, v. 203, p. 71–86, oct. 2001. 37

HOWARD, R. A.; MOSES, J. D.; VOURLIDAS, A.; NEWMARK, J. S.;
SOCKER, D. G.; PLUNKETT, S. P.; KORENDYKE, C. M.; COOK, J. W.;
HURLEY, A.; DAVILA, J. M.; THOMPSON, W. T.; CYR, O. C. S.;
MENTZELL, E.; MEHALICK, K.; LEMEN, J. R.; WUELSER, J. P.; DUNCAN,
D. W.; TARBELL, T. D.; WOLFSON, C. J.; MOORE, A.; HARRISON, R. A.;
WALTHAM, N. R.; LANG, J.; DAVIS, C. J.; EYLES, C. J.; MAPSON-MENARD,
H.; SIMNETT, G. M.; HALAIN, J. P.; DEFISE, J. M.; MAZY, E.; ROCHUS, P.;
MERCIER, R.; RAVET, M. F.; DELMOTTE, F.; AUCHERE, F.;
DELABOUDINIÈRE, J. P.; BOTHMER, V.; DEUTSCH, W.; WANG, D.; RICH,
N.; COOPER, S.; STEPHENS, V.; MAAHS, G.; BAUGH, R.; MCMULLIN, D.;
CARTER, T. Sun Earth Connection Coronal and Heliospheric Investigation
(SECCHI). **Space Science Reviews**, v. 136, p. 67–115, apr. 2008. 2, 42

IRELAND, J.; WALSH, R. W.; HARRISON, R. A.; PRIEST, E. R. A wavelet
analysis of active region oscillations. **Astronomy and Astrophysics**, v. 347, p.
355–365, jul 1999. 29

JAGER, C. de; KUPERUS, M. The acoustic energy flux of the sun and the
formation of the corona. **Bulletin of the Astronomical Institutes of the
Netherlands**, v. 16, p. 71, nov 1961. 13

KHODACHENKO, M. L.; ARBER, T. D.; RUCKER, H. O.; HANSLMEIER, A.
Collisional and viscous damping of mhd waves in partially ionized plasmas of the
solar atmosphere. **Astronomy and Astrophysics**, v. 422, p. 1073–1084, aug
2004. 3

- KIM, S.; NAKARIAKOV, V. M.; SHIBASAKI, K. Slow magnetoacoustic oscillations in the microwave emission of solar flares. **The Astrophysical Journal Letters**, v. 756, p. –36, sep 2012. [1](#)
- KLIEM, B.; DAMMASCH, I. E.; CURDT, W.; WILHELM, K. Correlated dynamics of hot and cool plasmas in the main phase of a solar flare. **The Astrophysical Journal Letters**, v. 568, p. –61, mar 2002. [3](#)
- KOOP, R. A. **Equilibrium structure of a shock-heated corona**. Scientific Report No. 4. AFCRL-68-0312. PhD Thesis (PhD) — Harvard University, 1968. [11](#)
- KOSOVICHEV, A. G.; ZHARKOVA, V. V. X-ray flare sparks quake inside Sun. **Nature**, v. 393, p. 317–318, may 1998. [14](#)
- KUMAR, P.; NAKARIAKOV, V. M.; CHO, K.-S. Observation of a quasi-periodic pulsation in hard x-ray, radio, and extreme-ultraviolet wavelengths. **The Astrophysical Journal**, v. 822, p. 7, may 2016. [1](#), [14](#)
- KUPERUS, M. The heating of the solar corona. **Space Science Reviews**, v. 9, p. 713–739, aug 1969. [11](#)
- KUPERUS, M.; IONSON, J. A.; SPICER, D. S. On the theory of coronal heating mechanisms. **Annual Review of Astronomy and Astrophysics**, v. 19, p. 7–40, 1981. [11](#), [13](#)
- LANDAU, L.; LIFSHITZ, E. **Fluid Mechanics**. Second. Oxford OX3 0BW, England: 00/1959, 1987. (A Course of Theoretical Physics., v. 6). [4](#), [7](#)
- LEMEN, J. R.; TITLE, A. M.; AKIN, D. J.; BOERNER, P. F.; CHOU, C.; DRAKE, J. F.; DUNCAN, D. W.; EDWARDS, C. G.; FRIEDLAENDER, F. M.; HEYMAN, G. F.; HURLBURT, N. E.; KATZ, N. L.; KUSHNER, G. D.; LEVAY, M.; LINDGREN, R. W.; MATHUR, D. P.; MCFEATERS, E. L.; MITCHELL, S.; REHSE, R. A.; SCHRIJVER, C. J.; SPRINGER, L. A.; STERN, R. A.; TARBELL, T. D.; WUELSER, J.-P.; WOLFSON, C. J.; YANARI, C.; BOOKBINDER, J. A.; CHEIMETS, P. N.; CALDWELL, D.; DELUCA, E. E.; GATES, R.; GOLUB, L.; PARK, S.; PODGORSKI, W. A.; BUSH, R. I.; SCHERRER, P. H.; GUMMIN, M. A.; SMITH, P.; AUKER, G.; JERRAM, P.; POOL, P.; SOUFLI, R.; WINDT, D. L.; BEARDSLEY, S.; CLAPP, M.; LANG, J.; WALTHAM, N. The Atmospheric Imaging Assembly (AIA) on the Solar Dynamics Observatory (SDO). **Solar Physics**, v. 275, p. 17–40, jan. 2012. [1](#), [17](#), [18](#), [19](#), [20](#), [21](#)

- LEROY, B.; SCHWARTZ, S. J. Propagation of waves in an atmosphere in the presence of a magnetic field. V. The theory of magneto-acoustic-gravity oscillations. **Astronomy and Astrophysics**, v. 112, p. 84–103, aug 1982. 1
- LI, D.; NING, Z. J.; ZHANG, Q. M. Imaging and spectral observations of quasi-periodic pulsations in a solar flare. **The Astrophysical Journal**, v. 807, p. 72, jul. 2015. 14, 15
- LOW, B. C.; NAKAGAWA, Y. Dynamics of solar magnetic fields. VI. Force-free magnetic fields and motions of magnetic foot-points. **The Astrophysical Journal**, v. 199, p. 237–246, jul. 1975. 40
- MACHADO, M. E.; AVRETT, E. H.; VERNAZZA, J. E.; NOYES, R. W. Semiempirical models of chromospheric flare regions. **The Astrophysical Journal**, v. 242, p. 336–351, nov. 1980. 2, 43, 44, 108
- MACHOL, J. **GOES X-ray Sensor (XRS) Measurements**. [S.l.], 2016. 14 p. Available from: https://ngdc.noaa.gov/stp/satellite/goes/doc/GOES_XRS_readme.pdf. 14
- MACKAY, D. H.; YEATES, A. R. The Sun’s global photospheric and coronal magnetic fields: Observations and models. **Living Reviews in Solar Physics**, v. 9, p. 6, dec. 2012. 39
- MARSH, M. S.; WALSH, R. W.; MOORTEL, I. D.; IRELAND, J. Joint observations of propagating oscillations with SOHO/CDS and TRACE. **Astronomy and Astrophysics**, v. 404, p. –37, jun 2003. 3
- MARTÍNEZ-OLIVEROS, J. C.; MORADI, H.; DONEA, A.-C. Seismic emissions from a highly impulsive M6.7 solar flare. **Solar Physics**, v. 251, p. 613–626, sep. 2008. 14
- MATHIOUDAKIS, M.; JESS, D. B.; ERDÉLYI, R. Alfvén waves in the solar atmosphere. **Space Science Reviews**, p. 94, nov 2012. 1
- MCLAUGHLIN, J. A.; HOOD, A. W. MHD wave propagation in the neighbourhood of a two-dimensional null point. **Astronomy and Astrophysics**, v. 420, p. 1129–1140, jun. 2004. 14
- MCWHIRTER, R. W. P.; THONEMANN, P. C.; WILSON, R. The heating of the solar corona. II. A model based on energy balance. **Astronomy and Astrophysics**, v. 40, p. 63–73, apr 1975. 3, 11, 12, 13

MENDOZA-BRICEÑO, C. A.; ERDÉLYI, R.; SIGALOTTI, L. D. G. The effects of stratification on oscillating coronal loops. **The Astrophysical Journal**, v. 605, n. 1, p. 493, 2004. Available from:

<<http://stacks.iop.org/0004-637X/605/i=1/a=493>>. 1

MIHALAS, D.; MIHALAS, B. W. **Foundations of radiation hydrodynamics**. New York, Oxford: 00/1984, 1984. 4, 7

MOORTEL, I. D. Propagating magnetohydrodynamics waves in coronal loops. **Philosophical Transactions of the Royal Society of London Series A**, v. 364, p. 461–472, feb. 2006. 1

_____. Longitudinal waves in coronal loops. **Space Science Reviews**, v. 149, p. 65–81, dec 2009. 1

MOORTEL, I. D.; HOOD, A. W.; IRELAND, J. Coronal seismology through wavelet analysis. **Astronomy and Astrophysics**, v. 381, p. 311–323, jan. 2002. 29

MOORTEL, I. D.; IRELAND, J.; WALSH, R. W. Observation of oscillations in coronal loops. **Astronomy and Astrophysics**, v. 355, p. L23–L26, mar. 2000. 1, 29

_____. Observation of oscillations in coronal loops. **Astronomy and Astrophysics**, v. 355, p. –23, mar 2000. 3

MOORTEL, I. D.; IRELAND, J.; WALSH, R. W.; HOOD, A. W. Longitudinal intensity oscillations in coronal loops observed with TRACE. I. Overview of measured parameters. **Solar Physics**, v. 209, p. 61–88, sep 2002. 42

MOORTEL, I. D.; MCATEER, R. T. J. Waves and wavelets: An automated detection technique for solar oscillations. **Solar Physics**, v. 223, p. 1–11, sep 2004. 29, 31

MOORTEL, I. D.; MUNDAY, S. A.; HOOD, A. W. Wavelet analysis: The effect of varying basic wavelet parameters. **Solar Physics**, v. 222, p. 203–228, 2004. 1, 25, 26, 29

MORTON, R. J.; HOOD, A. W.; ERDÉLYI, R. Propagating magneto-hydrodynamic waves in a cooling homogenous coronal plasma. **Astronomy and Astrophysics**, v. 512, p. –23, mar 2010. 1

NAKAGAWA, Y.; RAADU, M. A. On practical representation of magnetic field. **Solar Physics**, v. 25, n. 1, p. 127–135, 1972. ISSN 1573-093X. Available from: <<http://dx.doi.org/10.1007/BF00155751>>. 2, 40

NAKAGAWA, Y.; RAADU, M. A.; BILLINGS, D. E.; MCNAMARA, D. On the topology of filaments and chromospheric fibrils near sunspots. **Solar Physics**, v. 19, p. 72–85, aug. 1971. 40

NAKARIAKOV, V. M.; FOULLON, C.; MYAGKOVA, I. N.; INGLIS, A. R. Quasi-periodic pulsations in the gamma-ray emission of a solar flare. **The Astrophysical Journal Letters**, v. 708, p. L47–L51, jan. 2010. 1, 14

NAKARIAKOV, V. M.; INGLIS, A. R.; ZIMOVETS, I. V.; FOULLON, C.; VERWICHTE, E.; SYCH, R.; MYAGKOVA, I. N. Oscillatory processes in solar flares. **Plasma Physics and Controlled Fusion**, v. 52, n. 12, p. 124009, dec. 2010. 14

NAKARIAKOV, V. M.; MELNIKOV, V. F. Quasi-periodic pulsations in solar flares. **Space Science Reviews**, v. 149, p. 119–151, dec 2009. 1, 14, 108

NAKARIAKOV, V. M.; VERWICHTE, E. Coronal waves and oscillations. **Living Reviews in Solar Physics**, v. 2, n. 3, 2005. Available from: <<http://www.livingreviews.org/lrsp-2005-3>>. 3, 13

NARAIN, U.; ULMSCHNEIDER, P. Chromospheric and coronal heating mechanisms II. **Space Science Reviews**, v. 75, p. 453–509, feb 1996. 3

NISTICÒ, G.; NAKARIAKOV, V. M.; VERWICHTE, E. Decaying and decayless transverse oscillations of a coronal loop. **Astronomy and Astrophysics**, v. 552, p. 6, apr 2013. 1

NISTICÒ, G.; VERWICHTE, E.; NAKARIAKOV, V. 3D Reconstruction of Coronal Loops by the Principal Component Analysis. **Entropy**, v. 15, p. 4520–4539, oct. 2013. 42

O'DWYER, B.; ZANNA, G. D.; MASON, H. E.; WEBER, M. A.; TRIPATHI, D. SDO/AIA response to coronal hole, quiet Sun, active region, and flare plasma. **Astronomy and Astrophysics**, v. 521, p. A21, 2010. Available from: <<http://dx.doi.org/10.1051/0004-6361/201014872>>. xvii, 43, 44

PESNELL, W. D.; THOMPSON, B. J.; CHAMBERLIN, P. C. The Solar Dynamics Observatory (SDO). **Solar Physics**, v. 275, n. 1, p. 3–15, 2012. ISSN

1573-093X. Available from:

<<http://dx.doi.org/10.1007/s11207-011-9841-3>>. 17

PONTIEU, B. D.; TITLE, A. M.; LEMEN, J. R.; KUSHNER, G. D.; AKIN, D. J.; ALLARD, B.; BERGER, T.; BOERNER, P.; CHEUNG, M.; CHOU, C.; DRAKE, J. F.; DUNCAN, D. W.; FREELAND, S.; HEYMAN, G. F.; HOFFMAN, C.; HURLBURT, N. E.; LINDGREN, R. W.; MATHUR, D.; REHSE, R.; SABOLISH, D.; SEGUIN, R.; SCHRIJVER, C. J.; TARBELL, T. D.; WÜLSER, J.-P.; WOLFSON, C. J.; YANARI, C.; MUDGE, J.; NGUYEN-PHUC, N.; TIMMONS, R.; BEZOOIJEN, R. van; WEINGROD, I.; BROOKNER, R.; BUTCHER, G.; DOUGHERTY, B.; EDER, J.; KNAGENHJELM, V.; LARSEN, S.; MANSIR, D.; PHAN, L.; BOYLE, P.; CHEIMETS, P. N.; DELUCA, E. E.; GOLUB, L.; GATES, R.; HERTZ, E.; MCKILLOP, S.; PARK, S.; PERRY, T.; PODGORSKI, W. A.; REEVES, K.; SAAR, S.; TESTA, P.; TIAN, H.; WEBER, M.; DUNN, C.; ECCLES, S.; JAEGGLI, S. A.; KANKELBORG, C. C.; MASHBURN, K.; PUST, N.; SPRINGER, L.; CARVALHO, R.; KLEINT, L.; MARMIE, J.; MAZMANIAN, E.; PEREIRA, T. M. D.; SAWYER, S.; STRONG, J.; WORDEN, S. P.; CARLSSON, M.; HANSTEEN, V. H.; LEENAARTS, J.; WIESMANN, M.; ALOISE, J.; CHU, K.-C.; BUSH, R. I.; SCHERRER, P. H.; BREKKE, P.; MARTINEZ-SYKORA, J.; LITES, B. W.; MCINTOSH, S. W.; UITENBROEK, H.; OKAMOTO, T. J.; GUMMIN, M. A.; AUKER, G.; JERRAM, P.; POOL, P.; WALTHAM, N. The Interface Region Imaging Spectrograph (IRIS). **Solar Physics**, v. 289, p. 2733–2779, jul. 2014. 14

POTTASCH, S. R. On the radiative cooling rate in stellar atmospheres. **Bulletin of the Astronomical Institutes of the Netherlands**, v. 18, p. 7, 1965. 11, 12

PRIEST, E. R. **Solar magneto-hydrodynamics**. Hingham: D. Reidel Pub. Co., 1982. 74P p. 3, 4, 6, 9, 10, 11

ROBBRECHT, E.; VERWICHTE, E.; BERGHMANS, D.; HOCHEDÉZ, J. F.; POEDTS, S.; NAKARIAKOV, V. M. Slow magnetoacoustic waves in coronal loops: EIT and TRACE. **Astronomy and Astrophysics**, v. 370, p. 591–601, may 2001. 3

ROBERTS, B. Wave propagation in a magnetically structured atmosphere. I. Surface waves at a magnetic interface. **Solar Physics**, v. 69, p. 27–38, jan 1981. 1

_____. Wave propagation in a magnetically structured atmosphere. II. Waves in a magnetic slab. **Solar Physics**, v. 69, p. 39–56, jan 1981. 1, 11

- ROSA, M. D.; SLATER, G. **Guide to SDO Data Analysis**. [S.l.], feb. 2015. 90 p. Available from:
 <<https://www.lmsal.com/sdodocs/doc/dcur/SDOD0060.zip/zip/entry/>>. 20, 22
- ROSA, M. L. D.; SCHRIJVER, C. J.; BARNES, G.; LEKA, K. D.; LITES, B. W.; ASCHWANDEN, M. J.; AMARI, T.; CANOU, A.; MCTIERNAN, J. M.; RÉGNIER, S.; THALMANN, J. K.; VALORI, G.; WHEATLAND, M. S.; WIEGELMANN, T.; CHEUNG, M. C. M.; CONLON, P. A.; FUHRMANN, M.; INHESTER, B.; TADESSE, T. A critical assessment of nonlinear force-free field modeling of the solar corona for active region 10953. **The Astrophysical Journal**, v. 696, p. 1780–1791, may 2009. 42
- ROSNER, R.; TUCKER, W. H.; VAIANA, G. S. Dynamics of the quiescent solar corona. **The Astrophysical Journal**, v. 220, p. 643–645, mar 1978. 11, 12
- SCHERRER, P. H.; SCHOU, J.; BUSH, R. I.; KOSOVICHEV, A. G.; BOGART, R. S.; HOEKSEMA, J. T.; LIU, Y.; DUVALL, T. L.; ZHAO, J.; TITLE, A. M.; SCHRIJVER, C. J.; TARBELL, T. D.; TOMCZYK, S. The Helioseismic and Magnetic Imager (HMI) investigation for the Solar Dynamics Observatory (SDO). **Solar Physics**, v. 275, n. 1, p. 207–227, 2011. ISSN 1573-093X. Available from:
 <<http://dx.doi.org/10.1007/s11207-011-9834-2>>. 2, 17, 20
- SCHMELZ, J. T.; HOLMAN, G. D.; BROSIUS, J. W.; GONZALEZ, R. D. Coronal magnetic structures observing campaign. II - Magnetic and plasma properties of a solar active region. **The Astrophysical Journal**, v. 399, p. 733–742, nov 1992. 104, 108
- SCHMELZ, J. T.; HOLMAN, G. D.; BROSIUS, J. W.; WILLSON, R. F. Coronal magnetic structures observing campaign. III. Coronal plasma and magnetic field diagnostics derived from multiwaveband active region observations. **The Astrophysical Journal**, v. 434, p. 786–794, oct 1994. 104, 108
- SCHRIJVER, C. J. Simulations of the photospheric magnetic activity and outer atmospheric radiative losses of cool stars based on characteristics of the solar magnetic field. **The Astrophysical Journal**, v. 547, p. 475–490, jan. 2001. 2
- SCHRIJVER, C. J.; DE-ROSA, M. L. Photospheric and heliospheric magnetic fields. **Solar Physics**, v. 212, p. 165–200, jan. 2003. 2
- SCHWARZSCHILD, M. On noise arising from the solar granulation. **The Astrophysical Journal**, v. 107, p. 1, jan 1948. 1

- SEEHAFER, N. Determination of constant alpha force-free solar magnetic fields from magnetograph data. **Solar Physics**, v. 58, p. 215–223, jul. 1978. 39, 40
- SELHORST, C. L.; SILVA-VÁLIO, A.; COSTA, J. E. R. Solar atmospheric model over a highly polarized 17 GHz active region. **Astronomy and Astrophysics**, v. 488, p. 1079–1084, sep. 2008. 2
- SHEELEY JR., N. R.; HARVEY, J. W. The calculation of force-free fields from discrete flux distributions. **Solar Physics**, v. 45, p. 275–290, dec. 1975. 40
- SHEN, Y.; LIU, Y. Observational study of the quasi-periodic fast-propagating magnetosonic waves and the associated flare on 2011 May 30. **The Astrophysical Journal**, v. 753, p. 53, jul. 2012. 14
- STEIN, R. F. Waves in the solar atmosphere. I. The acoustic energy flux. **The Astrophysical Journal**, v. 154, p. 297, oct 1968. 1
- STEIN, R. F.; LEIBACHER, J. Waves in the solar atmosphere. **Annual Review of Astronomy and Astrophysics**, v. 12, p. 407–435, 1974. 1, 3
- STEIN, R. F.; SCHWARTZ, R. A. Waves in the solar atmosphere. II. Large-amplitude acoustic pulse propagation. **The Astrophysical Journal**, v. 177, p. 807, nov 1972. 1
- SU, J. T.; SHEN, Y. D.; LIU, Y.; LIU, Y.; MAO, X. J. Imaging observations of quasi-periodic pulsations in solar flare loops with SDO/AIA. **The Astrophysical Journal**, v. 755, p. 113, aug. 2012. 14
- SU, Y.; VERONIG, A. M.; HOLMAN, G. D.; DENNIS, B. R.; WANG, T.; TEMMER, M.; GAN, W. Imaging coronal magnetic-field reconnection in a solar flare. **Nature Physics**, v. 9, p. 489–493, aug 2013. 109
- SYCH, R.; NAKARIAKOV, V. M. Wave dynamics in a sunspot umbra. **Astronomy and Astrophysics**, v. 569, p. –72, sep 2014. 29
- SYCH, R.; NAKARIAKOV, V. M.; KARLICKY, M.; ANFINOGENTOV, S. Relationship between wave processes in sunspots and quasi-periodic pulsations in active region flares. **Astronomy and Astrophysics**, v. 505, p. 791–799, oct. 2009. 14
- SYCH, R.; ZAQRASHVILI, T. V.; NAKARIAKOV, V. M.; ANFINOGENTOV, S. A.; SHIBASAKI, K.; YAN, Y. Frequency drifts of 3-min oscillations in

microwave and EUV emission above sunspots. **Astronomy and Astrophysics**, v. 539, p. A23, mar. 2012. 29

SYCH, R. A.; NAKARIAKOV, V. M. The pixelised wavelet filtering method to study waves and oscillations in time sequences of solar atmospheric images. **Solar Physics**, v. 248, 2008. 1, 25, 29, 30, 31, 32, 34, 107

SYCH, R. A.; NAKARIAKOV, V. M.; ANFINOGENOV, S. A.; OFMAN, L. Web-based data processing system for automated detection of oscillations with applications to the solar atmosphere. **Solar Physics**, v. 266, n. 2, p. 349–367, 2010. ISSN 1573-093X. Available from: <<http://dx.doi.org/10.1007/s11207-010-9616-2>>. 1, 29, 34, 35

TORRENCE, C.; COMPO, G. P. A practical guide to wavelet analysis. **Bulletin of the American Meteorological Society**, v. 79, p. 61–78, jan 1998. 1, 25, 26, 27, 28, 29, 31, 35

ULMSCHNEIDER, P. On frequency and strength of shock waves in the solar atmosphere. **Solar Physics**, v. 12, p. 403–415, jun 1970. 3

VERWICHTE, E.; DOORSSELAERE, T. V.; FOULLON, C.; WHITE, R. S. Coronal Alfvén speed determination: Consistency between seismology using AIA/SDO transverse loop oscillations and magnetic extrapolation. **The Astrophysical Journal**, v. 767, p. 16, apr. 2013. 2

WALSH, R. W.; IRELAND, J. The heating of the solar corona. **The Astronomy and Astrophysics Review**, v. 12, p. 1–41, 2003. 3

WANG, T. Oscillations and waves in coronal loops. **ArXiv Astrophysics e-prints**, dec 2006. 10

WANG, T.; SOLANKI, S. K.; CURDT, W.; INNES, D. E.; DAMMASCH, I. E. Doppler shift oscillations of hot solar coronal plasma seen by sumer: A signature of loop oscillations? **The Astrophysical Journal Letters**, v. 574, n. 1, p. L101, 2002. Available from: <<http://stacks.iop.org/1538-4357/574/i=1/a=L101>>. 80, 107

WANG, T. J.; SOLANKI, S. K.; CURDT, W.; INNES, D. E.; DAMMASCH, I. E.; KLIEM, B. Hot coronal loop oscillations observed with sumer: Examples and statistics. **Astronomy and Astrophysics**, v. 406, p. 1105–1121, aug 2003. 1, 3, 4, 42

- WANG, T. J.; SOLANKI, S. K.; INNES, D. E.; CURDT, W.; MARSCH, E. Slow-mode standing waves observed by sumer in hot coronal loops. **Astronomy and Astrophysics**, v. 402, p. –17, may 2003. 80, 106, 107
- WENG, H.; LAU, K. M. Wavelets, period doubling, and time-frequency localization with application to organization of convection over the tropical western pacific. **Journal of Atmospheric Sciences**, v. 51, p. 2523–2541, sep 1994. 25, 26
- WHITE, R. S.; VERWICHTE, E. Transverse coronal loop oscillations seen in unprecedented detail by AIA/SDO. **Astronomy and Astrophysics**, v. 537, p. A49, jan. 2012. 2, 42
- WIEGELMANN, T.; SAKURAI, T. Solar force-free magnetic fields. **Living Reviews in Solar Physics**, v. 9, p. 5, dec. 2012. 37, 38
- WILLIAMS, D. R.; MATHIOUDAKIS, M.; GALLAGHER, P. T.; PHILLIPS, K. J. H.; MCATEER, R. T. J.; KEENAN, F. P.; RUDAWY, P.; KATSIYANNIS, A. C. An observational study of a magneto-acoustic wave in the solar corona. **Monthly Notices of the Royal Astronomical Society**, v. 336, p. 747–752, nov. 2002. 106
- WOODS, T. N.; EPARVIER, F. G.; HOCK, R.; JONES, A. R.; WOODRASKA, D.; JUDGE, D.; DIDKOVSKY, L.; LEAN, J.; MARISKA, J.; WARREN, H.; MCMULLIN, D.; CHAMBERLIN, P.; BERTHIAUME, G.; BAILEY, S.; FULLER-ROWELL, T.; SOJKA, J.; TOBISKA, W. K.; VIREECK, R. Extreme Ultraviolet Variability Experiment (EVE) on the Solar Dynamics Observatory (SDO): Overview of science objectives, instrument design, data products, and model developments. **Solar Physics**, v. 275, p. 115–143, jan. 2012. 17
- YUAN, D.; SYCH, R.; REZNIKOVA, V. E.; NAKARIAKOV, V. M. Multi-height observations of magnetoacoustic cut-off frequency in a sunspot atmosphere. **Astronomy and Astrophysics**, v. 561, p. –19, jan 2014. 29
- ZHANG, Y.; ZHANG, J.; WANG, J.; NAKARIAKOV, V. M. Coexisting fast and slow propagating waves of the extreme-UV intensity in solar coronal plasma structures. **Astronomy and Astrophysics**, v. 581, p. A78, sep. 2015. 3

GLOSSARY

Filtergram – A photograph of the Sun at a particular frequency range (by means of a variable filter).

Footpoint – The intersection of magnetic loops with the photosphere.

Ka-band – Part of the electromagnetic spectrum used in the transmission of science data from space missions. Ka-band, at 26 GHz can transmit a high rate data hundred of time faster, comparing with other bands.

PUBLICAÇÕES TÉCNICO-CIENTÍFICAS EDITADAS PELO INPE

Teses e Dissertações (TDI)

Teses e Dissertações apresentadas nos Cursos de Pós-Graduação do INPE.

Manuais Técnicos (MAN)

São publicações de caráter técnico que incluem normas, procedimentos, instruções e orientações.

Notas Técnico-Científicas (NTC)

Incluem resultados preliminares de pesquisa, descrição de equipamentos, descrição e ou documentação de programas de computador, descrição de sistemas e experimentos, apresentação de testes, dados, atlas, e documentação de projetos de engenharia.

Relatórios de Pesquisa (RPQ)

Reportam resultados ou progressos de pesquisas tanto de natureza técnica quanto científica, cujo nível seja compatível com o de uma publicação em periódico nacional ou internacional.

Propostas e Relatórios de Projetos (PRP)

São propostas de projetos técnico-científicos e relatórios de acompanhamento de projetos, atividades e convênios.

Publicações Didáticas (PUD)

Incluem apostilas, notas de aula e manuais didáticos.

Publicações Seriadas

São os seriados técnico-científicos: boletins, periódicos, anuários e anais de eventos (simpósios e congressos). Constam destas publicações o Internacional Standard Serial Number (ISSN), que é um código único e definitivo para identificação de títulos de seriados.

Programas de Computador (PDC)

São a seqüência de instruções ou códigos, expressos em uma linguagem de programação compilada ou interpretada, a ser executada por um computador para alcançar um determinado objetivo. Aceitam-se tanto programas fonte quanto os executáveis.

Pré-publicações (PRE)

Todos os artigos publicados em periódicos, anais e como capítulos de livros.